OPTICAL COATINGS FOR IMPROVED SEMICONDUCTOR DIODE LASER PERFORMANCE

By

MARCEL GERARD BOUDREAU, B.ENG., M.ENG.

A Thesis
Submitted to the School of Graduate Studies
in Partial Fulfillment of the Requirements
for the Degree
Doctor of Philosophy.

McMaster University

© Copyright by Marcel Gerard Boudreau, July 1997

OPTICAL COATINGS FOR IMPROVED SEMICONDUCTOR DIODE LASER PERFORMANCE

DOCTOR OF PHILOSOPHY (1997)
(Engineering Physics)

McMaster University
Hamilton, Ontario

TITLE: Optical Coatings for Improved Semiconductor Diode Laser Performance.

AUTHOR: Marcel G. Boudreau, B.Eng., M.Eng. (McMaster University)

SUPERVISOR: Dr. P. Mascher

NUMBER OF PAGES: xiii, 132

Abstract

Optical coatings have been applied to the facets of semiconductor diode lasers using the electron cyclotron resonance plasma enhanced chemical vapour deposition technique. Processes have been developed for the fabrication of optical interference filters from silicon oxynitride thin films using both tris dimethylaminosilane and silane as the silicon precursor. An important component for the fabrication of filters with a controlled reflectance spectrum is the in situ monitoring of the deposited film thickness and refractive index by ellipsometry. Using the ellipsometer, it is shown that, after correcting for systematic errors, an accurate measurement of the film index of refraction can be made during a deposition. Three separate applications of these optical coatings are discussed. The fabrication of anti-reflection coatings, the fabrication of narrow band reflectance coatings which could potentially have beneficial effects on the spectral properties of the laser, and the use of silicon nitride layers, in conjunction with a sulphur based passivation, to improve the reliability of high power AlGaAs based lasers. Single and double layer anti-reflection coatings have been designed for specific laser waveguide structures. An existing theoretical model of the spectral output of a semiconductor laser has been modified to include the effect of an optical filter with a highly wavelength dependent reflectance, in order to understand the limitations of this technique. Finally, improvements in the surface properties of passivated and encapsulated AlGaAs material have been observed through an increase in the yield of photoluminescence after the passivation process was applied.

Acknowledgements

I would like to thank my supervisor, Dr. Peter Mascher, for his guidance and support, as well as the trust that he has placed in me. I also thank Dr. Daniel Cassidy for lending me precious space on a sub-basement optical table, as well as for many helpful conversations. Several disasters have been averted by the convenient location of our reactor next to the MBE machine, and I am indebted to both Brad Robinson and Scott McMaster for their generosity. In addition, I would like to thank all of the collegues who have worked with me and who have made my years at McMaster very enjoyable. Finally, I would like to thank my wife Susan and my parents André and Sylvia for their constant love and support.

Contents

1 Introduction **1**

2 The Design of Optical Interference Filters **5**

2.1 Thin Film Optics 5

2.2 Typical Designs 10

2.2.1 Anti-Reflection Coatings 12

2.2.2 High Reflection Coatings 21

2.3 Effect of the Optical Coating on Laser Properties 25

3 Fabrication of Multilayered Structures **31**

3.1 Introduction 31

3.2 Plasma Characteristics 31

3.3 Material Properties 34

3.3.1 Experimental Details 34

3.3.2 Properties of Silicon Oxynitride Formed using TDAS 37

3.4 Ellipsometric Monitoring 44

3.4.1 The Measurement Process 45

3.4.2 Compensator Imperfections 47

3.4.3 Window Imperfections 48

3.4.4 Substrate Index Errors 50

3.5 Coating of Laser Facets 50

3.6 Control Algorithms 52

3.7 Summary 55

4 Characterization of Interference Filter Properties 57

4.1 Experimental Details 57

4.2 AR and Wide Band HR Coatings 60

4.3 Narrow Band Filters 65

4.4 Summary 69

5 Facet Coatings for High Power Lasers 71

5.1 Surface Properties of GaAs and AlGaAs 73

5.2 Passivation of GaAs and AlGaAs 77

5.3 PL as a Surface Characterization Technique 79

5.4 Facet Degradation in SDL's 83

5.5 Experimental Details 88

5.6 Low Temperature PL Measurements 93

5.7 PL Decay Measurements 98

5.8 Performance of Treated Lasers 106

6 Conclusions and Future Work 111

6.1 Conclusions 111

6.2 Future Work 115

A Fabry-Perot Model of a Semiconductor Laser 119

B Publications and Presentations 123

List of Figures

1.1 Effect of a narrow band filter with Reflectance R(ω) on the output spectrum of a SDL. G(ω) is the gain spectrum. 2

2.1 Schematic of a thin film optical filter 8

2.2 Multilayer AR coating consisting of two subsystems a and b separated by a central layer i. 13

2.3 Reflectance spectrum of both a single layer and two layer AR coating. 15

2.4 Reflection of light from a waveguide by a thin film optical filter. 16

2.5 A comparison of the rigorous and approximate methods for calculating the optimum index of refraction for an AR coating. 18

2.6 The effect of illumination on the reflectance of light from an AR coated laser facet. 19

2.7 The result of optimizing a two layer AR coating for a waveguide structure. 20

2.8 Reflectance spectra for quarter wave stack HR filters showing the effect of variations in the index contrast ($n_{high} - n_{low}$) and the number of periods. In all cases $n_{low} = 1.46$. 22

2.9 The effect of illumination on the reflectance of light from a laser facet coated with a narrow band interference filter. 23

2.10 The effect of illumination on the reflectance of light from a laser facet coated with a wide band interference filter. 23

2.11 Schematic diagram of the optical path traced in a Fabry-Perot semiconductor laser cavity. 27

2.12 Calculated SMSR versus the difference in modal reflectance. 28

2.13 Calculated SMSR versus the optical coating thickness. 29

3.1 A schematic diagram of the ECR-PECVD system. 33

3.2 Measured temperature versus time for different plasma gases. 34

3.3 The geometry used for the ERD measurements. 36

3.4 A schematic diagram of the TDAS molecule. 37

3.5 The effect of varying the nitrogen partial pressure on the measured FTIR spectra of SiN_x thin films. 38

3.6 The effect of varying the nitrogen partial pressure on the measured composition of SiN_x thin films. 39

3.7 The effect of varying the nitrogen partial pressure on the measured etch rate and position of the Si-N stretching peak of SiN_x thin films. . 41

3.8 The effect of varying the fraction of oxygen in an argon and nitrogen plasma on the film index of refraction. 42

3.9 The effect of varying the flow ratio of oxygen to SiH_4 in an argon plasma on the film index of refraction. 43

3.10 Schematic diagram of the rotating compensator ellipsometer. 45

3.11 The effect of incorporating the compensator imperfections on the measured index of refraction of a deposited film. 48

3.12 Measured substrate refractive index versus substrate temperature for a silicon substrate at 633 nm. 51

3.13 The effect of incorporating substrate temperature changes on the measured film refractive index versus thickness for a typical deposition. . . 52

3.14 A schematic diagram of the fixture used to mount laser bars for optical coating. 53

3.15 Calibration of the flow rate required for a given index of refraction and deposition rate. 54

3.16 SEM of an optical filter consisting of 35 layers. 55

3.17 Deposition rate vs time for the filter shown above. 56

4.1 The mount used to measure the reflectance spectrum. 58

4.2 The measured reflectance for a single layer AR coating. 61

4.3 The measured reflectance for a two layer AR coating designed for 1500 nm on silicon. 62

4.4 The measured and model Δ and Ψ trajectory for the 2 layer AR coating of Figure 4.3. 63

4.5 Measured and model reflectance for a 7 layer HR filter using SiH_4. . . 64

4.6 Measured and model reflectance for a 17 layer quarter wave stack using TDAS. 65

4.7 The measured L-I characteristic for both facets of a HR coated laser. . 66

4.8 The measured model reflectivity and threshold current versus chip position on the coated laser bar. 67

4.9 Back-scattered electron image of a 10 period rugate filter. 67

4.10 The measured reflectances of narrow band filters designed for 860 nm and 965 nm. 68

5.1 A schematic illustration of the conduction and valence band edges near the surface of a semiconductor with acceptor-like surface states. 75

5.2 The conduction and valence band edges near the surface of a semiconductor with surface states under high level injection conditions. 82

5.3 A schematic diagram of the integrated PL measurement system. . . . 90

5.4 Low temperature PL spectra of undoped $Al_{0.11}Ga_{0.89}As$ (a)untreated, (b)sulphur treated and (c)sulphur treated and encapsulated with 100 nm SiN_x. 94

5.5 Measured PL enhancement as a function of aluminum mole fraction for sulphur treated and sulphur treated and encapsulated $Al_xGa_{1-x}As$. 96

5.6 SEM image of a sulphur treated laser facet prior to optimization of the pre-etch solution. 97

5.7 The effect of the optical coating on the PL stability for (100) GaAs surfaces. 99

5.8 The effect of the sulphur treatment on the PL stability for coated (100) GaAs surfaces. 100

5.9 The measured PL decay for illumination at 632 nm with 39 kW/cm^2, and 3.6 kW/cm^2 intensity. 102

5.10 Measured PL intensity versus time after various plasma exposures. . . 103

5.11 Measured PL intensity versus time for a (110) laser facet after a 30 second argon plasma exposure and SiN_x film deposition. 104

5.12 Measured optical power at constant current for (•) EG&G coated lasers, (o) McMaster coated lasers with an argon preclean. 107

5.13 Measured optical power at constant current for sulphur treated and coated lasers using the process for optimum PL enhancement. 108

5.14 Optical micrograph of laser facets after life testing for (a)the optimized process, and (b)the non-sulphur passivated facet. 109

A.1 Schematic diagram of the optical path traced in a Fabry-Perot semiconductor laser cavity. 119

List of Tables

2.1 Film parameters optimized for AR coating on a laser facet. 20

3.1 A comparison of the measured thicknesses and optical index of reference thin films with the actual values. 49

5.1 Gibbs energy of formation for GaAs oxides and aluminum oxide. and the heat of formation per O atom. 79

5.2 Typical test sequence for evaluating the impact of facet treatments on the performance of the laser. 92

Chapter 1

Introduction

Thin dielectric films can be used in several ways to improve the operating characteristics and versatility of a semiconductor diode laser (SDL) [1. 2. 3. 4]. Optical interference filters on a laser facet can be used to modify the net cavity round trip gain of a Fabry-Perot SDL and. as a result, can induce significant changes in the laser threshold and efficiency [5, 6], the spectral properties of the output [7], and the tuning characteristics [8]. As well, by acting as a passivating layer, the thin film coating can increase the high power reliability of the laser [9].

Three issues involving the application of dielectric coatings to laser facets will be addressed in this work. Diode lasers exhibit gain over a wide wavelength region under lasing conditions which results in an output wavelength spectrum which is not monochromatic, but characterized by several modes associated with the longitudinal laser cavity. The multimode spectral output limits the application of SDL's. For example. this is the cause of dispersion related distortion in optical communication systems. The random fluctuation of optical power between cavity modes, or mode partition noise, is mainly responsible for the poor signal to noise performance of diode lasers used in applications such as CD ROM read/write heads. An optical filter with a narrow reflectance band located within the gain bandwidth of the laser can increase

the cavity loss of the longitudinal modes which are not at the reflectance maximum. This will result in the suppression of optical power in these side modes, and the redistribution of this power to the mode nearest to the reflectance peak as shown in Figure 1.1

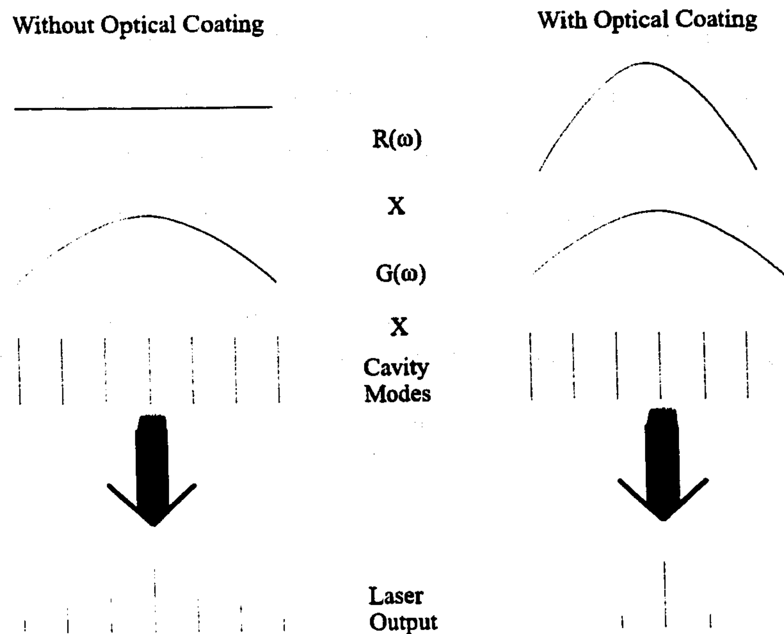

Figure 1.1: Effect of a narrow band filter with Reflectance $R(\omega)$ on the output spectrum of a SDL. $G(\omega)$ is the gain spectrum.

The non-monochromatic output spectrum caused by the broad gain bandwidth of the SDL, can be a significant advantage for some applications since it allows for an inexpensive tunable wavelength source. The longitudinal cavity modes can be removed by the application of an anti-reflection (AR) coating to the facet of the laser. If the reflection coefficient of the facet can be reduced from the uncoated value of approximately 0.32 to less then 1×10^{-4} by the anti-reflection coating, an external optical element can then be used to continuously tune the laser across the entire gain region of the laser material. For example, in many commercially available tunable

diode laser systems the optical feedback is provided by a grating element which is placed to couple reflected light back into the laser. The grating is rotated to tune the wavelength which is reflected back to the cavity. In order to obtain continuous wavelength tuning in these systems, the critical component is the quality of the AR coating on the laser facet.

An important limitation of SDL's which will be addressed in this Thesis is the high power limit of the devices. For the AlGaAs/GaAs material system in particular, at high optical powers the facet of the laser undergoes catastrophical optical damage which is due to a thermal runaway process associated with non-radiative recombination centers at the laser facet surface. It is known that a chemical treatment of GaAs surfaces using sulphur based compounds passivates these non-radiative recombination centers and greatly reduces the surface recombination velocity. Unfortunately, this surface treatment is sensitive to environmental contamination, and the passivation effect is not robust. By encapsulating the treated surface with an inert dielectric coating, such as silicon nitride, the sulphur passivation layer is protected from these contaminants and the passivation effect is seen to be significantly more stable. It is hoped that this improved surface quality will increase the laser reliability.

In this work, a process has been developed for the thin film coating of SDL facets using electron cyclotron resonance plasma enhanced chemical vapour deposition (ECR-PECVD) of silicon oxynitride (SiO_xN_y) and silicon oxide (SiO_x). Both silane (SiH_4) and an organic molecule, tris(dimethylamino)silane (TDAS, $C_6H_{19}N_3Si$) were used as silicon precursors. From measurements of the photoluminescence efficiency of coated and uncoated surfaces it was observed that the ECR-PECVD process induced little damage in the AlGaAs/GaAs laser facets. Precise measurements of the index of refraction and thickness of the single layers were made using an *in*

situ ellipsometer operating at 632 nm. Both step index and inhomogeneous multilayer structures were deposited using an automated gas delivery system which was developed as a component of this work.

The Thesis summarizing this work is divided into six chapters. The design of multilayer filters, with particular attention to the special case of interference filters on laser facets, is discussed in chapter 2. An accurate model of the reflectance of thin film filters illuminated by the diffracted optical beam from a laser waveguide [10] has been used to design interference filters for diode lasers. An analytical model of the laser spectral output [11] is used to understand and evaluate the effect of reflectance changes as a function of wavelength on the spectral output and noise properties of the coated laser. The materials properties of the thin films, along with details of the optical monitoring, and automation of the multilayer deposition process using *in situ* ellipsometry is discussed in chapter 3. The application of this process to the fabrication of optical coatings is discussed in chapter 4. Examples of high reflectance coatings, narrow band reflectance coatings and AR coatings applied to both standard silicon wafers and laser facets are described. In chapter 5 the surface properties of AlGaAs passivated using a sulphur based chemistry, and encapsulated with a silicon nitride coating are described. The effect of this treatment on the performance of high power AlGaAs/GaAs lasers is also discussed. Chapter 6 is a conclusion and summary of this work.

Chapter 2

The Design of Optical Interference Filters

2.1 Thin Film Optics

Thin film optical interference filters have been studied intensively over the past half century [12, 13, 14], and there are a number of detailed discussions of their analysis and design [12, 15, 16]. In the following, a brief description of these issues will be given. focusing on the applications which have been investigated in this work. The notation of reference [12] will be used.

In any medium. Maxwell's equations can be used to generate a wave equation for both the electric and magnetic field. Under most circumstances, the wave equation can be solved by a plane polarized harmonic function, the most convenient form of this function is the complex representation,

$$\mathbf{E} = \mathcal{E} exp[\imath(\omega t - Kx)], \tag{2.1}$$

which represents the electric field component of a plane wave of frequency ω propagating in the x direction with wavenumber K. Substituting this function into the wave equation for the electric field in a conducting medium,

$$\nabla^2\mathbf{E} = \varepsilon\mu\frac{\partial^2\mathbf{E}}{\partial t^2} + \mu\sigma\frac{\partial\mathbf{E}}{\partial t}, \tag{2.2}$$

yields the dispersion relation

$$K^2 = \omega^2 \varepsilon \mu - \imath \omega \mu \sigma. \tag{2.3}$$

ε is the electric permittivity, μ is the magnetic permeability, and σ is the conductivity of the medium. Note that the wavenumber can be a complex quantity. The permittivity and permeability can be expressed as $\varepsilon = \varepsilon_r \varepsilon_0$ and $\mu = \mu_r \mu_0$, with ε_0 and μ_0 the vacuum permittivity and permeability, and ε_r and μ_r the relative permittivity and permeability of the medium.

In vacuum, $\sigma = 0$ and the phase velocity of the wave, defined as $v = \omega / K$, is $v^2 = c^2 = 1/\mu_0 \varepsilon_0$. Equation 2.3 can be expressed as

$$\frac{c^2}{v^2} = \frac{\varepsilon \mu}{\varepsilon_0 \mu_0} - \imath \frac{\mu \sigma}{\omega \varepsilon_0 \mu_0}. \tag{2.4}$$

This defines the complex dimensionless index of refraction, N, for any medium as

$$N^2 = \varepsilon_r \mu_r - \imath \mu_r \sigma / \omega \varepsilon_0. \tag{2.5}$$

The complex number N is typically written as

$$N = n - \imath k \tag{2.6}$$

where n is the index of refraction referred to for the case of dielectric materials, and k is the extinction coefficient. Including this definition in equation 2.1 gives

$$\mathbf{E} = \mathcal{E} exp[-(2\pi k/\lambda)x] exp\{\imath[\omega t - (2\pi n/\lambda)x]\}, \tag{2.7}$$

where λ is the wavelength of the light in vacuum. For the wave described by equation 2.7, k represents absorption in the material. The amplitude of the electric field will decay by a factor of $1/e$ after propagating a distance of $\lambda/2\pi k$. In the medium, the phase of the wave will change by 2π after a distance $nx = \lambda$, rather than after

a distance $x = \lambda$. For this reason, the effective wavelength in the medium is λ/n, and nx, the optical distance, is more important than the physical distance, x, in the study of thin film filters.

The remaining physical characteristic of the electromagnetic wave which is of importance for the study of thin film filters is the optical admittance. It can be shown that, at optical frequencies, the magnetic and electric field of the wave are related,

$$\mathbf{H} = N\mathcal{Y}(\hat{s} \times \mathbf{E}). \tag{2.8}$$

$\mathbf{H}$ is the magnetic field, $\hat{\mathbf{s}}$ is the unit vector representing the direction of propagation, and $\times$ is the cross product operator. $N\mathcal{Y}$ is the ratio of the magnetic to electric field amplitude and has the dimensions of an admittance (Siemens, S), $\mathcal{Y}$ is the admittance of free space, and has a numerical value of $2.6544 \times 10^{-3} S$. By redefining the admittance units to free space units, where $\mathcal{Y}$ is unity, N represents the optical admittance directly.

The calculation of the overall reflectance and transmittance of a thin film structure is a repetitive calculation of the electric field reflection and transmission coefficients, or Fresnel coefficients, at each interface of the structure. Figure 2.1 shows a plane wave incident on an arbitrary multilayer film and defines the conventions used to calculate the reflection and transmission coefficients.

In general, the reflection of an arbitrary plane wave is quite complicated, with the incident and reflected or transmitted polarization states being different. The measurement of this change of polarization, and its interpretation, is the subject of chapter 3, where the ellipsometric measurement of the index and thickness of the deposited films is discussed. There are two polarization states which do not change upon reflection or transmission across a boundary, the state with the electric field perpendicular to the plane of incidence, transverse electric (TE or s), and that with

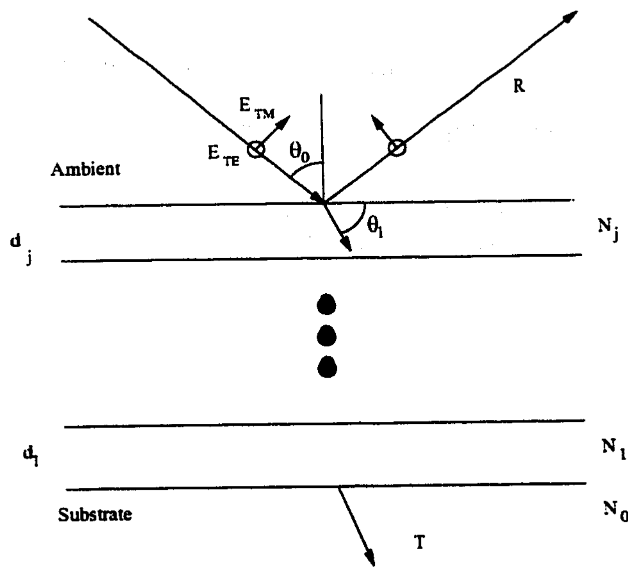

Figure 2.1: Schematic of a thin film optical filter

the magnetic field perpendicular to the plane of incidence, transverse magnetic (TM or p). Any incident wave can be decomposed into these component waves, and so there is a reflection and transmission coefficient calculated for both TE and TM waves. These equations are determined from the continuity of the tangential components of the electric and magnetic fields at the interface. For a single interface they are given by [12],

$$\rho_s = \frac{E_r}{E_i} = \frac{N_0 \cos\theta_0 - N_1 \cos\theta_1}{N_0 \cos\theta_0 + N_1 \cos\theta_1} \tag{2.9}$$

$$\tau_s = \frac{E_t}{E_i} = \frac{2N_0 \cos\theta_0}{N_0 \cos\theta_0 + N_1 \cos\theta_1} \tag{2.10}$$

$$\rho_p = \frac{E_r}{E_i} = \left(\frac{N_0}{\cos\theta_0} - \frac{N_1}{\cos\theta_1}\right)\left(\frac{N_0}{\cos\theta_0} + \frac{N_1}{\cos\theta_1}\right)^{-1} \tag{2.11}$$

$$\tau_p = \frac{E_t}{E_i} = \left(\frac{2N_0}{\cos\theta_0}\right)\left(\frac{N_0}{\cos\theta_0} + \frac{N_1}{\cos\theta_1}\right)^{-1}. \tag{2.12}$$

E_i, E_r and E_t are the components of the field parallel to the interface. As an example, for the case of p polarization, $E_i = \mathcal{E}_i \cos\theta_0$ where $\mathcal{E}_i$ is the amplitude of the incident

field.

The reflectance and transmittance are defined as

$$R = \left(\frac{\mathcal{E}_r}{\mathcal{E}_i}\right)^2 \tag{2.13}$$

$$T = \frac{N_1}{N_0}\left(\frac{\mathcal{E}_t}{\mathcal{E}_i}\right)^2. \tag{2.14}$$

Introducing the modified optical admittance,

$$\eta = H/E, \tag{2.15}$$

which is equivalent to $\eta = N\mathcal{Y}$ at normal incidence, and becomes

$$\eta_p = \frac{N}{\cos\theta} \tag{2.16}$$

$$\eta_s = N\cos\theta \tag{2.17}$$

for oblique incidence at angle θ, in all cases the reflection and transmission coefficients can be written as

$$\rho = \frac{\eta_0 - \eta_1}{\eta_0 + \eta_1} \quad \tau = \frac{2\eta_0}{\eta_0 + \eta_1} \tag{2.18}$$

$$R = \left(\frac{\eta_0 - \eta_1}{\eta_0 + \eta_1}\right)^2 \quad T = \frac{4\eta_0\eta_1}{(\eta_0 + \eta_1)^2}. \tag{2.19}$$

Note that when N is complex, the product of the complex conjugates of ρ and τ are taken to determine reflectance and transmittance.

Referring again to Figure 2.1, if the interference filter was reduced to a single layer on a substrate, only interface 0 and 1 would remain, and light would enter at an angle θ from the ambient air with admittance η_2. By considering the continuity of the fields at both interfaces, the values of both field components at the top interface can be related to those at the substrate interface by the following matrix equation,

$$\begin{bmatrix} E_1 \\ H_1 \end{bmatrix} = \begin{bmatrix} \cos\delta & (i\sin\delta)/\eta_1 \\ i\eta_1\sin\delta & \cos\delta \end{bmatrix} \begin{bmatrix} E_0 \\ H_0 \end{bmatrix}. \tag{2.20}$$

where δ is the phase thickness of the layer, and is given by

$$\delta = 2\pi N_1 d \cos\theta_1 / \lambda. \tag{2.21}$$

The ratio of the fields at the surface of the film/substrate system is called the characteristic admittance of the system Y, in analogy with equation 2.15. Again, the reflection coefficient and reflectance are written as,

$$\begin{aligned} \rho &= \frac{\eta_2 - Y}{\eta_2 + Y} \\ R &= \left(\frac{\eta_0 - Y}{\eta_0 + Y}\right)\left(\frac{\eta_0 - Y}{\eta_0 + Y}\right)^*, \end{aligned} \tag{2.22}$$

where "*" represents the complex conjugate. Using the characteristic admittance, equation 2.20 can be rewritten as

$$E_1 \begin{bmatrix} 1 \\ Y \end{bmatrix} = \begin{bmatrix} \cos\delta & (i\sin\delta)/\eta_1 \\ i\eta_1 \sin\delta & \cos\delta \end{bmatrix} \begin{bmatrix} 1 \\ \eta_0 \end{bmatrix} E_0. \tag{2.23}$$

Dividing by E_0, the admittance of the system can be calculated directly from equation 2.23. This method can be extended to an arbitrarily large number of layers by defining the characteristic matrix for each layer. The overall admittance is then the product of the matrices of all the layers taken from the one closest to the substrate to the top of the stack, multiplied by the complex vector representing the admittance of the substrate. The overall reflection coefficient and reflectance are then calculated using equation 2.22.

2.2 Typical Designs

In the last section it was shown that the reflectance and transmittance of multilayered thin film structures with complex indices of refraction can be calculated quite easily. The reflectance of inhomogeneous thin film structures, where the index of refraction

of the material varies continuously as a function of depth, can also be calculated accurately using the same technique, if the continuous index is discretized on a fine enough scale. A short computer program to perform this calculation has been written to assist in the design of optical filters.

The more difficult problem is determining the type of thin film structure required in order to obtain a specific reflectance vs wavelength characteristic. There are many discussions of the design of filters for specific applications in the literature [17, 18, 19]. A relation between the reflectance spectrum, and the spatial Fourier transform of the thin film structure exists [17], however, in general, there is no simple way to invert the problem solved above to calculate the optimum layer structure based on the desired refectance. Normally, numerical optimization techniques or intuition and experience are required in the design process.

The fundamental building block of any homogeneous filter is the quarter wave layer. The phase change of light at the wavelength of interest passing through this layer is $\pi/2$. Light which has passed through the film and is reflected at the lower interface interferes with light reflected from the surface of the layer. For this particular wavelength, the relative phase of the two components is either 0 or π, depending on whether the layer below the quarter wave layer has a higher or lower refractive index. A single layer on a higher index material results in destructive interference of the two components, and produces a low reflectance zone for wavelengths where the phase thickness is near a quarter wave. High reflectance filters are made by several periods of high and low quarter wave layers, so that a region of constructive interference centered at the quarter wave region produces a high reflectance band. This reflectance spectrum is analogous to an electron band gap in a solid, and is sometimes referred to as a photonic band gap.

Because the wavelength at which a layer is a quarter wave thickness is so important in the design of any filter, reflectance spectra are often calculated using a scale normalized to this wavelength. The quarter wave unit, g is defined as

$$g = \frac{\lambda_0}{\lambda}, \tag{2.24}$$

where λ_0 is the design wavelength at which the optical thickness of the film is a quarter wave, $nd/\lambda_0 = 0.25$. The phase thicknesses of the layers in the filter at different wavelengths are then quoted in terms of g,

$$\delta = 2\pi \frac{nd}{\lambda_0} g. \tag{2.25}$$

2.2.1 Anti-Reflection Coatings

As mentioned in the Introduction, in order to continuously tune the wavelength of a SDL by some external means, the longitudinal modes associated with the cavity of the laser itself must be suppressed. This requires an optical coating on the laser facet with a reflectance below 10^{-4} over the tuning range of the laser. For normal incidence plane wave illumination, the simplest anti-reflection (AR) coating design which theoretically achieves zero reflectance is the single quarter wave layer which has an index of refraction which is the geometrical mean of the substrate and ambient medium index, $n_{film} = (n_{amb} n_{sub})^{1/2}$. At the design wavelength, this layer transforms the admittance of the substrate to that of the ambient medium, and hence there is a perfect impedance match of the layer structure and ambient, with no reflection. The index of refraction of typical laser materials ranges from 3.2 to 3.7, so that the required index of refraction of the coating material ranges from about 1.79 to 1.92. This index range is accessible using silicon oxynitride as the dielectric coating material, which can be deposited with refractive indices ranging from 1.46 up to 1.95.

A dramatic improvement in the performance of AR coatings is obtained by using two layers rather than one. A method for the design of a two layer AR coating is described in reference [12]. The technique is based on Smith's method of effective indices [20] and consists of dividing the system into two subsystems with a medium of index η_i in between as shown in Figure 2.2. The overall transmission coefficient of the structure can be expressed as a function of the reflection and transmission coefficients of the subsystems a and b,

$$T = \left(\frac{T_a T_b}{(1 - R_a^{1/2} R_b^{1/2})^2}\right) \times \left(1 + \frac{4R_a^{1/2} R_b^{1/2}}{(1 - R_a^{1/2} R_b^{1/2})^2} \sin^2\left(\frac{\phi_a + \phi_b - 2\delta}{2}\right)\right)^{-1} . \quad (2.26)$$

where ϕ_a and ϕ_b are the phase of the reflection coefficient at interface $a - i$ and $i - b$ respectively, and δ is the optical thickness of the imaginary layer i. In order to obtain $T = 1$ each of the two terms in equation 2.26 must be 1. The first term is unity if $R_a = R_b$ and the second term is unity if

$$\sin^2\left(\frac{\phi_a + \phi_b - 2\delta}{2}\right) = 0. \quad (2.27)$$

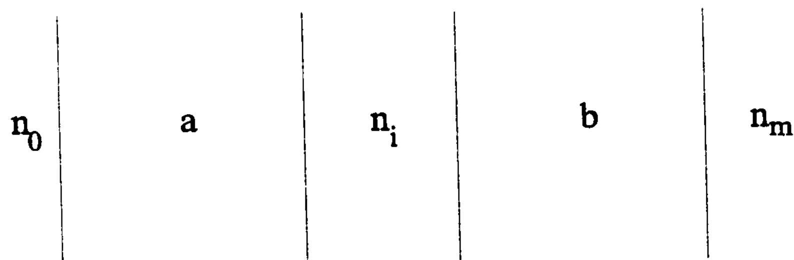

Figure 2.2: Multilayer AR coating consisting of two subsystems a and b separated by a central layer i.

One of the properties of the characteristic matrix of equation 2.20 is that it is unchanged if the admittance of the layer is multiplied by a constant factor without any change in the optical thickness. As a result, the reflectance of any multilayer

structure is unchanged if all of the layer admittances are multiplied by a constant factor. If each subsystem is assumed to be a single layer, the reflectance R_a can be made equal to the reflectance R_b if the following relations hold

$$\frac{\eta_0}{\eta_i} = \frac{\eta_a}{\eta_b} = \frac{\eta_i}{\eta_m}. \tag{2.28}$$

As a result

$$\eta_i = (\eta_0 \eta_m)^{1/2} \tag{2.29}$$

and

$$\eta_b = \eta_a (\eta_m/\eta_0)^{1/2}. \tag{2.30}$$

For any chosen index in layer b there is a corresponding index for layer a which matches the reflectances of the two subsystems. This layer structure results in a reflectance of zero only for wavelengths where the phase condition described by equation 2.27 is true. A simple way to satisfy this condition is to choose a quarter wave optical thickness for each of the layers a and b and to allow the thickness of layer i to go to zero. Also, the width of the low reflectance zone is highest if the lowest value of η_a is chosen.

Figure 2.3 shows the calculated reflectance spectra of a single layer coating and a two layer AR coating with $n_a = 1.46$ and $n_b = 2.846$ on a substrate with $n_m = 3.8$. For the single layer coating, the width of the low reflectance region (R $< 10^{-4}$) is approximately 30 nm. This is about the same as the gain bandwidth of the laser. and even a perfect coating will result in observation of the cavity modes in the output spectrum of the laser. By using two layers in the design, the width of the minimum reflectance is increased by a factor of more than 4. This is particularly important for applications where the laser is to be continuously tuned over a wide wavelength range [21].

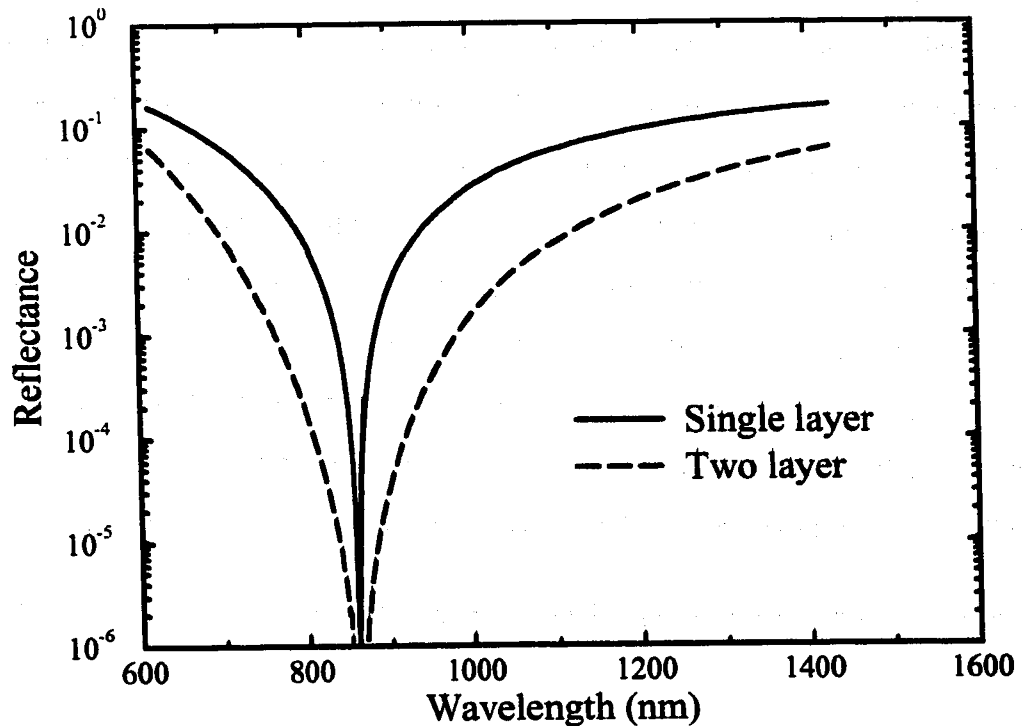

Figure 2.3: Reflectance spectrum of both a single layer and two layer AR coating.

The reflectance spectra for the AR coatings discussed above were generated using the matrix method summarized in section 2.1, however this analysis assumes that the light illuminating the filter is collimated and enters the filter either at normal incidence, or at some specific angle. As alluded to in the Introduction, the design of optical filters for SDL facets is complicated by the fact that the light illuminating the filter is the diffracted elliptical beam from the laser waveguide. The geometry of the situation which must be considered is shown in Figure 2.4. This optical beam can be represented as a superposition of plane waves propagating at different angles of incidence into the filter. Each plane wave component has a specific spatial period along the x direction. The amplitude of each plane wave component is determined

by the spatial Fourier transform of the waveguide mode. For a more confined waveguide mode the diffraction of the beam will be greater, and higher angle plane wave components will illuminate the filter.

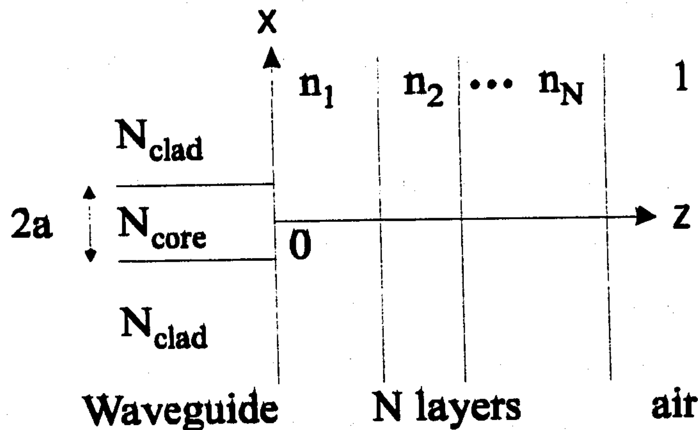

Figure 2.4: Reflection of light from a waveguide by a thin film optical filter.

To determine the reflection coefficient of a filter/waveguide combination exactly, one would have to consider a solution of Maxwell's equations for this complicated 3 dimensional boundary value problem. One very good assumption which makes the problem tractable is that the lateral (y) confinement of the waveguide is significantly less than the transverse (x) confinement, so that diffraction of the waveguide output is stronger in the transverse direction than in the lateral direction. With this assumption the variation of the field as a function of y is ignored and the problem is reduced to 2 dimensions.

There have been several numerical calculations of the reflection coefficient of uncoated or anti-reflection coated laser facets [10, 22, 23, 24, 25, 26]. The most detailed and complete study of this problem was reported by Vassallo [10]. In this work, a rigorous calculation of the reflection coefficient of a symmetric waveguide mode is carried out. In addition, a first order approximation to the solution is given. This

solution is accurate enough to be used for the design of AR coatings with properties practically identical to the coating properties calculated from the rigorous method. A computer program was written to perform the approximate calculation of the reflectance from a laser facet in order to compare it with the plane wave calculation. As an indication of the accuracy of the approximate algorithm, Figure 2.5 compares the results of the approximate method with those calculated by Vassallo's rigorous method. The optimal index of refraction which is required for minimum reflectance is calculated as a function of the thickness of the active region of the laser structure shown in the inset. In Figure 2.5, the difference between the calculated index and the true index which results in a reflectance of 10^{-5} is indicated. By comparing the approximate and rigorous calculations, it can be seen that the error in the optimum index results in a residual reflectance which is less than 10^{-5} for all cases, and so the numerical calculation can be taken as accurate for practical purposes.

Figure 2.6 shows the impact of including the accurate illumination from the waveguide. In the figure, $n_{clad} = n_{core}(1-\zeta)$, therefore, ζ represents the confinement of the waveguide. The reflectance of a single layer AR coating designed assuming a weakly confined waveguide illumination is compared with the reflectance of the same filter when illuminated by a more strongly confining waveguide. Obviously it is important to include this effect in the design of AR coatings if a reflectance of 10^{-4} is desired at the operating wavelength.

One approach to the design of multilayer filters for laser facets is to take a design determined by the standard techniques, which neglect the waveguide illumination, and then modify the individual layers in such a way that the reflectance spectrum of the waveguide illuminated filter becomes equivalent to the original reflectance spectrum. A simple error term which represents the difference between the

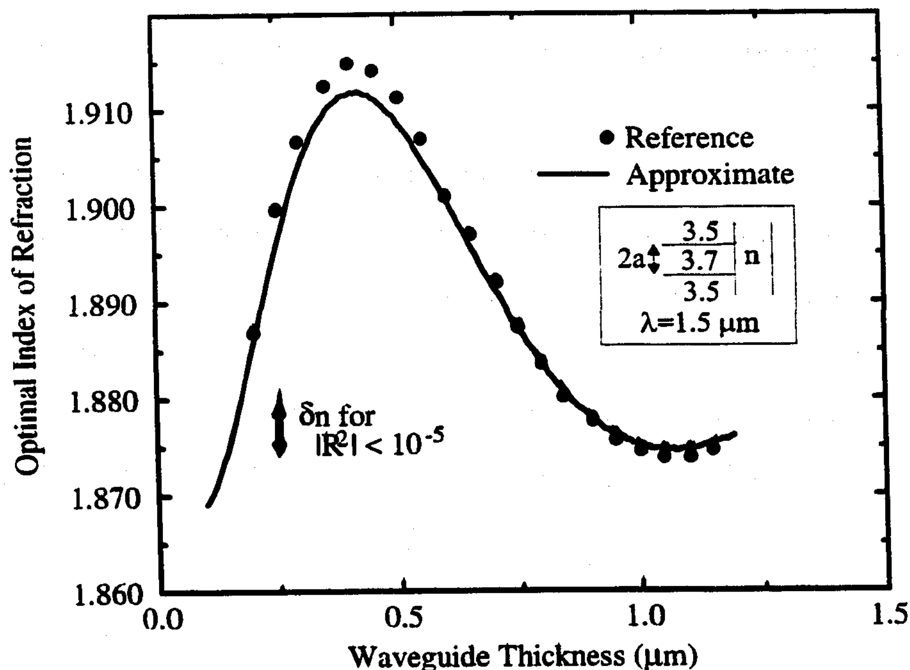

Figure 2.5: A comparison of the rigorous and approximate methods for calculating the optimum index of refraction for an AR coating.

desired and actual spectrum over the wavelength region of interest (from λ_i to λ_f) can be defined as

$$\epsilon = \sum_{\lambda_i}^{\lambda_f} |R_{wg} - R_{pw}|, \tag{2.31}$$

where R_{wg} is the reflectance calculated including the waveguide illumination, and R_{pw} is the reflectance calculated assuming plane wave illumination. For a given waveguide structure. the reflectance spectrum depends only on the thicknesses and refractive indices of the layers which comprise the filter. By iteratively varying these parameters such that the error term is minimized, the transformation of the original design to one which has the desired reflectance characteristics on a laser facet is possible.

In order to verify the accuracy of the algorithm, an optimization of a single

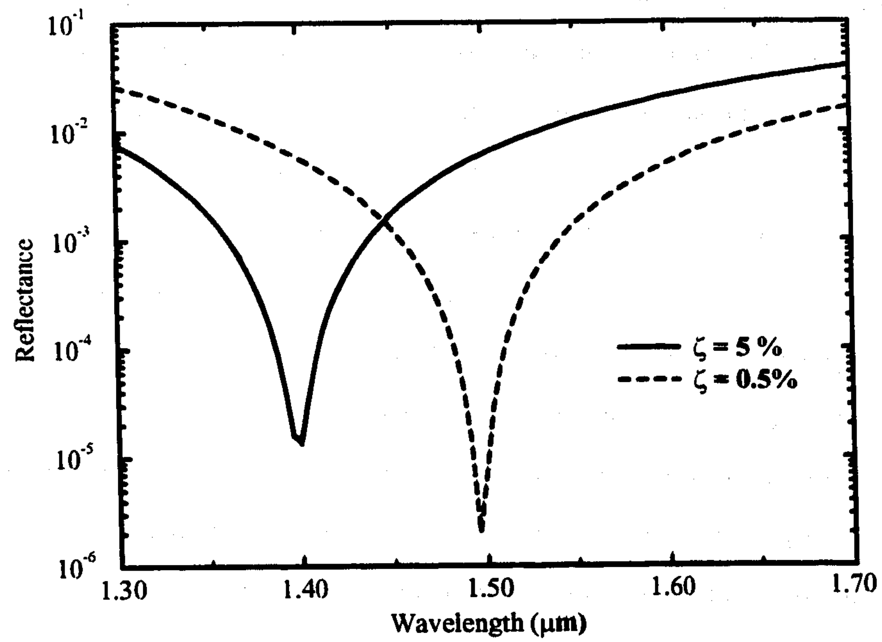

Figure 2.6: The effect of illumination on the reflectance of light from an AR coated laser facet.

layer AR coating was performed. The desired reflectance spectrum has a zero at 1500 nm. and the waveguide structure is the same as that referred to in Figure 2.5 with an active layer thickness of 0.4 μm. The optimization process produces a value of 1.9124 for the index of the AR coating, and a thickness of 2098.4 Å as the required parameters for the layer. Referring to Figure 2.5, the index agrees with that calculated by simply minimizing the reflectance at the desired wavelength.

The same algorithm can be used for multilayer film structures. Figure 2.7 shows the result of optimizing a wide band AR coating consisting of two layers on the same waveguide structure. The optimized film parameters obtained from the algorithm are listed in table 2.1. The AR bandwidth for the optimized filter on a laser facet is slightly narrower than the original design with plane wave illumination,

Layer	n	t [Å]
air	1.0	
SiO_2	1.4749	2703.0
SiO_x	2.7490	1392.7

Table 2.1: Film parameters optimized for AR coating on a laser facet.

however the region with $R < 10^{-4}$ is still more than 180 nm wide.

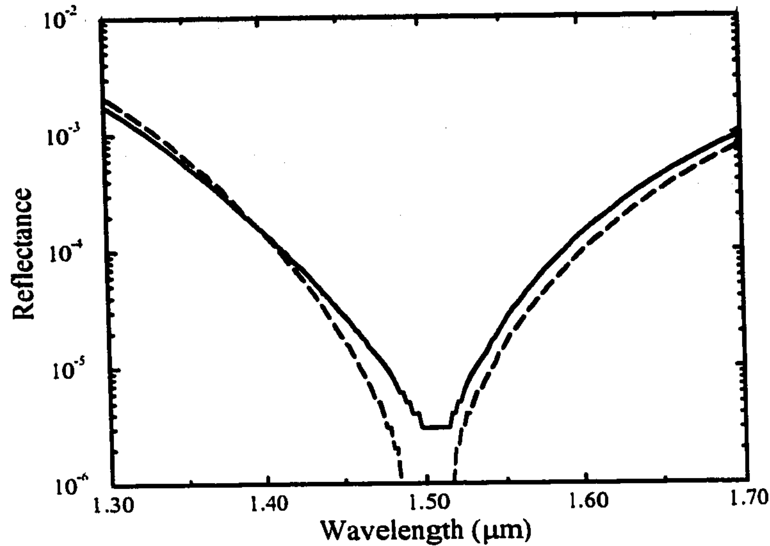

Figure 2.7: The result of optimizing a two layer AR coating for a waveguide structure.

In the literature, two layer AR coating designs have been optimized for specific laser structures [21]. Due to a limited availability of materials with the appropriate index of refraction, the high index layer was replaced with an equivalent two layer structure. The resulting design had a reflectance below 10^{-4} over a wavelength range of nearly 150 nm at a center wavelength of 1550 nm. The measured low reflectance bandwidth of the fabricated filter was approximately 100 nm.

2.2.2 High Reflection Coatings

The second important application of interference filters as facet coatings for SDL's is as a high reflection coating to reduce the threshold current and increase the differential quantum efficiency of the laser. Figure 2.8 shows the reflectance spectra for various quarter wave stack high reflectance filters. There are two main parameters to adjust when designing a quarter wave stack, i. e., the index difference between the high and low refractive index layers, or the index contrast, and the number of periods. It can be shown that the width of the high reflectance band depends only on the index contrast [12].

$$\Delta g = \frac{2}{\pi} \sin^{-1} \left(\frac{n_H - n_L}{n_H + n_L} \right), \tag{2.32}$$

where Δg is the half width of the reflectance band measured in quarter wave units. The other significant design criterion is the number of layers required to obtain a specific reflectance. Each addition of a high/low period to the quarter wave stack increases the effective admittance of the substrate (at $g = 1$) by a factor $(n_H/n_L)^2$. To obtain high reflectance, the effective admittance of the substrate must be significantly higher than 1. As a consequence of this, the total number of layers in a design requiring a high reflectance increases dramatically as the index ratio is reduced. The filters discussed here can be divided into two basic types, i.e., narrow reflectance band (NB) filters and wide reflectance band (WB) filters, depending on the index contrast.

As for the AR coating case, it is important to include the waveguide illumination effects in the calculation of the reflectance spectra for multilayer coatings, particularly the NB filters. Figures 2.9 and 2.10 show the change in the reflectance spectra for a NB high reflectance filter and for a WB high reflectance filter, respectively. The effect is very significant for the NB filter, and only slight for the WB filter. Note that the overall thickness of the NB filter is nearly a factor of 4 greater than

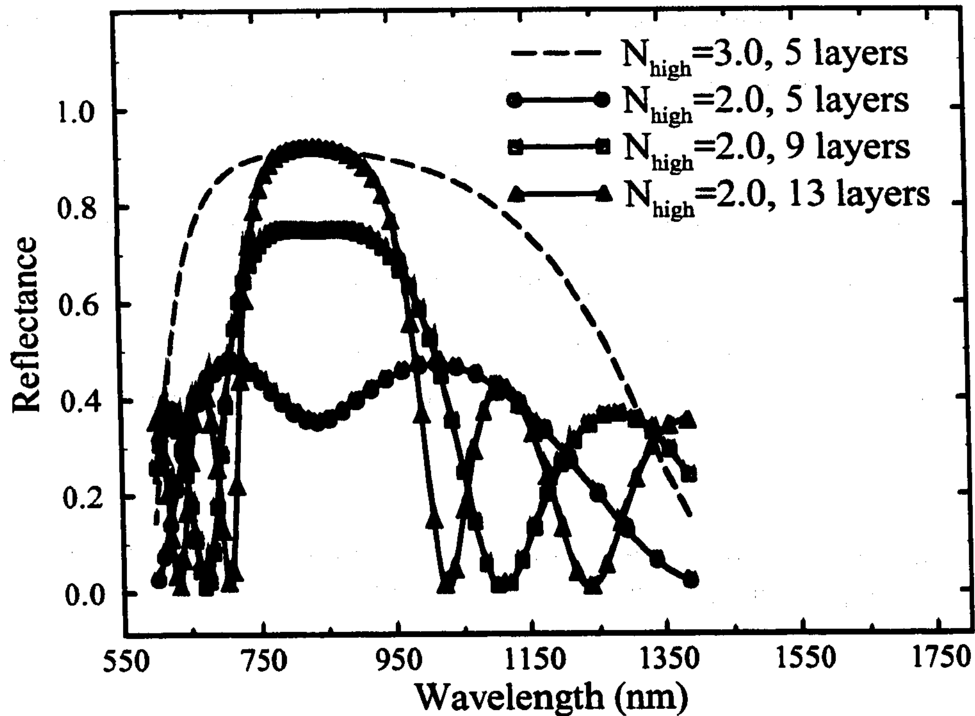

Figure 2.8: Reflectance spectra for quarter wave stack HR filters showing the effect of variations in the index contrast ($n_{high} - n_{low}$) and the number of periods. In all cases $n_{low} = 1.46$.

...r the WB filter. For plane wave illumination of the NB filter, as more ... periods are added, the reflectance builds up and approaches 1.0, however, when the reflectance of the filter is calculated for waveguide illumination the layers which are farther from the facet contribute less to the reflectance, and the build-up of the stop band is not as pronounced.

For the design of AR coatings, an interesting conclusion which was drawn from modelling the laser facet reflectance accurately, is that even though there is a significant component of the light from the laser propagating within the filter at non-

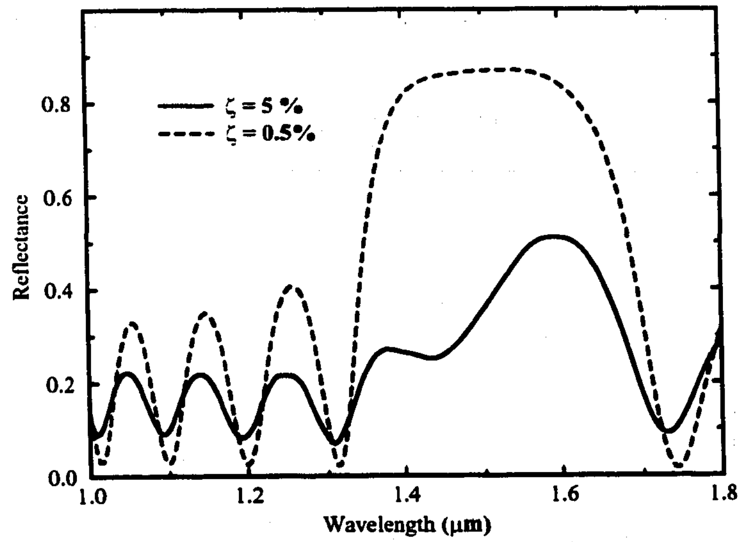

Figure 2.9: The effect of illumination on the reflectance of light from a laser facet coated with a narrow band interference filter.

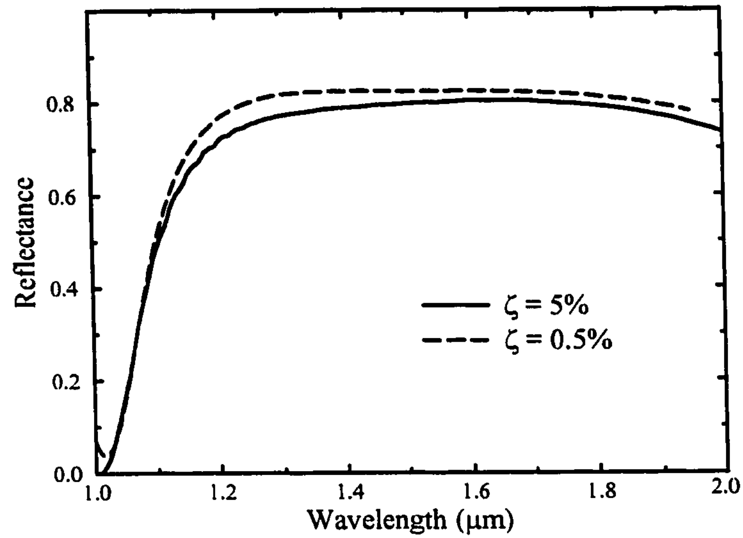

Figure 2.10: The effect of illumination on the reflectance of light from a laser facet coated with a wide band interference filter.

normal angles of incidence, it is still possible to obtain no reflectance from the facet using a single layer optical coating. This is somewhat counter-intuitive, since it would seem that matching all of the different plane wave components at once would be an impossible task. The accurate modelling of more complicated interference filters on laser facets may indicate that other new effects can be produced. As mentioned earlier, the issue of AR coating has received much attention in the literature for the past several years, however, the use of optical filters on laser facets for other applications has not been studied to the same extent. Optical filters have been used to achieve more novel modifications of the operating characteristics of SDL's. For example, filters deposited directly on the laser facet have been used to improve the thermal stability of a semiconductor laser [3]. Also, an external thin film Fabry-Perot transmission filter was used in conjunction with a mirror to improve the operation of an external cavity laser [27]. In another report, a standard AR coating was applied to one facet, while a coating was applied to the opposite facet which had increased reflectivity at wavelengths where the gain of the semiconductor was reduced. This resulted in a reduction of threshold current changes as the semiconductor laser wavelength was tuned [28].

A single layer coating on a laser facet with a large optical thickness will result in a modulation of the reflectance which is quite rapid. This can have the same effect as a NB high reflection coating, however, it is much simpler to fabricate. The laser properties which result from such a coating will be discussed after the effect of a wavelength dependent facet reflectance on the spectral properties of a SDL is considered.

2.3 Effect of the Optical Coating on Laser Properties

In this section, the effect of the various optical coatings discussed above on the output characteristics of SDLs is described. The three filter designs were discussed in section 2.2. AR coatings and WB high reflection coatings are used in standard manufacturing processes, and are critical to the production of external cavity lasers and high power lasers, respectively. The use of a NB filter on a laser facet to modify the spectral characteristics of a laser is a more difficult problem which has not been investigated. The principle was mentioned in chapter 1, and is simply to use the interference filter to produce a change in the cavity loss in the semiconductor laser such that one longitudinal mode of the laser experiences a significantly lower loss than the others, resulting in a high selectivity for that mode.

The effects of the optical coating on the properties of the laser can be separated into two parts, i. e., effects due to the magnitude of the filter reflectance and effects due to the phase of the filter reflectance. The effect of the phase is to change the condition for constructive interference in the Fabry-Perot cavity, which defines the frequency of the longitudinal modes of the laser. The frequency of the peaks of the Fabry-Perot transmission spectrum for a cavity with optical coatings must satisfy the relation

$$\sin[2nk_0L + \phi] = 0, \tag{2.33}$$

where L is the cavity length, k_0 is the wavenumber of the laser, and ϕ is the sum of the phase introduced by reflection from the two facets of the laser as shown in Figure 2.11. As a result the longitudinal modes occur at frequencies

$$\nu_m = \frac{mc}{2n(\nu)L} - \frac{\phi(\nu)c}{4\pi n(\nu)L}. \tag{2.34}$$

Note that the frequency dependence of the refractive index of the material and the phase of the filter has been shown explicitly. The change in frequency between modes can be calculated (including the dispersion of index and reflection phase) giving

$$\Delta\nu = \frac{c}{2\left(n_g - \frac{\lambda^2}{4\pi L}\frac{\partial\phi}{\partial\lambda}\right)L}, \tag{2.35}$$

where n_g is the group index. $\partial\phi/\partial\lambda$ is positive for most filter designs over the wavelength region of interest, and so the effect is generally to increase the spacing between longitudinal modes. For most cases the effect is smaller than 1 % and can be ignored.

More significant is the effect of the variation of the magnitude of the reflectance with wavelength introduced by the optical filter. To investigate these effects, a realistic model which calculates the output spectrum of a semiconductor laser [11] was modified to include a variation of the facet reflectance with wavelength. This model was used to investigate the effect of various filter designs on the output spectrum of the laser. A brief description of the model is given in appendix A. Referring to Figure 2.11, the expression for the power in a given mode, I_m, is

$$I_m^{\pm} = \frac{<\delta_m^2> (1 + R_m^{\mp} G_m)}{1 - R_m^{+} R_m^{-} G_m^2}, \tag{2.36}$$

where $\pm$ refers to the direction of propagation, either toward the left or right, and δ_m is the time averaged intensity of the spontaneous emission coupled into the mode m. $R_m^{\pm}$ is the reflection coefficient for the mode at facet $\pm$, and G_m is the intensity gain during a single pass for this mode. For convenience the + facet will be referred to as the front, and the − facet as the back facet of the laser. In the following discussion, the front facet of the laser is assumed to be coated with a wavelength selective filter, while the back facet is assumed to have a constant reflectance. The gain of a mode depends on the total intensity of all modes, and so the calculation of the mode powers

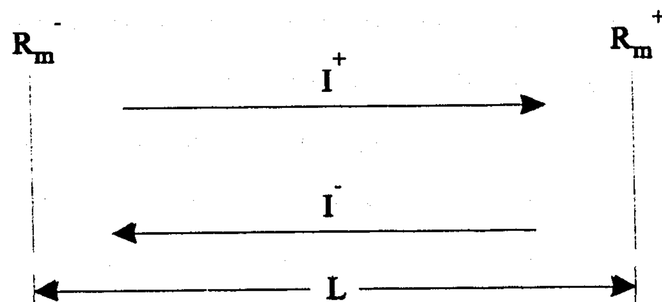

Figure 2.11: Schematic diagram of the optical path traced in a Fabry-Perot semiconductor laser cavity.

requires the solution of a coupled set of equations. The denominator in equation 2.36 determines the intensity of a given mode to a large degree. Above the threshold current, the product of $(R_m^+ R_m^-)^{1/2} G_m$ approaches 1 for the dominant mode. The supression of the remaining modes is determined by the amount of change which can occur in the "RG" product of the adjacent modes.

From numerical simulations, it has been observed that there does not appear to be a strong sensitivity of the side mode supression ratio (SMSR) to the average facet reflectances. The average facet reflectances do control the threshold current and differential quantum efficiency of the laser, and so it is more important to design coatings with average reflectances chosen to optimize these parameters. The most efficient output of optical power is obtained when the laser is coated on one facet with a high reflectance filter ($R \approx 95$ %) and the opposite facet with an AR filter ($R \approx 5$ %) [5, 6]

Figure 2.12 shows the effect of a small increase in the reflectance of one cavity mode on the SMSR observed in the laser output spectrum. It can be seen that even an increase of 0.5 percentage points in the reflectance of the central mode increases the SMSR by nearly two orders of magnitude. The spectra were calculated at a current pump rate of twice the threshold current, and with values of $R_m^- = 0.95$ for all m and

$R_m^+ = 0.05$ for all m except the central mode where the gain is a maximum.

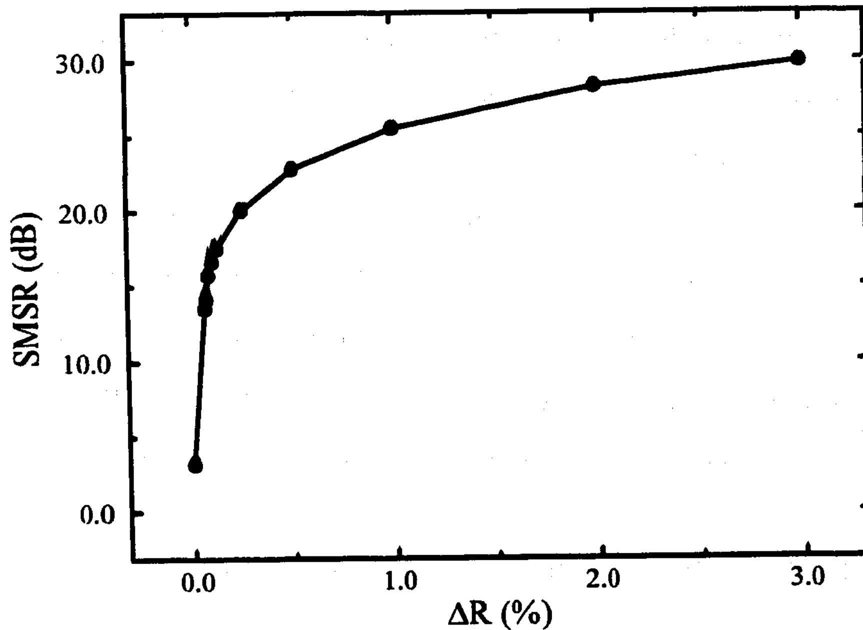

Figure 2.12: Calculated SMSR versus the difference in modal reflectance.

The laser can also be forced to oscillate off of the gain peak by a similar increase in the reflectance of a non central mode. Because the temperature variation of the refractive index of typical dielectric materials is small compared to a semiconductor. this would mean that the temperature and current tuning observed in a standard laser due to wavelength shifts in the gain peak can be reduced.

As mentioned, the simplest method for producing a narrow reflectance band is to deposit an optically thick single layer coating. The index of refraction must be chosen to be as large as possible, to increase the optical thickness for a given physical thickness, but must be low enough that there is a significant modulation of the reflectance. From numerical simulations, the optimum index of refraction is found

to be near 2.0. Figure 2.13 shows the expected SMSR as a function of the thickness of the optical coating for a 1550 nm laser with a longitudinal mode spacing of 1.2 nm. The calculations were performed with the laser operating at $1.5I_{th}$.

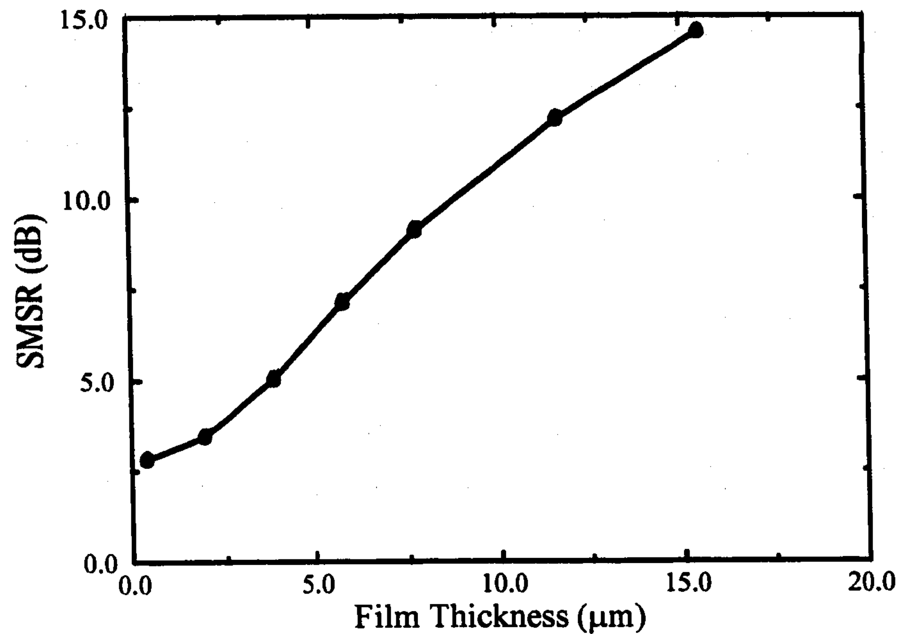

Figure 2.13: Calculated SMSR versus the optical coating thickness.

In order to obtain significant side mode surpression a very thick film is required, making the practical application of this technique challenging. However, it has been observed that there is a significant reduction in the amount of intensity noise in the optical output of the laser as the SMSR is reduced through the use of feedback from an external optical element [29]. In this study it was observed that by increasing the SMSR from 13 dB to 19 dB the relative intensity noise at low frequencies (below 50 MHz) was reduced by two orders of magnitude. For communications applications, the typical specification for the SMSR of distributed feedback lasers is 30 dB. Al-

though it does not seem reasonable to expect this performance from the application of a thin film filter to a simple Fabry-Perot laser, the high sensitivity of the laser noise to the SMSR indicates that attempts to increase this parameter could prove useful in applications where a low cost reduction in laser intensity noise is necessary, but not to the degree required for communications applications.

Chapter 3

Fabrication of Multilayered Structures

3.1 Introduction

In this chapter, the implementation of the designs described in chapter 2 is discussed. The structures were deposited using an electron cyclotron resonance plasma enhanced chemical vapour deposition (ECR-PECVD) system. The deposited layers were amorphous silicon and silicon oxynitrides, with refractive indices varying from 3.3 to 1.46. A run to run reproducibility in the index of refraction of 0.008 and a thickness control of ±10 Å were obtained using an in situ ellipsometer for optical monitoring.

3.2 Plasma Characteristics

A detailed description of the plasma characteristics of the ECR-PECVD reactor has been given previously [30]. The films are formed by cracking various silicon precursors in a mixed plasma of argon, oxygen and nitrogen. The parameters which can be varied to affect the film properties are the microwave power used to sustain the discharge, the pressure maintained in the chamber during deposition, the profile of the magnetic field, the temperature of the substrate, and the composition of the

gases used in the discharge. Figure 3.1 shows a schematic diagram of the ECR-PECVD system. The microwave power source, waveguide coupler. microwave tuning stubs, and the quartz window through which the microwave energy is coupled, are indicated in the figure. The plasma gases are introduced in the upper dispersion ring, and activated by the resonant absorption of the microwave energy at the position below the quartz window where the magnetic field satisfies the cyclotron resonance condition, $eB_{res}/2\pi m = 2.45$ GHz, with e the electron charge, B_{res} the appropriate magnetic field in Gauss, and m the electron mass. For this case, B_{res} corresponds to a magnetic field of 875 Gauss. The silicon precursor, either TDAS or Silane, was introduced below the plasma generation region, close to the sample. The path of the silicon precursor to the surface from the dispersion ring is quite direct, involving only a small number of activating collisions. As a result, care must be taken in the design of the gas dispersion ring to ensure that an even distribution of the silicon source is delivered from this dispersion ring so that a reasonable film uniformity can be obtained. For all the experiments discussed in this work, the pressure in the chamber during deposition was maintained at 2 mTorr, the currents in the upper and lower magnets were set to 180 and 115 A respectively, the microwave power ranged from 500 W up to 1200 W, and the substrate temperature was generally kept below 300 °C. There was a linear relationship between the chamber operating pressure and the gas flow rates with slightly different proportionality constants for the different gases. Because of this. the total gas flow rate during a deposition was generally between 15 and 20 sccm. depending on the gas mixture. Reliable control of the film refractive index was only achieved when the base pressure of the chamber was kept below 10^{-7} Torr. after baking the chamber walls a pressure of 5×10^{-8} Torr was obtained.

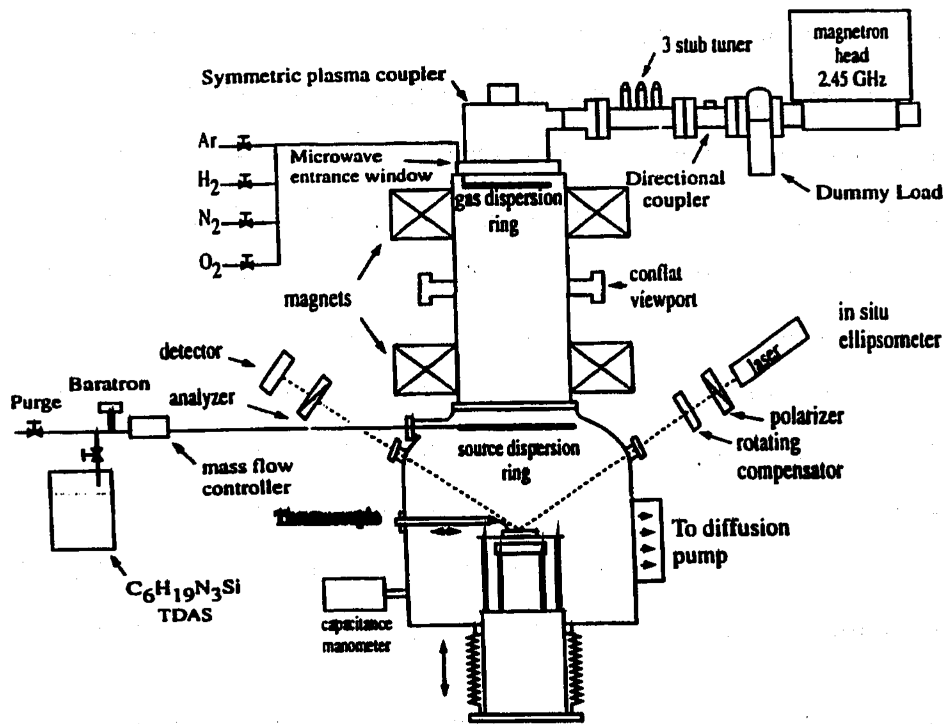

Figure 3.1: A schematic diagram of the ECR-PECVD system.

The surface temperature during deposition is a critical parameter, since significant damage occurs to InP, for example, when exposed to a 1000 W argon plasma even though the deposited film quickly passivates the surface. The thermocouple used to monitor the substrate temperature was originally placed below the sample, and was unable to measure the substrate temperature accurately during plasma exposure [30]. In order to accurately measure this temperature, a shielded Tungsten/Rhenium thermocouple was installed such that it could be placed in contact with the substrate during a deposition, as indicated in Figure 3.1. Figure 3.2 shows the surface temperature measured with the thermocouple as a function of the time after the plasma initiation for plasmas generated from argon and oxygen. The higher temperature is obtained in the argon plasmas, due to ion bombardment from the heavy argon atoms,

however, in all cases significant plasma heating of the substrate takes place.

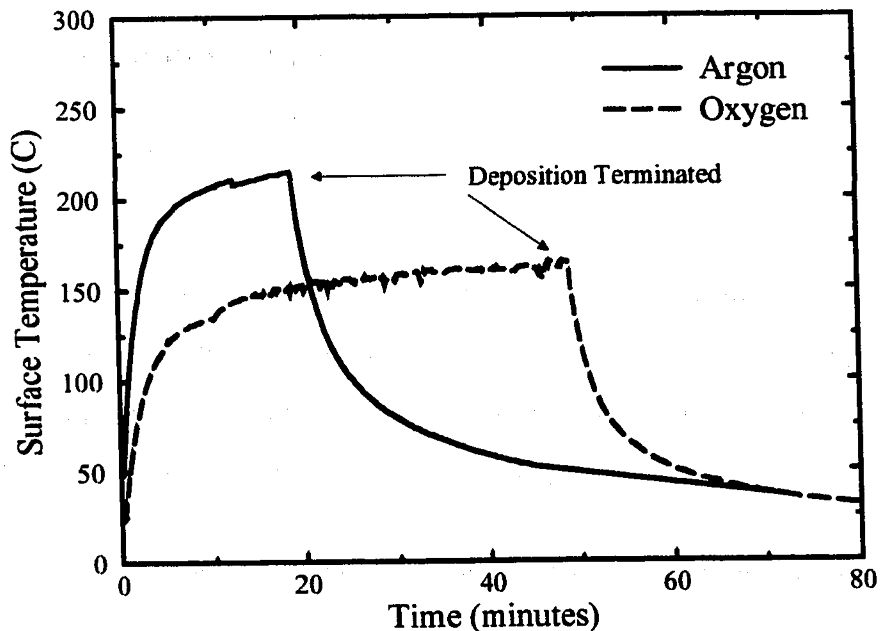

Figure 3.2: Measured temperature versus time for different plasma gases.

The surface temperature is also affected by the microwave power coupled to the plasma. The power must be high enough to maintain an overdense plasma, which allows for much more efficient coupling of the microwave energy to the plasma. Above this power level, however, the surface temperature increases approximately linearly with microwave power.

3.3 Material Properties

3.3.1 Experimental Details

In order to evaluate the material quality of the thin films used in these experiments several characterization techniques were used. The composition and structure of

the films were investigated by Fourier transform infrared spectroscopy (FTIR) and elastic recoil detection (ERD) [31]. The etch rate in a buffered HF solution (6:1 NH_4F:HF) was used to measure the relative density and chemical stability of the films. The surface quality and morphology of the films were determined using atomic force microscopy (AFM) and scanning electron microscopy (SEM).

For the FTIR measurements double side polished wafers were used to avoid scattering from the rough back surface of the wafer. Frequency dependent absorption due to free carriers in the semiconductor was eliminated by using high resistivity substrates ($\rho > 30$ Ωcm). The absorbance of the films was measured over a frequency range from 4000 cm^{-1} to 400 cm^{-1}. Which allowed the detection of both the hydrogen related absorption peaks as well as the absorbance associated with the heavier film components. To increase the sensitivity of the measurement, films of a thickness greater than 400 nm were analyzed. The resolution of the spectrometer was set to 8 cm^{-1}, and 16 scans were averaged in order to obtain each spectrum. Absorption features associated with CO_2 and H_2O contamination of the optical path in the interferometer were avoided by purging in a dry nitrogen environment.

The ERD technique is a very powerful method for determining the complete composition, including the hydrogen content, of many material systems, and in particular for these silicon based dielectric films. The technique is based on the forward scattering of atoms from the film due to heavy ion bombardment, and the subsequent measurement of both the energy and mass of the scattered species using a single detector. The yield of atoms of a particular mass as a function of energy gives information on the depth profile for that atom in the film. In the measurements performed on this material a 230 MeV ^{209}Bi ion beam was used. The geometry of the measurement is shown in Figure 3.3, with the detector at an angle, ξ, of 45° relative to the

surface. The forward scattered ion detector design was optimized for high sensitivity, so that a high signal to noise ratio could be obtained with a low radiation dose at the sample. The analysis of the detector signal is very complicated, and is described more completely in Wallace [31]. The absolute accuracy of these measurements is approximately 5% of the indicated concentration.

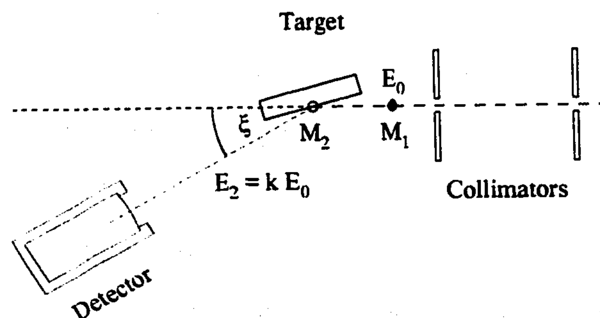

Figure 3.3: The geometry used for the ERD measurements.

The main silicon precursor used to deposit SiO_xN_y was tris(dimethylamino)silane. This molecule contains both silicon and nitrogen atoms, with the nitrogen directly bonded to the silicon, as is shown in Figure 3.4. In situ studies of reactive radicals in radio frequency plasma enhanced CVD processes have shown that radicals very similar to TDAS form in the gas phase during the deposition of silicon nitride films in plasmas composed of ammonia and silane [32]. Due to this molecular structure, SiO_xN_y films with refractive indices ranging from 1.95, for SiN_x , to 1.46, for SiO_2, could be deposited, however, processes using TDAS could not be used to produce higher index films such as amorphous silicon. To obtain higher refractive index films, silane (SiH_4) was also used in a mixed argon/oxygen plasma for depositing SiO_x films with x ranging from 0 to 2. This resulted in a larger variation of the film refractive index from 3.3 to 1.46. The typical deposition rate for high quality films was 1 to 2 Å/s for both silicon precursors. This could be increased by a factor of up to 10 by

increasing the TDAS flow rate, however, the resulting films were less dense and prone to oxidation.

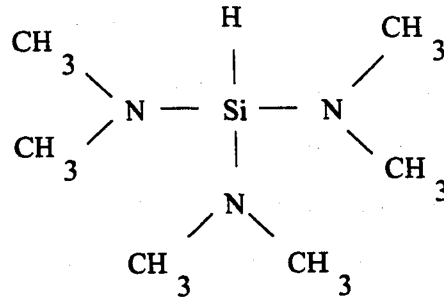

Figure 3.4: A schematic diagram of the TDAS molecule.

3.3.2 Properties of Silicon Oxynitride Formed using TDAS

It was found that high quality SiO_2 thin films could be fabricated in an oxygen plasma under most plasma conditions. When a nitrogen plasma was used to deposit SiN_x thin films using TDAS, however, the process generally produced films with poor adhesion. If no resistive substrate heating was used, the films were quite soft with very high etch rates in the buffered HF solution. In order to understand the deposition process more clearly, and to possibly improve the film properties, mixtures of argon and nitrogen with varying nitrogen partial pressure were used to deposit SiN_x films using TDAS as the silicon precursor. It is known that ion assisted deposition processes lead to improved film adhesion and density [33], and it was hoped that the ion bombardment provided by the argon component of the plasma would improve the deposited film properties. In addition, due to the presence of both silicon and nitrogen in the TDAS precursor, there is no nitrogen component required in the plasma, and silicon nitride films can be formed in a pure argon plasma.

The films were deposited at a substrate temperature of 150 °C (prior to the initiation of the plasma), and at a microwave power of 1000 W. It was found that

the hardness and adhesion of the films, as determined from simple scratch testing, improved significantly when a high argon content was used in the plasma. Figure 3.5 shows the measured FTIR spectra for films with nitrogen fractions ranging from 0 to 1, while Figure 3.6 shows the relative silicon, nitrogen, hydrogen and carbon concentrations determined from ERD measurements of the same set of films.

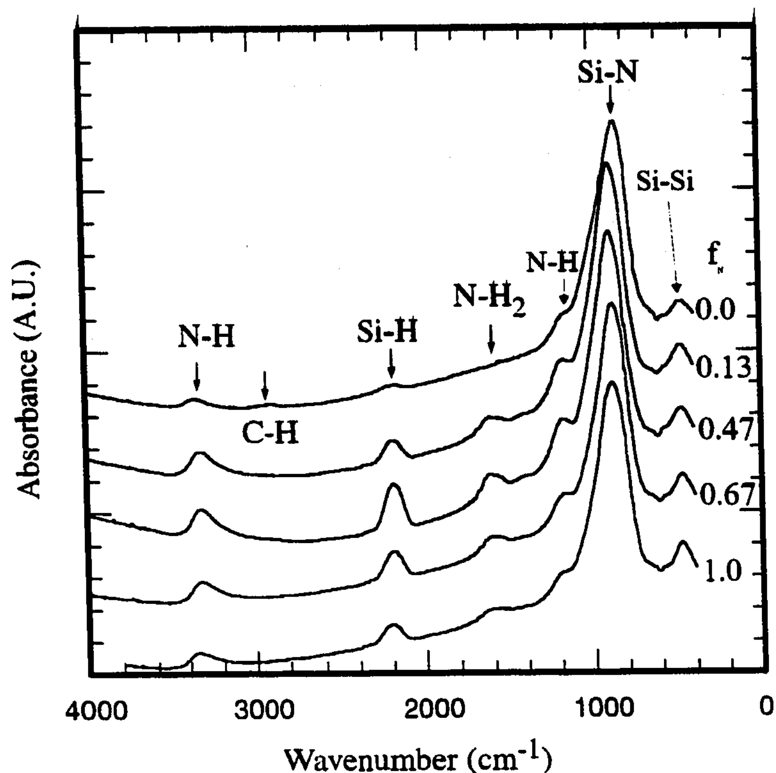

Figure 3.5: The effect of varying the nitrogen partial pressure on the measured FTIR spectra of SiN_x thin films.

The films contained less than 1% oxygen, and a small amount of argon which decreased as the argon content in the plasma decreased. The fraction of nitrogen (f_N) is defined as the ratio of the partial pressure of nitrogen to the total pressure. From the FTIR spectra it was observed that the amount of C-H bonding is highest in the films from an argon plasma, while the overall amount of bonded hydrogen, particularly

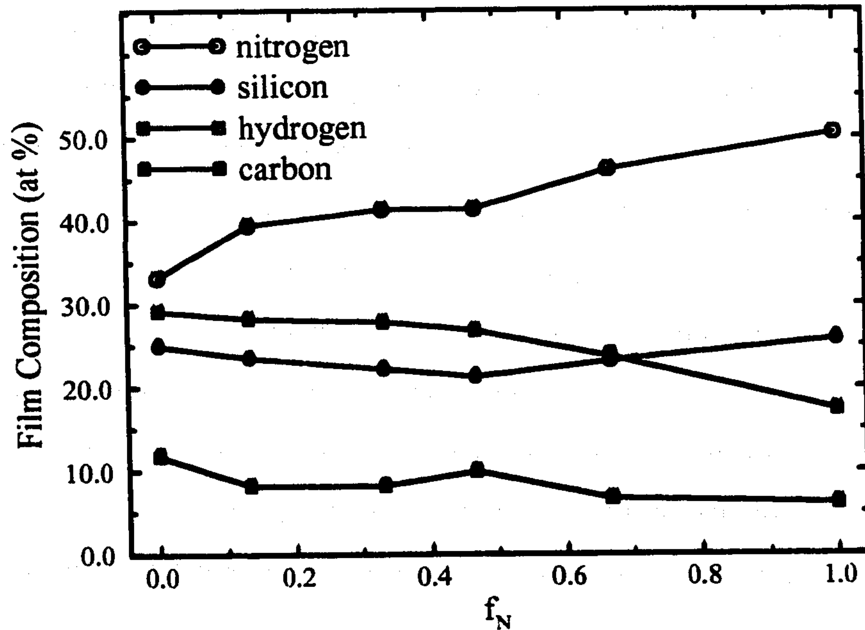

Figure 3.6: The effect of varying the nitrogen partial pressure on the measured composition of SiN_x thin films.

from Si-H and $N\text{-}H_2$ bonding, seems to be highest for $f_N = 0.47$ and is reduced as f_N approaches 0 or 1. From the ERD measurements the amount of hydrogen decreases with f_N while the amount of nitrogen increases. In this measurement, the total hydrogen content is measured, rather than just the fraction of hydrogen which is bonded in the film. The amount of silicon is nearly constant, with a slight reduction as f_N approaches 0.5, and the amount of carbon decreases as f_N increases.

Figure 3.7 shows the measured etch rate in BHF for the same set of films. In the pure argon plasma, the etch rate was only 0.5 Å/min with no observation of pinholes in films deposited on silicon substrates even after immersion in the etchant for 30 minutes. The observed etch rate was highest for plasmas with f_N near 0.5, consistent with the level of hydrogen bonding observed from the FTIR spectra. The

increased hydrogen bonding for mixed plasmas is an indication of a lack of stoichiometry, with hydrogen passivating dangling bonds in the film. The presence of network terminating N-H_2 bonds can have a large effect on the film etch rate since crosslinking of bonds in the film is significantly reduced [34]. Figure 3.7 also shows the position of the Si-N stretching peak, which is correlated with the level of bonded hydrogen, as well as the ratio of silicon to nitrogen in the film. For stoichiometric SiN_x films, the expected position of the Si-N stretching peak is 854 cm^{-1}. The presence of hydrogen as a nearest neighbor to a Si-N bond induces an increase in the ionic content of the bond, which results in a peak shift to higher wavenumbers [35]. For nitrogen rich films, an increase in the number of nearest neighbor nitrogen atoms again shifts the position of the Si-N related peak to higher wavenumbers. The behavior of the peak shift can then be explained as a combination of the increased level of hydrogen in the films for $f_N \approx 0.5$, and the steady increase of the nitrogen content in the film with f_N. From the ERD measurements it is observed that films formed in a pure argon plasma actually contain the highest amount of hydrogen and carbon, although from the etch rate behaviour and FTIR spectrum the films appear to be reasonably pure silicon nitride. The oscillator strength for the C-H stretch absorption is quite low, and so C-H bonds account for most of the excess hydrogen. Also, the ratio of silicon to nitrogen is stoichiometric (3/4) for these films, and so the appearance of the Si-N stretch peak at the expected wavenumber for silicon nitride is reasonable. The chemical inertness of the films seems to come from the longer range bonding structure. There must be a strong crosslinking of local bonding units through Si-C and C-C bonds. Some evidence for this is seen in the broader shape of the Si-N absorption peak for the films from a plasma with f_N=0, when compared with films from higher f_N plasmas.

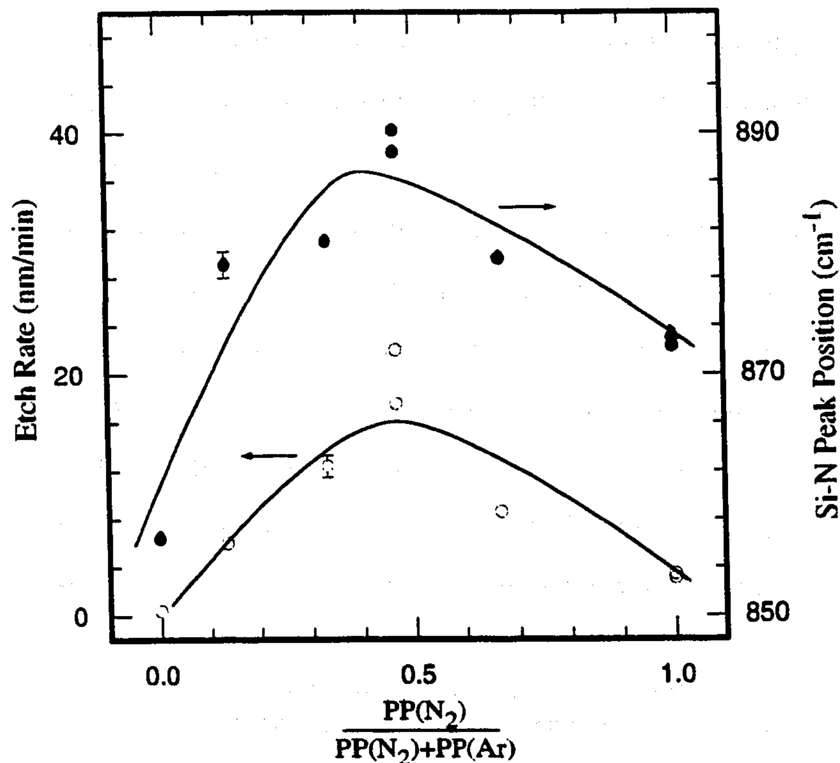

Figure 3.7: The effect of varying the nitrogen partial pressure on the measured etch rate and position of the Si-N stretching peak of SiN_x thin films.

As mentioned earlier, for the fabrication of interference filters, silicon oxynitride and silicon oxide films were used. The main parameter used to vary the film index of refraction was the partial pressure of oxygen in the plasma. Figure 3.8 shows the effect of varying the partial pressure of oxygen in a nitrogen and argon plasma on the film index of refraction when TDAS was used as the silicon precursor. For the argon plasma, the film is almost completely oxidized even with only 10 % O_2 in the plasma. If a nitrogen plasma is used instead of an argon plasma, the sensitivity to oxygen is significantly lower.

Similar behavior in the index of refraction was observed when SiH_4 was used as the silicon precursor. Figure 3.9 shows a plot of the refractive index of SiO_x films

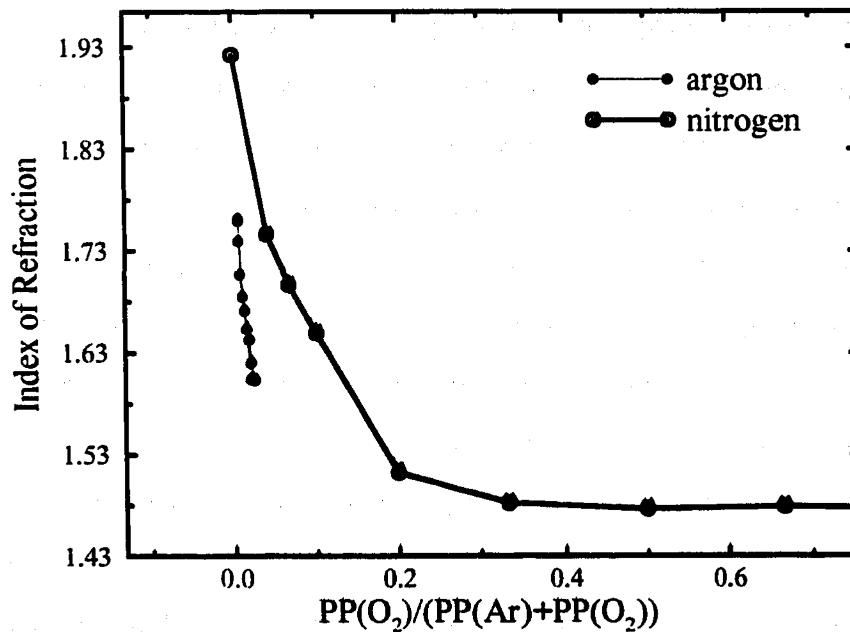

Figure 3.8: The effect of varying the fraction of oxygen in an argon and nitrogen plasma on the film index of refraction.

deposited using SiH_4 as a function of the ratio of the flow rate of oxygen to silane in the plasma.

The mass flow controllers used to deliver the gases to the chamber are accurate to within 0.2 sccm from run to run, and can control the flow rate to within 0.1 sccm of the set point value. Typical flow rates to obtain 2 mTorr pressure in the chamber are approximately 15 to 20 sccm. To obtain good control over the index of refraction of the film, the true O_2 flow must be accurately set between 0 and 2 sccm. In order to improve the control over the delivered O_2 flow, a mixture of 10 % O_2/90 % Ar was used, in addition to a flow controller with a one fifth the flow range of the original controller. With these modifications, the fraction of O_2 in the plasma could be controlled to within 0.002 sccm. This leads, in principle, to a control over the

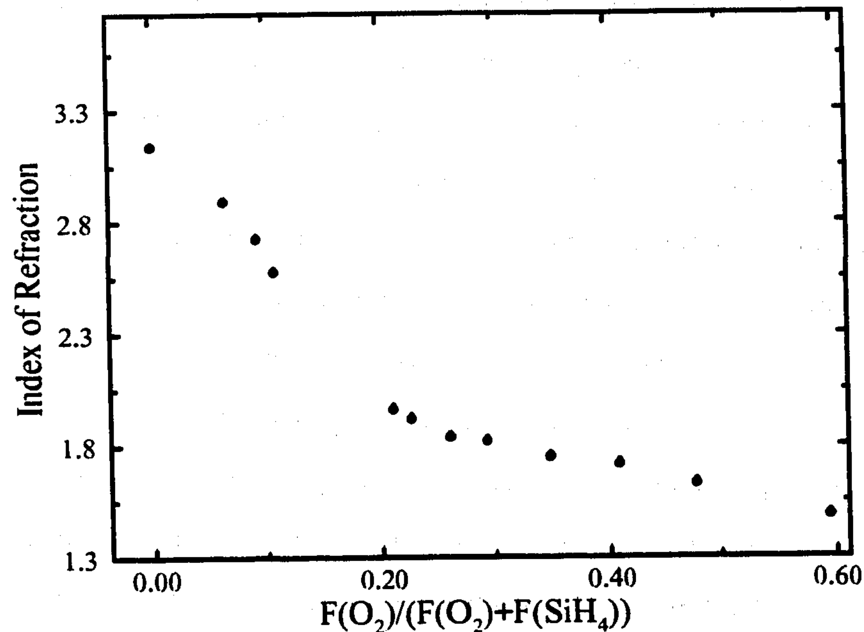

Figure 3.9: The effect of varying the flow ratio of oxygen to SiH_4 in an argon plasma on the film index of refraction.

refractive index to within 0.002 for SiH_4 and less than 0.001 for TDAS, using the range of refractive indices available for each silicon precursor. Other effects, such as variations in the conditions of the chamber walls, or vacuum leaks, should then be the issues which affect the control of the refractive index.

Because of the sensitivity of the films to oxygen, it was found that great care must be taken to avoid contamination in both the vacuum and the gas delivery systems. Water vapour entrained in the gas delivery tubing, or vacuum leaks with a partial pressure higher than 1×10^{-7} Torr in the chamber resulted in a lowering of the index of refraction obtained for SiN_x by up to 0.1. This sensitivity is due to the strength of the Si-O bond relative to Si-N and Si-C bonds.

AFM measurements indicated that the films had an extremely smooth mor-

phology. The RMS roughness of a 1000 Å thick film of SiO_2 deposited using TDAS on silicon was measured to be less than 1 Å, on InP, the roughness increased to 2.6 Å [36]. The surface roughness increases for thicker structures, however, even for a 17 layer HR coating on silicon with a thickness of 2.2 μm, the roughness was less than 1 nm. This compares with typical values obtained using ion assisted evaporation techniques of 2 to 3 Å for single layer films approximately 0.25 μm thick [37]. The figures quoted here give an indication that the films are smooth with respect to light scattering, however, the topic of surface morphology is quite complex and these numbers are given for comparison only.

SEM measurements of the film surface on silicon substrates were typically featureless, indicating a high quality surface after deposition. Greater care must be taken for depositions performed on GaAs or InP substrates, since plasma heating can produce damage in these materials. By lowering the microwave power to 800 W high quality coatings could be obtained on GaAs. Powers as low as 500 W were necessary to obtain high quality coatings on InP.

3.4 Ellipsometric Monitoring

A Rudolph Research i1000 rotating compensator ellipsometer operating at a wavelength of 633 nm was used for thickness control and for the monitoring of the film index of refraction. The details of the operation and capabilities of the original unit are outlined in reference [30].

In order to increase the flexibility of the ellipsometer, customized control software was written to allow more complex numerical processing of the basic ellipsometer data. Three important sources of error in determining the actual film index and thickness were isolated, i. e., imperfections in the compensator element

of the ellipsometer, imperfections in the vacuum windows through which the probing beam of the ellipsometer passed, and variations in the index of refraction of the substrate with substrate temperature changes. A recalibration of the ellipsometer, incorporating corrections for these errors, resulted in significant improvements in the measurement accuracy.

3.4.1 The Measurement Process

Figure 3.10 shows a schematic diagram of the rotating compensator ellipsometer. The ellipsometer consists of the polarizer, set at an azimuth of 45 °, the rotating

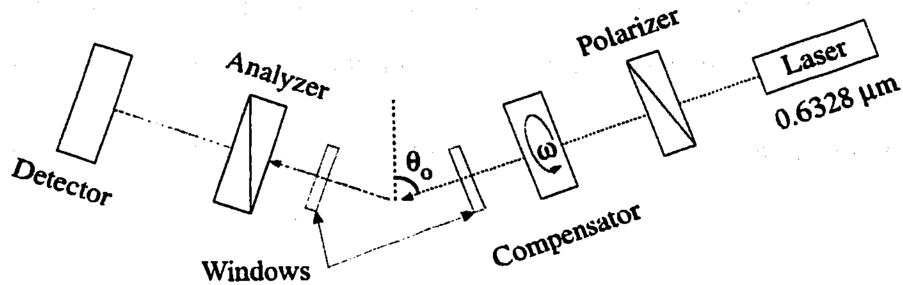

Figure 3.10: Schematic diagram of the rotating compensator ellipsometer.

compensator, the input vacuum window, the sample under investigation, the output vacuum window, and finally the analyzer, again set at an azimuth of 45 °.

The conversion of the basic ellipsometer data into a measured value of a film parameter of interest is a complex process which can be broken down into three steps. If the compensator spins such that the fast axis azimuth of the compensator crystal is at an angle C relative to the plane of incidence of the sample, the intensity seen by the detector varies as

$$I(C) = A_0 + A_2 \cos 2C + B_2 \sin 2C + A_4 \cos 4C + B_4 \sin 4C \quad (3.1)$$

The first step is the calculation of the Fourier coefficients, A_i, B_i, from a measurement of the intensity as a function of angle. The second step is to use these 4 coefficients,

normalized by A_0, to determine the values of Δ, and ψ, the two ellipsometric angles. If ρ_p is the complex reflection coefficient for p polarized light, and ρ_s is the same for s polarized light, the values of Δ and ψ are defined as

$$\begin{aligned} \Delta &= \arg \rho_p/\rho_s \\ \psi &= |\rho_p/\rho_s|. \end{aligned} \quad (3.2)$$

Systematic errors can occur in the calculation of Δ and ψ due to imperfections in the optical components used in the ellipsometer, or errors in the azimuth settings of the components. The third step is the inversion of the measured values of Δ and ψ using a model of the film structure similar to that shown in Figure 2.1. Here, errors in the estimates for the assumed model parameters produce errors in the values measured for the parameters to be determined. The ellipsometric data was used in several different ways, depending on the type of film structure which was deposited. The index of refraction of a bare substrate, the thickness of a film with a predetermined index of refraction, both the thickness and index of a single film on a substrate, or the thickness and index of a layer deposited on an arbitrary stack of known optical admittance could be calculated, depending on the inversion algorithm chosen.

The accurate calibration of the ellipsometer is very important if accurate measurements of the film optical properties are to be made. Three reference wafers of known refractive index and thickness were measured with the present ellipsometer. From this, three sets of Δ and ψ were obtained for a total of six parameters. These six parameters were used to calculate the actual ellipsometer angle of incidence and the window optical properties, defined by Δ_w and ψ_w. A numerical process varied the three fitted parameters to match the measured values of Δ and ψ to the theoretically calculated values. The accuracy of the fit was indicated by a normalized error term calculated from the squared differences between the predicted and the model Δ and

ψ.

3.4.2 Compensator Imperfections

The Fourier coefficients of the intensity variation (A_i, B_i) are functions of the polarizer and analyzer azimuth. as well as the Jones matrix of the compensator and the sample. Hauge et al [38] describe the dependence of the Fourier coefficients on the Jones matrices of the optical elements and sample, including the effect of an imperfection in the compensator. The Jones matrix of an imperfect compensator can be written as

$$\begin{bmatrix} 1 & 0 \\ 0 & \rho_c \end{bmatrix}, \tag{3.3}$$

where

$$\begin{aligned} \rho_c &= \tan\psi_c \exp^{(-i\Delta_c)} \\ \psi_c &\cong \pi/4 \\ \Delta_c &\cong \pi/2. \end{aligned}$$

The imperfection plate of the compensator can be measured quite simply by measuring the variation of the intensity with compensator angle in a direct polarizer-compensator-analyzer setup, where the sample is removed. This procedure was performed. and resulted in values of 90.35 ± 0.01 and 45.134 ± 0.005 for Δ_c and ψ_c, respectively for the compensator used in these experiments. The effect of this on the calculation of the film refractive index and thickness during the deposition of a typical film is seen in Figure 3.11. The error is much more significant for a very thin film, where the value of ψ is near zero. The error in the ellipsometric angles produces a large error in the measured index for thin films. For films less than approximately 500 $\AA$ thick, the dependence of the film index on ψ and Δ is very weak, and so any

errors in these angles, whether they are instrumental errors, or due to errors in the estimates of the film model parameters result in large errors in the measured film refractive index.

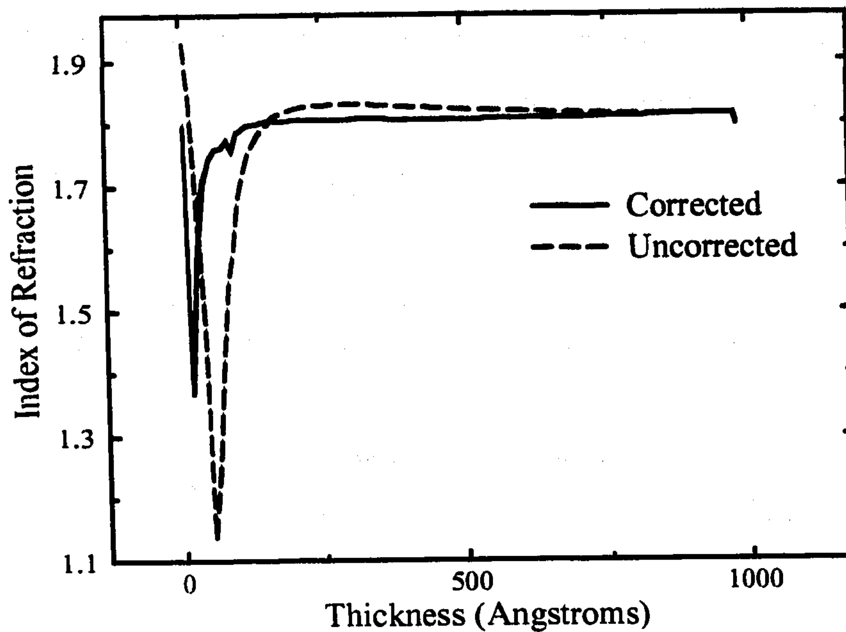

Figure 3.11: The effect of incorporating the compensator imperfections on the measured index of refraction of a deposited film.

3.4.3 Window Imperfections

The optical beam must pass through two vacuum windows in order to access the sample. In our system the windows are made of fused quartz brazed in a 1.33 inch conflat flange. The windows should have no effect on the state of polarization of the beam, however, they have a residual Δ and ψ value due to stresses from the brazing process, as well as stress induced by the tightening of the vacuum gasket. It was determined that the optical properties of several different windows were approx-

imately equal. The windows behave like a compensator with a very small relative phase. Typical values of Δ_w and ψ_w were 1.5 ° and 45.5 °, respectively. As mentioned above, provisions were made in the calibration routine to evaluate the properties of the windows and to subsequently eliminate the window effect, however, it was more desirable to reduce the window imperfections. It was found that the residual ellipticity induced in linearly polarized light propagating through the windows was reduced to approximately 10 % of the original value by mounting a second window in the beam and rotating it such that the ordinary optical axis of one window was parallel to the extraordinary axis of the second window.

Prior to correcting for the compensator and window imperfections a typical fit error term, calculated as outlined in section 3.4.1, was approximately 1.1. After these corrections, the fit error was reduced to 0.23. Table 3.1 lists the measured and actual thickness and index of several thermally oxidized silicon reference samples to give an indication of the typical accuracy of the ellipsometer measurement for this fit error.

n_{ref} ±0.002	d_{ref} Å(±3Å)	n_{meas}	d_{meas} Å	nd error (%)
1.462	426	1.466	429	1.1
1.462	445	1.456	458	2.5
1.462	1102	1.464	1106	0.5
1.462	2229	1.465	2223	0.06
1.462	2270	1.462	2277	0.3
2.002	934	2.008	933	0.2

Table 3.1: A comparison of the measured thicknesses and optical index of reference thin films with the actual values.

Again, the largest relative errors are observed for thinner films, however in all cases except one, the error in the optical thickness was less than 10 Å, while the error in the index of refraction was always less than 0.5%.

3.4.4 Substrate Index Errors

The most significant error affecting the accuracy of the film index and thickness calculation during a deposition was due to variations in the substrate index of refraction during a deposition. This index change results from temperature changes in the substrate during plasma exposure.

To incorporate this heating effect in the ellipsometer measurement, a measurement of both n and k for the substrate as a function of surface temperature was made as shown in Figure 3.12. A least squares fit to the temperature dependence gave the following functional forms for the dependence of n and k at 633 nm for a silicon substrate on the substrate surface temperature

$$\begin{aligned} n &= 7.23 \times 10^{-4}T + 3.838 \\ k &= 1.768 \times 10^{-7}T^2 + 1.256 \times 10^{-4}T + 7.37 \times 10^{-3}. \end{aligned} \tag{3.4}$$

Temperature measurements made during a deposition were used to adjust the optical properties of the substrate which were used in the inversion algorithm to convert Δ and ψ values to film index and thickness. Figure 3.13 shows a plot of the index versus thickness, determined with and without substrate temperature correction, for a single layer of silicon nitride deposited using TDAS in a pure argon plasma. Again, the largest effect occurs for thinner films, where the inversion calculation is much more sensitive to errors in both Δ and ψ.

3.5 Coating of Laser Facets

A spring loaded fixture was fabricated from stainless steel to mount laser bars to be coated. The laser bars were mounted between the cleaved edges of two silicon wafers. The arrangement is shown in figure 3.14. The silicon wafers act to clamp the laser

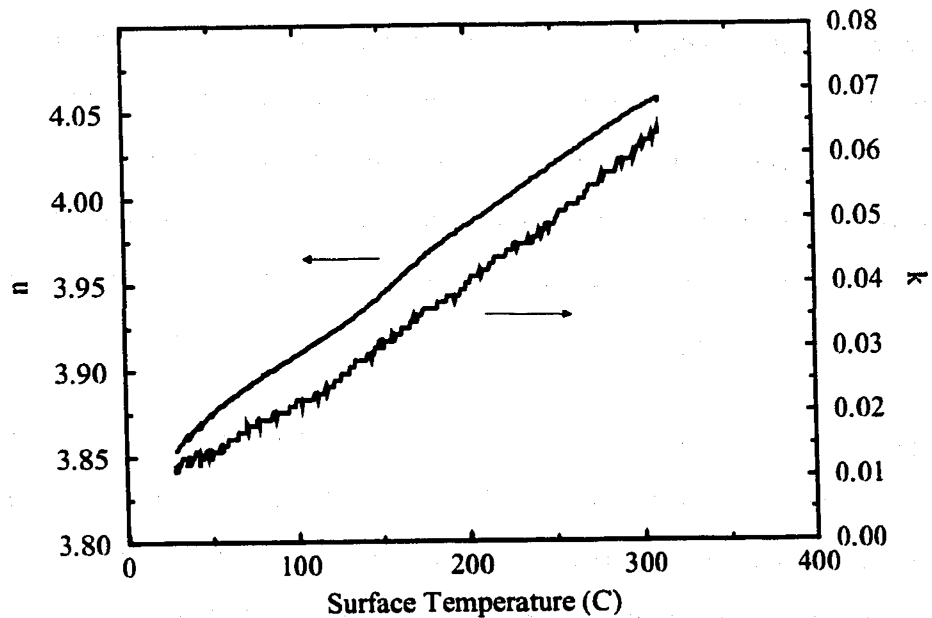

Figure 3.12: Measured substrate refractive index versus substrate temperature for a silicon substrate at 633 nm.

bars to be coated on edge and are also used for optical monitoring by the ellipsometer. The surface thermocouple is placed on the sample, as indicated in the figure. The thickness of the silicon wafers must be slightly less than the length of the lasers to be coated, which ranged from 300 μm up to 750 μm. This is necessary so that the metal contacts on the top and bottom of the laser do not become coated by the dielectric.

Particular care had to be taken to ensure that a light pressure held the laser bars in place, even during the temperature cycling which occurs during the plasma deposition procedure. A balance between a holding pressure high enough to keep the laser bars stably mounted, yet low enough to avoid cleaving or otherwise damaging the thin bars must be maintained. In order to coat both facets of a laser the bars were removed and rotated after the first facet coating and the silicon wafers were replaced.

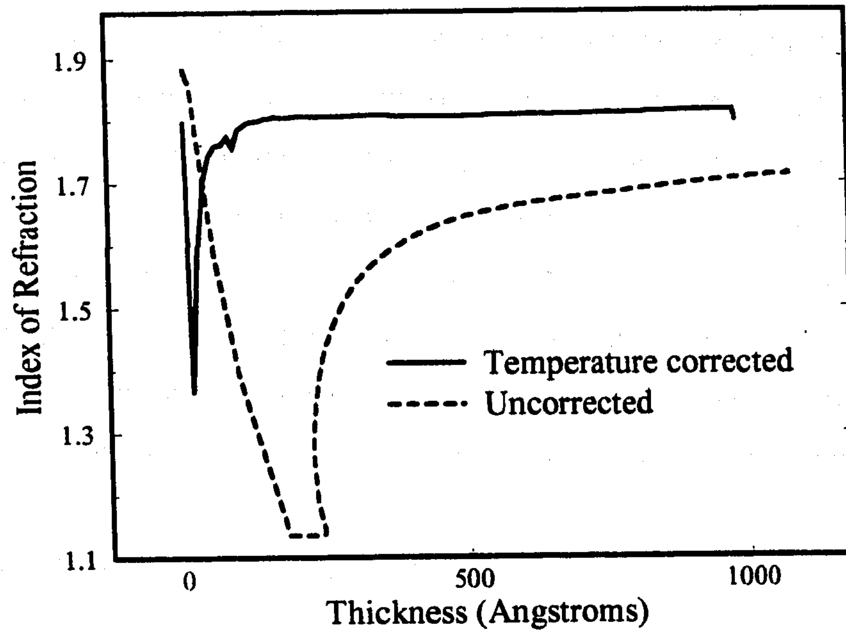

Figure 3.13: The effect of incorporating substrate temperature changes on the measured film refractive index versus thickness for a typical deposition.

3.6 Control Algorithms

The set points of the flow rates of the plasma gases, argon, oxygen and nitrogen, were automated using a simple A/D convertor. In principle, one could then input a desired set of film thicknesses and indices as the setpoint for the deposition process, and then use the difference between the measured film properties and the setpoints as an error term in a feedback control loop which would adjust the relative flows of the gases to obtain the desired film characteristics. This type of control was not successful due to the difficulty of accurately determining the film index of refraction for thin films. For multilayer structures, this problem is compounded by the feed forward nature of the inversion algorithm, which calculates the index of refraction of the top layer based

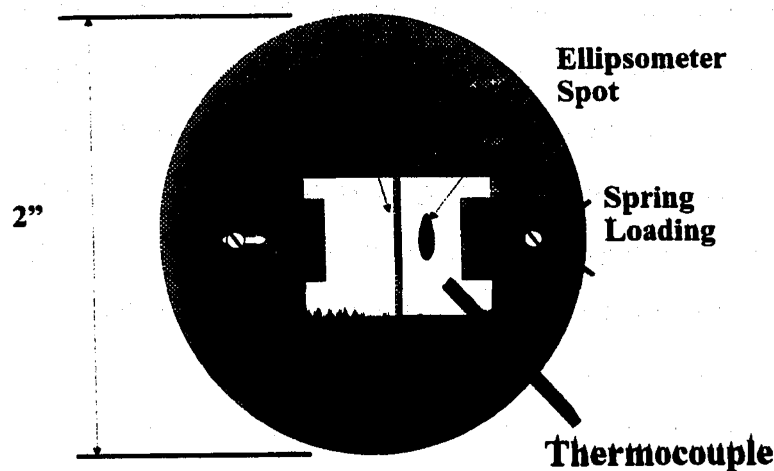

Figure 3.14: A schematic diagram of the fixture used to mount laser bars for optical coating.

on previously measured refractive indices [39]. This instability problem has been addressed recently. By using a measurement of the rate of change of Δ and ψ with thickness, a measurement of the surface index independent of previously accumulated layers may be possible in certain cases [39, 40, 41].

A more successful control algorithm uses the inversion routine which assumes a fixed index of refraction for a given layer, and measures only the thickness of the present layer. The endpoint of a layer is determined from the optical thickness measured by the ellipsometer. For this method, a calibration of the index as a function of the plasma gas flows is required. Data from Figure 3.8 was used to calibrate the index as a function of oxygen partial pressure in an argon plasma. The result is shown in Figure 3.15. Errors in the assumed refractive index do not result in thickness errors, since the ellipsometer is measuring the optical thickness rather than physical thickness

of the deposited film.

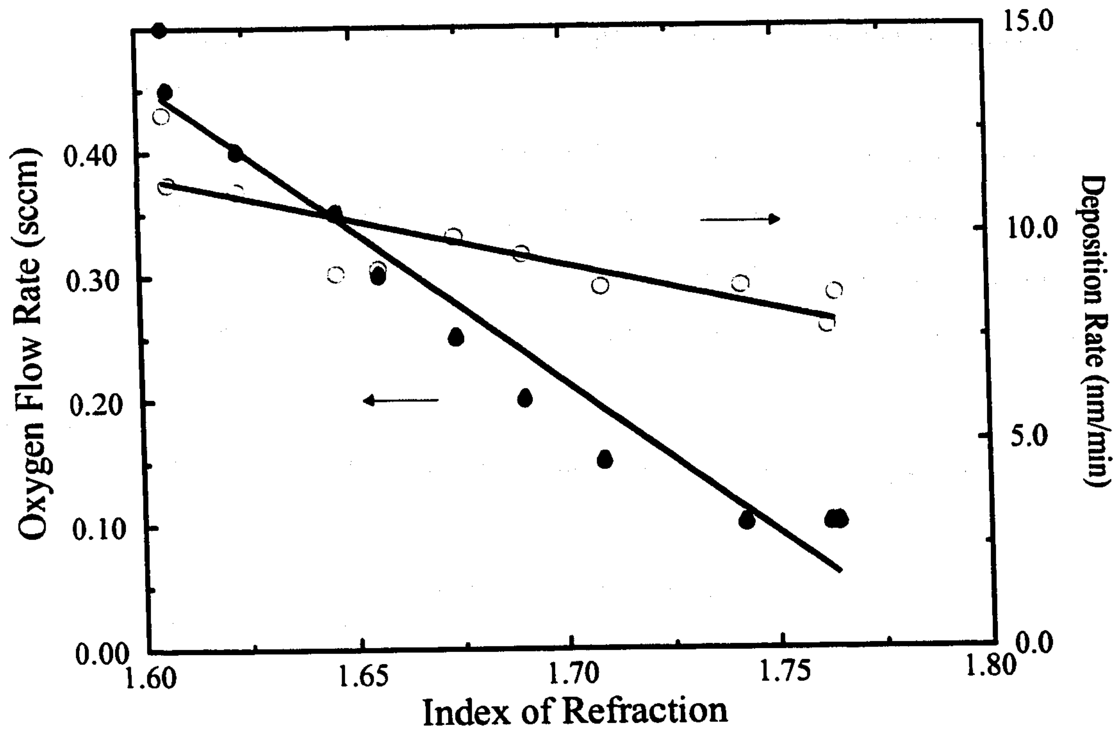

Figure 3.15: Calibration of the flow rate required for a given index of refraction and deposition rate.

This method was used to deposit optical interference filters containing up to 37 layers. Figure 3.16 shows a scanning electron micrograph of a filter consisting of alternating layers of high index ($n = 1.75$) and low index ($n = 1.6$) silicon oxynitride. There were two skipped layers in the normal periodic cycle from high to low index which are apparent in the SEM.

Figure 3.17 shows the measured deposition rate as a function of time for the same deposition. Note that initially the deposition rate is high and drops during the first few minutes. This is associated with the increase of the substrate temperature.

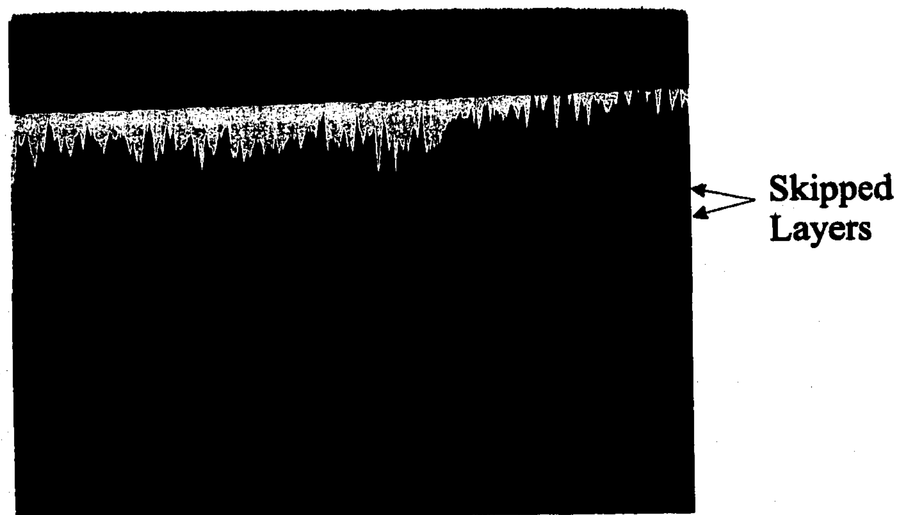

Figure 3.16: SEM of an optical filter consisting of 35 layers.

After this initial transient, the deposition rate seems to rise and fall as appropriate from the calibration, however, as the structure becomes thicker, a periodic increase in the deposition rate appears which does not seem to correlate with the gas ratio in the plasma.

3.7 Summary

In this chapter, the accuracy of the deposition control using in situ ellipsometry has been illustrated. Although a full feedback control system is not feasible for filters consisting of more than a few layers, the ellipsometer control is quite effective for one or two layers, and is very important for the fabrication of AR coatings. As well, the material properties of the films deposited by the ECR-PECVD system have been described. It is seen that the properties of films deposited under low temperature conditions are excellent.

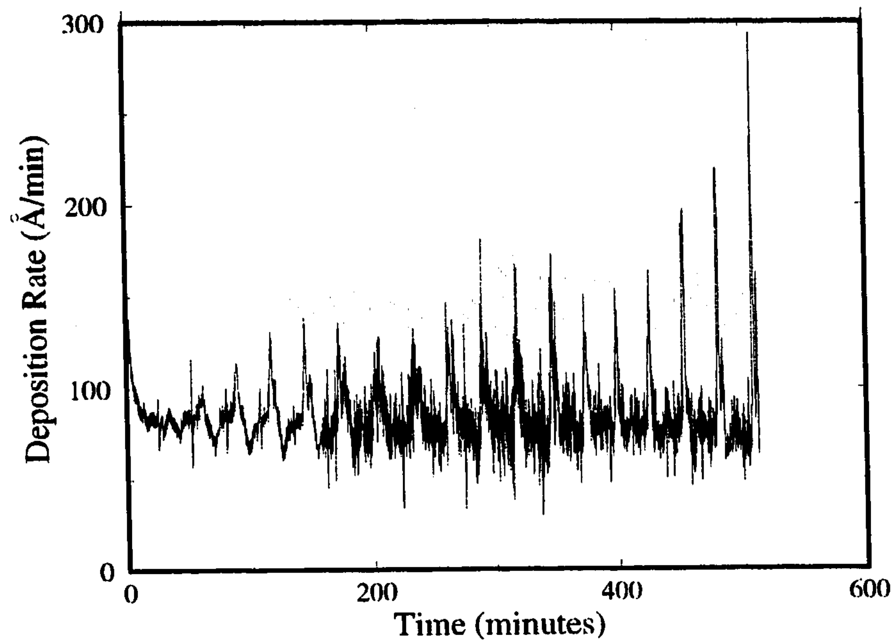

Figure 3.17: Deposition rate vs time for the filter shown above.

Chapter 4

Characterization of Interference Filter Properties

Filters based on the designs described in chapter 2 were fabricated in the ECR-PECVD system. In this chapter the properties of these filters, and the results of the application of these filters to laser facets will be described.

4.1 Experimental Details

The reflectance of multilayered structures was determined using a Perkin-Elmer, Lambda 9 spectrophotometer with a reflectance mount. The reflectance could be measured from a wavelength of 190 nm up to 3200 nm. Figure 4.1 shows the geometry used for the reflectance measurements. A gold film was applied to the surface of each prism used to redirect the optical beam. Before each filter measurement, a measurement of the reflectance of a silicon wafer was used to calibrate the system. The theoretical values of refractive index and extinction coefficient for the gold and silicon were obtained from reference [42]. The reflectance measurements are accurate to within 2%, while the minimum measureable reflectance is approximately 0.1%. To measure reflectances below this value, which was required for the characterization of AR coatings, a tunable external cavity laser was used (Model ECU-2001, Environ-

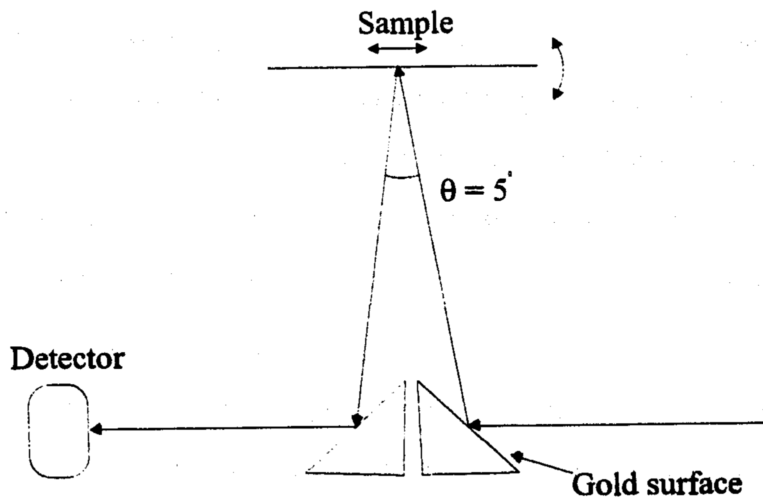

Figure 4.1: The mount used to measure the reflectance spectrum.

mental Optical Sensors Inc.). A laser module tunable over a wavelength range from 835 nm to 865 nm at constant output power was used to measure the reflectance of filters designed for minimum reflectance at 850 nm. The laser operates in a single longitudinal cavity mode, due to the high optical feedback provided by the external cavity, and as a result linewidths of less than 4 MHz are obtained. This is effectively monochromatic for the purpose of measuring the filter reflectance. Due to the high optical power obtained from the laser, the measurement of a reflectance of 10^{-4} with better than 1% precision is possible using a simple silicon photodetector. The reflectance is normalized to that of the substrate, for silicon substrates the reflectance was again calculated from reference [42].

For the most part, the lasers coated in this work were 300 μm stripe width, broad area lasers based on the AlGaAs/GaAs material system with a GaAs active region. The operating wavelength of the lasers was approximately 860 nm. InGaAsP/InP based lasers operating at wavelengths from 1.4 to 1.55 μm and aluminum free InGaP/GaAs 980 nm lasers were also coated. For the InP based lasers, a very

careful choice of the deposition parameters must be made in order to avoid degradation of the InP surface, resulting in poor adhesion of the film. The most important factor appears to be the microwave power used during the deposition, which must be lowered to 500 W. For the GaAs based lasers, no visible damage is observed on the laser facets, using a high power optical microscope, after the coatings were deposited using a 1000 W microwave power. For these lasers, the issue of plasma induced damage is described in more detail in chapter 5

For the AlGaAs lasers, testing was carried out using a 10 A current pulser. A pulse width of 200 ns was used at a repetition rate of 1 kHz. The laser was mounted on a copper heat sink, however, no active control of the laser chip temperature was used. A spring loaded contact was used to deliver the current to the laser. A large area contact was used to reduce the local current density which could overheat and locally melt the metallization layer on the laser. Typically lasers were tested with the junction side up. The light was collected using an integrating sphere, and the output from the sphere was directed to a silicon photodetector. A standard box car gating scheme was used to measure the average optical power associated with each current pulse. Using this apparatus, the light vs current (L-I) characteristic for the coated lasers was measured.

Both AR and HR facet coatings were applied to these lasers. The reflectance was determined from the relative power observed from the coated and uncoated facet of the same laser. The ratio of this power is given by

$$\frac{P^+}{P^-} = \left(\frac{R^-}{R^+}\right)^{1/2} \left(\frac{1-R^+}{1-R^-}\right), \tag{4.1}$$

where P^+ (P^-) is the power from facet + (−), and R^+ (R^-) is the facet reflectance as in Figure 2.11. Since the threshold current is the same for both facets, the differential quantum efficiency, or the slope above the threshold current can be used to determine

the reflectance at the coated facet.

4.2 AR and Wide Band HR Coatings

Both single layer and two layer AR coatings have been applied to wafers in order to characterize the accuracy of the ellipsometer measurements, and to determine the effectiveness of the coating. For the single layer coating, the reflectance measurements were made using the tunable laser, and so the coating was designed for a minimum reflectance at 850 nm. For the example described here, a SiO_x film was deposited using a mixture of argon, oxygen and silane (17.3 sccm Ar, 0.42 sccm O_2, 1.5 sccm SiH_4) at a microwave power of 1000 W on a silicon substrate. The refractive index of the substrate at this wavelength was $N_{sub} = 3.65+i0.005$ [42], the ideal index of refraction for a single layer AR coating should be 1.91. Figure 4.2 shows the measured reflectance of this coating, a minimum reflectance of 3×10^{-4} was obtained at 847 nm. The measured parameters for the film, obtained from the *in situ* ellipsometer were $n_{film} = 1.891$, $d_{film} = 1120$ Å, for a theoretical minimum at $\lambda = 4nd = 847$ nm.

There was a significant non-uniformity in both the coating thickness and index of refraction across the wafer. As a result, the minimum reflectance was a function of the position on the wafer at which the measurement was made. Ellipsometric measurements performed on the coating after the deposition indicated that the index varied by approximately 0.03 across the wafer, while the thickness varied by 100 Å. Measurements made at the same location as the *in situ* measurement were in agreement, however the minimum reflectance did not occur at this position since the refractive index is slightly low. The minimum value of the reflectance occured at a position on the wafer where the index of refraction was observed to be closest to 1.91. The laser spot size for the *in situ* ellipsometer was approximately 6 mm long

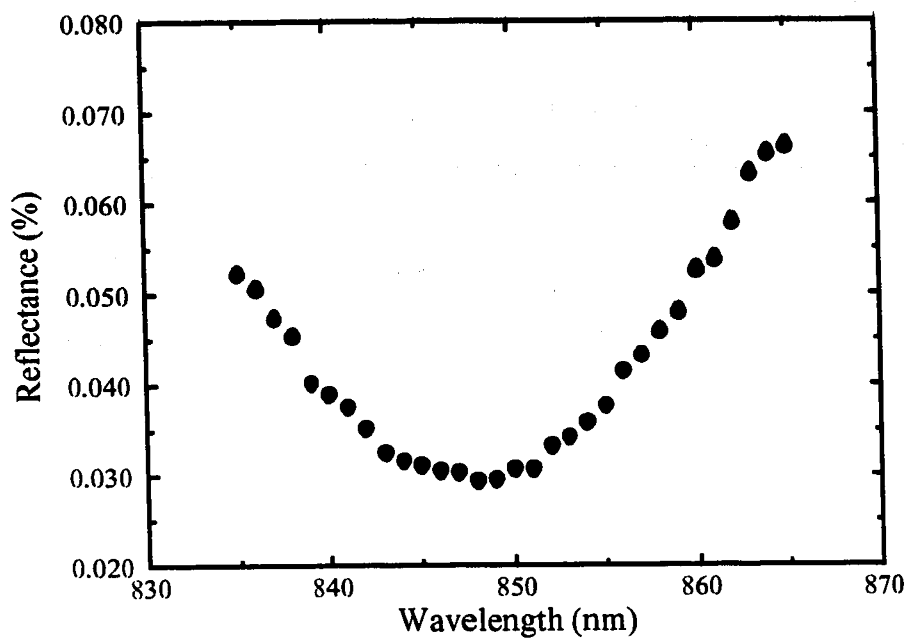

Figure 4.2: The measured reflectance for a single layer AR coating.

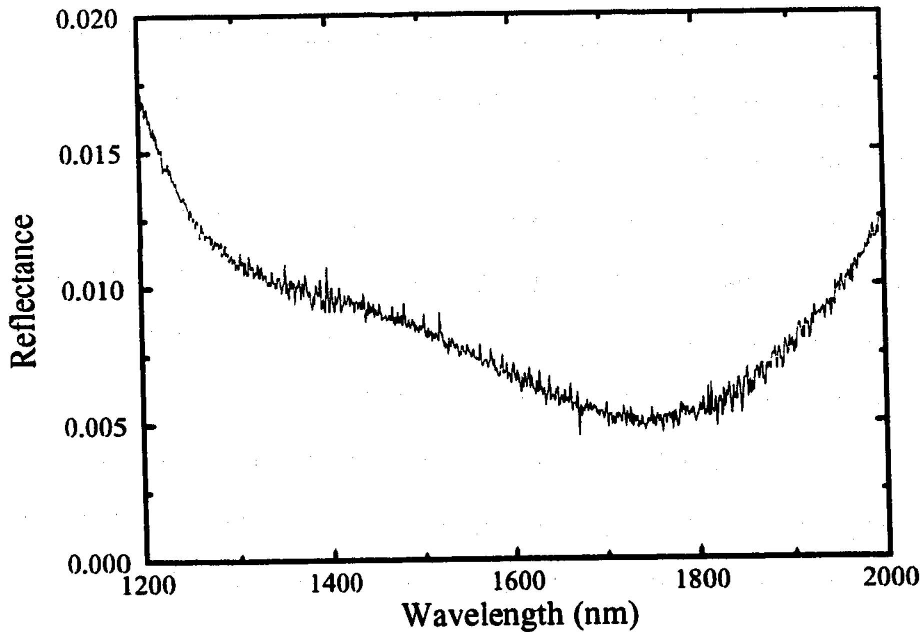

Figure 4.3: The measured reflectance for a two layer AR coating designed for 1500 nm on silicon.

and 3 mm wide, while the silicon sample is 3 cm × 2 cm. As mentioned in chapter 4, the source of the non-uniformity in the film refractive index and thickness is mainly due to the non-uniform distribution of the SiH_4 in the plasma.

An example of the reflectance measured from a two layer coating is shown in Figure 4.3. In this case, the reflectance minimum was designed to occur at 1500 nm. The dispersion in the silicon substrate refractive index is significantly lower for these wavelengths, varying from 3.488 at 1.4 μm to 3.47 at 1.6 μm. In this case, the measurement of the reflectance was performed using the spectrophotometer. Significant errors in the absolute reflectance minimum could occur due to the large spot size of the illuminating beam, as well as the spectral width of the monochromator, which was 2 nm in this case. Even with these error contributions, which would tend to in-

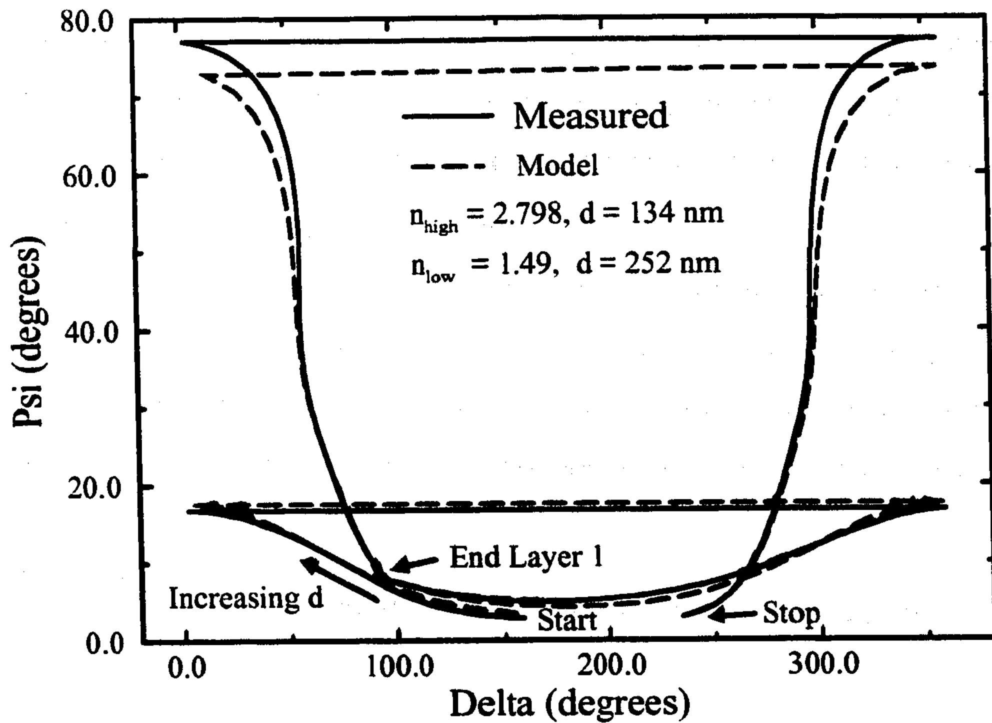

Figure 4.4: The measured and model Δ and Ψ trajectory for the 2 layer AR coating of Figure 4.3.

crease the value of the minimum reflectance obtained, the reflectance is below 1% for a large wavelength range, from 1400 nm to 1800 nm. Figure 4.4 shows the measured and predicted ellipsometer measurements of Δ and Ψ for this coating. There is very good agreement here, however, it should be noted that the dispersion in the refractive index of the film has not been taken into account.

AR coatings fabricated using TDAS from an argon plasma have been applied to the AlGaAs broad area lasers. After coating one of the facets, the threshold current of the laser increased from 2.8 A to 4.5 A. The measured reflectance, based on the ratio of the optical power from the coated and uncoated facet, was approximately

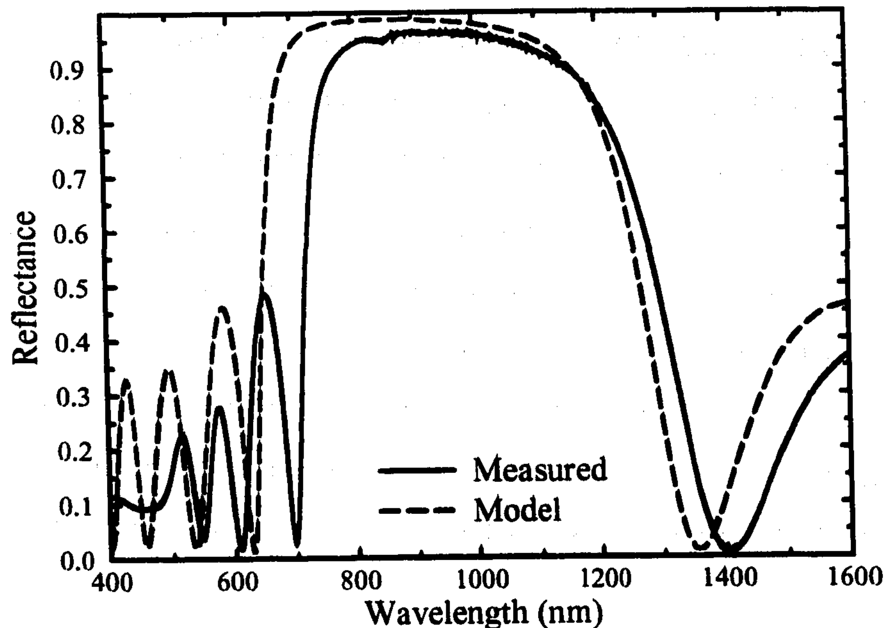

Figure 4.5: Measured and model reflectance for a 7 layer HR filter using SiH_4.

0.1%.

For the HR coatings, there is a significant improvement in the performance of the filters when using SiH_4 rather than TDAS, due to the wider available index range. Figure 4.5 shows the measured and model reflectance obtained from a 7 layer quarter wave stack of a-Si/SiO_2 (n_{high} = 3.3, n_{low} = 1.5). Note that dispersion in the refractive indices of both the substrate and the film layers has not been taken into account in the model reflectance calculation.

In order to obtain reasonably high reflectances using TDAS, many more layers are required in the quarter wave stack. Figure 4.6 shows the measured and model reflectance obtained from a 17 layer quarter wave stack of SiN_x/SiO_2 (n_{high} = 1.8, n_{low} = 1.5). In this case the filter was also applied to a laser bar, Figure 4.7 shows

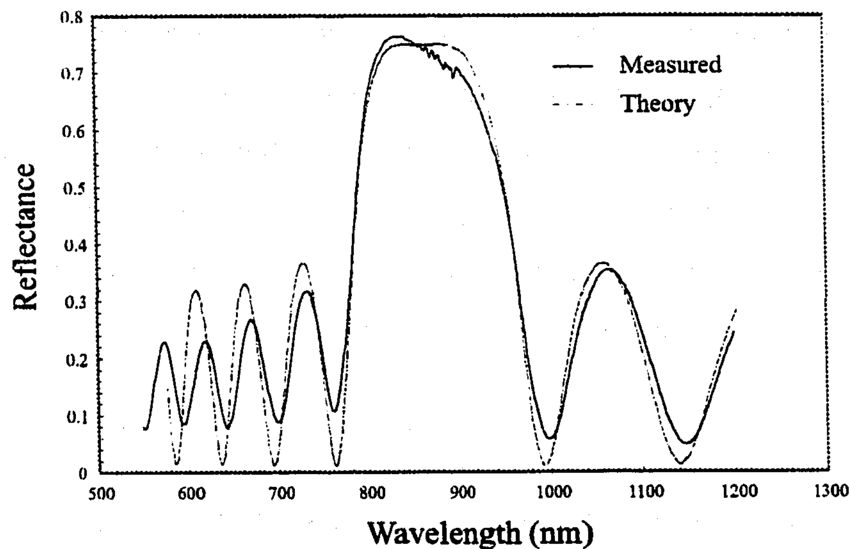

Figure 4.6: Measured and model reflectance for a 17 layer quarter wave stack using TDAS.

the L-I characteristic obtained from the coated and uncoated facet of the laser. The threshold current after coating was reduced from 2.8 A to 1 A. The reflectance obtained from the relative power out of each facet was plotted as a function of the chip position on the bar in order to indicate the reflectance uniformity over the length of the bar. Figure 4.8 shows the measured threshold current and modal reflectivity obtained and indicates that the reflectance varies by less than 4% across the bar.

4.3 Narrow Band Filters

In this section, the measured performance of narrow band high reflection coatings will be described. Two separate design types were used, quarter wave optical coatings, with a small index separation, ($n_{high} = 1.75$, $n_{low} = 1.6$), and rugate filters. The main advantage of an inhomogeneous filter is a reduced level of stress due to the lack of discrete interfaces, and as a result, the filters should have improved stability and adhesion when compared to quarter wave stack designs. Although it was possible

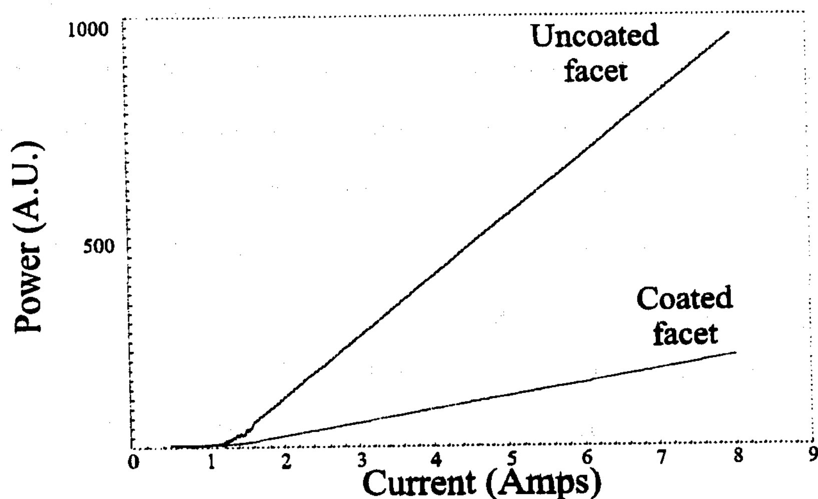

Figure 4.7: The measured L-I characteristic for both facets of a HR coated laser.

to fabricate the inhomogeneous structures, we found that these filters were prone to cracking and poor adhesion when the number of periods was increased to more than 15. Figure 4.9 shows a SEM image of a 10 period inhomogeneous filter with a thickness of approximately 5 μm. The film was deposited on silicon, however at this thickness there was no evidence of cracking or poor adhesion associated with a large build up of stress in the material.

The measured reflectance of two separate narrow band coatings designed for 860 nm and 965 nm are shown in Figure 4.10. The measured wavelength at which the peak reflectance occurs is indicated in the figure, as is the value of the reflectance where the width of the reflectance peak is approximately 40 nm. Considering the discussion of section 2.2.1, the performance of these filters on a laser facet could be significantly different, however it is shown that narrow band filters can be fabricated by this process. The number of periods for both cases was 37, and the total thickness was approximately 5 μm.

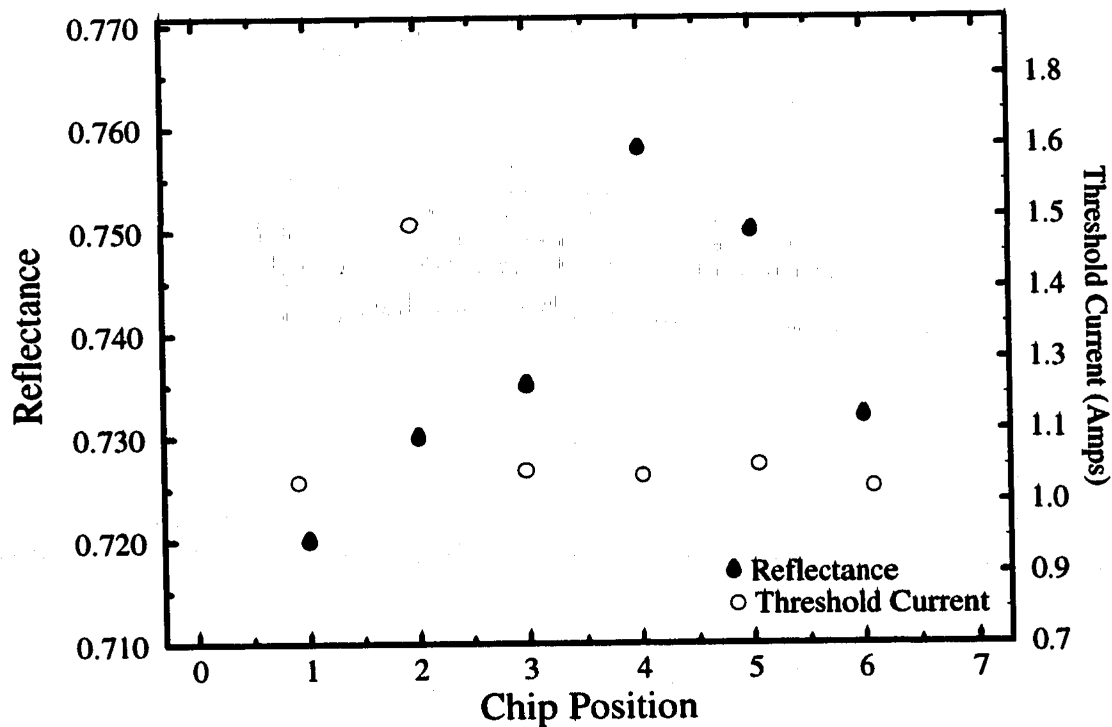

Figure 4.8: The measured model reflectivity and threshold current versus chip position on the coated laser bar.

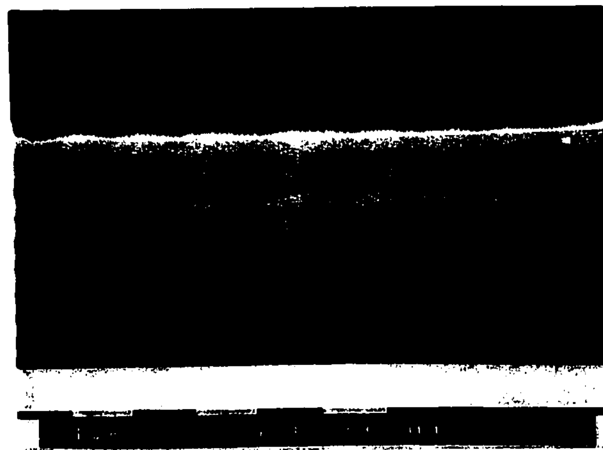

Figure 4.9: Back-scattered electron image of a 10 period rugate filter.

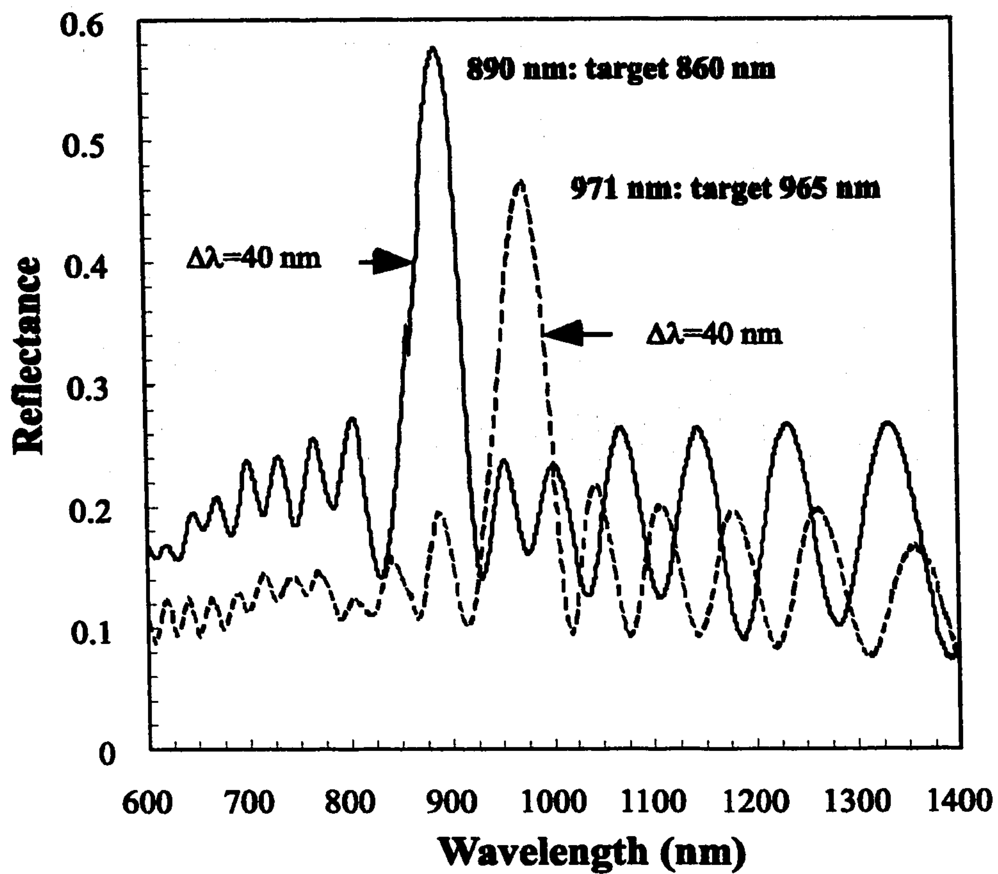

Figure 4.10: The measured reflectances of narrow band filters designed for 860 nm and 965 nm.

4.4 Summary

Several examples of thin film filters fabricated using the deposition process described in chapter 3 have been discussed. Both single layer, and double layer AR coating designs have been implemented, as well as wide band and narrow band high reflectance filters. It has also been shown that filters which could be used to affect the spectral output of a semiconductor diode laser can be deposited.

Chapter 5

Facet Coatings for High Power Lasers

It has been shown that the ECR-PECVD process can be used to fabricate complicated multilayer structures from silicon based dielectric materials. An additional feature of this process is the low damage induced in the substrate during the deposition process, allowing the deposition of high quality films on sensitive materials. Obtaining high surface quality on semiconductor laser facets is critically important for the reliable operation of lasers at high output powers [43, 44, 45, 46]. The level of imperfections present in the bulk of the laser structure has been reduced to the point where the main failure mode, particularly for lasers based on the the AlGaAs/GaAs material system, is catastrophical optical mirror damage (COMD) at the laser facet due to surface recombination centers. Under high output power operating conditions, non-radiative recombination through these surface states results in an increase of the facet temperature, which increases the rate of production of new surface states. This feed-back loop results in a sharp drop in the output power of the laser at some critical power level. Investigations of facets which have failed through this process indicate a thermal breakdown in the material with the liberation of As atoms and an increased Ga content at the surface [47].

It was found that a dramatic improvement in the surface quality of GaAs

could be obtained if the material was immersed in aqueous solutions of sulphur containing compounds such as $(NH_4)_2S$ and Na_2S [48, 49]. This discovery initiated a number of investigations to determine the origin of the passivation effect, and to evaluate its impact on various technologies. Obviously, such a treatment could have a significant influence on the optical power at which COMD occurs in AlGaAs/GaAs based semiconductor lasers. Unfortunately, surfaces passivated by sulphur are not stable, particularly under illumination or in humid environments, and some form of encapsulation is required. The present process is particularly appropriate for this application, due to the chemically inert nature of the SiN_x films deposited using TDAS, and the minimal process induced substrate damage.

In this chapter the present understanding of the AlGaAs surface, the effect of sulphur based passivations on this surface, and the encapsulation of these passivation treatments is reviewed. A discussion of the degradation in the output characteristics of SDL's is also given, with special attention focused on the properties of the laser facet during high power operation. The present research project was a collaborative effort divided between three groups, McMaster University, the University of Toronto, and EG&G Optoelectronics Canada. Commercial high power broad area AlGaAs/GaAs lasers from EG&G were used to determine the effectiveness of the treatment in real devices. To understand and optimize the sulphur passivation process, $Al_xGa_{1-x}As$ epilayers with various aluminum mole fraction, x, and doping concentrations, were investigated. The sulphur passivation itself was performed and optimized at the University of Toronto [50]. The surface quality was determined mainly from measurements of the intensity of the photoluminescence (PL) from the surface of treated samples, however, other surface sensitive techniques such as photoreflectance spectroscopy were used to further clarify the effect of the passivation. The encapsulation

of the sulphur passivated layer, and an investigation of the degradation of the PL intensity with time for the encapsulated material, both sulphur treated and untreated, was carried out at McMaster University, and is the main contribution described in this chapter.

5.1 Surface Properties of GaAs and AlGaAs

For more than three decades GaAs has been an important component of many opto-electronic devices, due to its improved carrier transport properties relative to silicon, as well as its direct band gap. $Al_xGa_{1-x}As$ has also been an important material since it has a band gap which increases with aluminum mole fraction, and is lattice matched to GaAs, allowing for heterostructure devices. Unfortunately, GaAs (100) surface properties are very poor, with a surface Fermi level pinned near midgap, and a high density of interface states. The (100) surface is composed of either all Ga atoms or all As atoms, which results in a high surface energy due to the polar nature of the Ga-As bond. As a result, numerous surface reconstructions with varying stoichiometries have been observed [51]. The surface electronic properties depend very strongly on minor changes in the surface structure. For example, the concentration of GaAs surface states is typically more than $10^{13}cm^{-2}$, which is 1000 times higher than what is typically observed for high quality Si/SiO_2 interfaces, but still represents less than 1 % of the number of possible surface states. The complicated nature of the surface reconstruction makes it difficult to accurately calculate surface electron states even for clean surfaces under a UHV environment. The surface is also prone to oxidation, particularly when aluminum is added to the binary alloy, adding further complications.

The situation is more clear for (110) surfaces, which can be studied by cleaving

in a UHV environment. Because the surface is non-polar, with an equal concentration of Ga and As atoms, there are no surface reconstructions observed, although there is a shift in the relative positions of the atoms near the surface relative to the bulk crystal [51]. As a result of the abrupt termination of the crystal lattice, there are no surface states existing within the bandgap of the material for clean (110) surfaces [52, 53, 54], however, it has been observed that the Fermi level again becomes pinned near midgap after exposure to only 0.05 monolayers of oxygen [55].

The diode laser facet is the (110) surface, while the (100) surface is the growth surface for most epitaxial techniques, since composition control is very difficult on (110) surfaces. For field effect devices, where the variation of the thickness of the depletion region in the semiconductor is important, Fermi level pinning is intolerable. For a "pinned" surface, the Fermi level at the surface is only required to move through a small energy in the band gap of the material in order to charge or neutralize a large number of surface states, making it impossible to induce a change in the depletion layer thickness within the semiconductor. On the other hand, for the purposes of improving laser performance, the important parameter is the recombination rate at the surface. This is characterized by the surface recombination velocity, SRV, which is a function of both the density and energy distribution of the surface states, as well as the position of the Fermi level relative to these states. Referring to Figure 5.1, the rate of recombination at the surface, for a single trap type at energy E_t, is given by the Shockley-Read-Hall (SRH) relation [56]

$$U = \frac{N_t v_{th}^2 \sigma_n \sigma_p (p_s n_s - p' n')}{\sigma_p v_{th}(p_s + p') + \sigma_n v_{th}(n_s + n')}, \tag{5.1}$$

where N_t is the areal density of trap states, n_s (p_s) is the equilibrium concentration

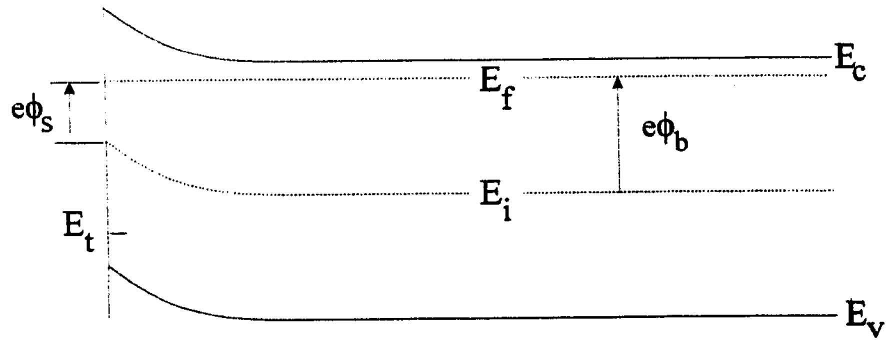

Figure 5.1: A schematic illustration of the conduction and valence band edges near the surface of a semiconductor with acceptor-like surface states.

of electrons (holes) at the surface, and

$$n' = n_i \exp\left(\frac{E_t - E_i}{kT}\right) \tag{5.2}$$

$$p' = n_i \exp\left(-\frac{E_t - E_i}{kT}\right) \tag{5.3}$$

are the product of the equilibrium carrier concentration, without injection, and the occupation probability of the trap for both electrons and holes, or, alternatively, the concentration of electrons (holes) in the conduction (valence) band if the Fermi level was at the trap energy (k is Boltzmann's constant). σ_n (σ_p) is the cross section for capture of an electron (hole) ($\sim 10^{-15}$ cm^2), and v_{th} is the thermal velocity of the carriers ($\sim 10^7$ cm/s). Referring to Figure 5.1, if the surface is in thermal equilibrium with the bulk of the semiconductor, n_s and p_s are related to the carrier concentrations in the bulk, n and p, by

$$n_s = n \exp\left(-\frac{e(\phi_b - \phi_s)}{kT}\right) \tag{5.4}$$

$$p_s = p \exp\left(\frac{e(\phi_b - \phi_s)}{kT}\right), \tag{5.5}$$

where ϕ_s and ϕ_b are defined in figure 5.1. When excess carriers are injected into the semiconductor, the carrier concentrations, n and p, determine the quasi-Fermi levels

of each carrier population,

$$n = n_i \exp\left(-\frac{E_i - F_n}{kT}\right) \tag{5.6}$$

$$p = n_i \exp\left(\frac{E_i - F_p}{kT}\right). \tag{5.7}$$

Finally, n_i is the intrinsic carrier concentration, and E_i is the intrinsic Fermi energy, such that $n = p = n_i$ with no doping in the crystal.

The rate of recombination can be written as a product of a velocity and the density of excess carriers present,

$$p_s n_s - p'n' = pn - n_i^2 = (n_0 + p_0 + n_1)n_1, \tag{5.8}$$

where $n_1 = p_1$ are the excess carrier densities. This defines the SRV as

$$\text{SRV} = \frac{N_t v_{th}^2 \sigma_n \sigma_p (n_0 + p_0 + n_1)}{\sigma_p v_{th}(p_s + p') + \sigma_n v_{th}(n_s + n')}, \tag{5.9}$$

so that $U = \text{SRV} n_1$. SRV is scaled by the number of traps, as would be expected, however, the dependence on the band bending at the surface, expressed through the carrier densities in the denominator of equation 5.9, is quite complicated. From equations 5.2 and 5.3 it is observed that the sum of p' and n' is lowest for traps near E_i. Traps close to the conduction band, for example, are very efficient at capturing electrons from the conduction band, and have a high n', however, the rate of recombination is limited by the very low rate of hole capture, or alternatively, the emission of electrons to the valence band (p' is low). The opposite situation holds for traps close to the valence band, but again the net result is that the sum of n' and p' is larger than if the trap were near E_i. The same argument can be made concerning the level of doping in the semiconductor. When the material is n-type, the traps will capture electrons effectively, however, there are very few holes available to complete

the recombination process. The highest recombination rate is then observed on surfaces where there are large numbers of surface states near the intrinsic Fermi energy, and where the Fermi level at the surface is also near the intrinsic Fermi energy. This is exactly the case which seems to occur for both GaAs (100) and (110) surfaces after exposure to the ambient atmosphere. In contrast. the Fermi level for InP is pinned closer to the conduction band minimum [55], resulting in significantly reduced SRV relative to GaAs.

5.2 Passivation of GaAs and AlGaAs

Direct measurements of the SRV for GaAs yield values on the order of 10^6 cm/s, for air exposed surfaces. By capping the GaAs with a lattice matched higher band gap material, such as AlGaAs, the recombination velocity at the GaAs/AlGaAs interface can be reduced to as low as 40 cm/s [57]. There have been a number of reports of improved surface properties due to sulphur passivation of GaAs surfaces. For example. the performance in heterojunction bipolar transisters has been improved dramatically [49, 58]. In reference [58], SiN_x coatings were applied after sulphur treatment in order to stabilize the surface. Careful investigation of the degree of band bending at the surface indicates that the sulfur treatment does not necessarily reduce the concentration of interface states, but varies the distribution of surface states within the band gap such that the Fermi level is pinned closer to the valence band maximum. thereby reducing the SRV [59]. Various models of the surface state distribution of GaAs, before and after sulfur treatment, have been proposed. For example, Spindt et al. [60] describe a scenario where the initial surface is pinned due to double donor and double acceptor states at the surface. For the particular surface which is supposed, a small drop in the concentration of donor states, due to

the sulphur treatment, moves the Fermi level toward the valence band and can have the effect of greatly reducing the efficiency of recombination through the donor-like surface states.

More recently, capacitance vs voltage (C-V) measurements of metal-insulator -semiconductor (MIS) structures consisting of sulphur passivated GaAs and a SiN_x insulator deposited using the ECR-PECVD process showed a reduction in the interface state density as well as a significant unpinning of the Fermi level [61]. This improvement was only observed after the treated and coated samples were annealed at temperatures above 300°C. A separate study observed a significant increase in PL intensity from sulphur passivated, SiN_x coated GaAs after annealing above 300°C [62]. At temperatures above 300°C hydrogen begins to evolve from the SiN film, and it appears that this hydrogen has a large impact on the surface behavior. MIS structures consisting of sulphur treated GaAs, with an interface control layer consisting of silicon and germanium sublayers and an insulator layer of remote plasma deposited SiN_x were fabricated on both (110) and (100) surfaces [63]. C-V measurements indicated that the sulphur treatment improved the interface properties of both surface types. Low interface state density ($< 2\times10^{12}$ $ev^{-1}cm^{-2}$) and a large capacitance variation in the quasi-static C-V curve indicated a high quality interface after S/Ge/Si/SiN_x passivation. This high quality was observed on both (100) and (110) surfaces, indicating that the sulphur treatment is effective in both cases. In this study, it was assumed that the main effect of the sulphur was the supression of surface oxidation.

It has been observed that for silicon layer thicknesses below 2.5 nm, quantum confinement of the electron states, including the surface states, at the GaAs/silicon interface causes a shift of all electron states near the surface to higher energies, thereby moving them away from the Fermi level, and reducing their efficiency as recombination

Reactions	ΔG^f (kcal/mol)	E^o (eV)
Ga + As → GaAs	-20	0.87
2Ga + $3/2O_2$ → Ga_2O_3	-258	3.74
Ga + O → GaO	-83	3.62
2As+$3/2O_2$ → As_2O_3	-156	2.26
2Al+$3/2O_2$ → Al_2O_3	-404	5.86
2GaAs + As_2O_3 → 4As + Ga_2O_3	-62	2.70

Table 5.1: Gibbs energy of formation for GaAs oxides and aluminum oxide, and the heat of formation per O atom.

centers [64]. It is this effect which makes the silicon or germanium interface control layer an effective passivant.

In contrast to the SiO_2/Si system, the native oxide of GaAs is largly responsible for the poor surface quality of GaAs. The oxide is typically not stoichiometric, consisting mainly of Ga_2O_3 with excess As near the surface region [51]. Table 5.1 shows the heats of formation for the various oxides of AlGaAs, and the associated bond energies [65, 66]. Note the large differences in the heats of formation, indicating that the thermodynamically stable surfaces will be strongly non-stoichiometric.

Recently, careful deposition of a Ga_2O_3 film on a freshly grown (100) GaAs surface with no oxygen exposure resulted in nearly perfect surface properties (D_{it} = $10^{10}/cm^2/eV$, SRV = 6000 cm/s) [67, 68]. The PL intensity from these surfaces was nearly equivalent to that observed on surfaces with AlGaAs capping layers. In addition, there was no degradation in the PL signal after illumination for 24 hours.

5.3 PL as a Surface Characterization Technique

As mentioned, the main technique which was used in this work for the investigation of changes in surface quality was the relative intensity of the PL observed from samples treated in various ways. This technique is often used to investigate surface quality,

since the process of radiative recombination which results in the observation of luminescence is directly competing with non-radiative recombination processes. Any increase in PL is assumed to indicate a drop in the rate of non-radiative recombination occuring at the surface, or alternatively, a drop in the SRV. As was shown above, many factors contribute to changes in the SRV and, as a result, a careful interpretation of PL measurements is essential.

A detailed description of the characteristic features observed in spectrally resolved, low temperature PL measurements on $Al_xGa_{1-x}As$ is given in reference [69]. In this section the surface properties which affect the intensity yield of PL will be described. During PL measurements, the sample is illuminated by an intense monochromatic light source with a photon energy larger than the band gap of the material. This results in the injection of carriers in the material due to absorption, and the separation of the quasi-Fermi levels for electrons and holes defined in equations 5.6 and 5.7. The generation rate is given by Beer's Law

$$G(z,\lambda) = [1 - R(\lambda)]\alpha(\lambda)F(0)\exp[-\alpha(\lambda)z], \tag{5.10}$$

where $R(\lambda)$ is the surface reflection coefficient at the wavelength of the incident illumination, $\alpha(\lambda)$ is the absorption coefficient, z is the depth from the surface, and $F(0)$ is the flux of photons incident on the sample. A more detailed description of the minority carrier concentration as a function of z, including the effect of surface recombination, diffusion of minority carriers and band bending, is given in references [70, 71], however the trends considered here are still valid.

Assuming that the surface states are able to stay in thermal equilibrium with the bulk of the semiconductor, these states will be neutralized by the excess injected carriers, generally resulting in a decrease in the surface band bending. Two factors will affect the PL intensity observed for a given intensity of illumination, i. e., the

variation of the surface concentration of electrons and holes, n_s and p_s as the bands flatten, and the reduction of the space charge region in the semiconductor. This space charge region is generally considered to be a "dead layer" for recombination because of the electric field which separates electrons and holes [70], and so the volume for radiative transitions increases with decreased band bending, increasing the intensity of PL observed. This effect is smaller in doped material than in undoped material, due to the low initial thickness of the dead layer in doped material. The dependence of the SRV on the illumination intensity is quite complicated. As an example of the possible behaviour. consider an n-type semiconductor with a single acceptor like trap as in Figure 5.1. If the trap concentration is high enough, the surface Fermi level is pinned at the trap energy. For this case, the surface is inverted relative to the bulk of the semiconductor, with a higher concentration of holes. The injection of carriers will begin to neutralize the acceptors due to the increased concentration of holes. This reduces the band bending, p_s increases slightly, while n_s increases more significantly. The SRV increases as the ratio n_s/p_s approaches 1. The important parameter is the ratio of n_s/p_s. At high injection, $n_s = p_s$, and so the SRV becomes a independent of intensity. For Figure 5.1, n_s/p_s is already greater than 1, but again, increased carrier injection increases the SRV as n_s/p_s approaches 1. Figure 5.2 shows the same surface as Figure 5.1, but now with a significant carrier injection. The surface states are neutralized by the excess carriers, and the band bending at the surface is reduced relative to Figure 5.1. As a result, the sum of p_s and n_s is increased, while the band flattening increases the volume available for PL. Both of these factors contribute to an increased PL intensity in addition to the expected linear increase in the signal with the incident illumination intensity.

An important factor which has not been considered, i. e., fixed charge at the

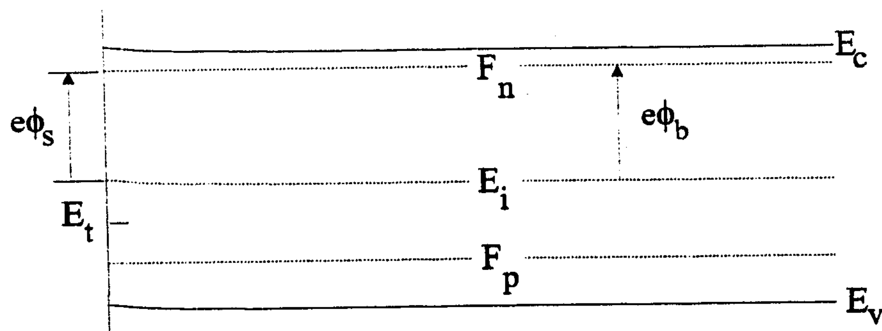

Figure 5.2: The conduction and valence band edges near the surface of a semiconductor with surface states under high level injection conditions.

surface of the semiconductor, has a large effect on the observed surface recombination velocity under conditions of high level injection [48] . Fixed charge is often observed when some form of passivation coating is applied to the surface, particularly when dielectric coatings are used. The charge is observed in many dielectric materials, and is due to defects, or dangling bonds, either within the film, or very close to the dielectric/semiconductor interface. Under high level injection conditions, the presence of a fixed charge, which is not in thermal equilibrium with the semiconductor, acts to bend the bands again. As a result either holes or electrons are removed from the surface, depending on the sign of the charge, reducing the SRV in both cases. This would have the effect of increasing the PL intensity, however, the space charge dead layer increases in volume, counteracting this effect to some degree.

The situation near the facet of a SDL is similar to the case described above. There is a significant excess of carriers, and negligible doping in both the active and cladding layers. When the laser is operated above threshold current, the quasi-Fermi levels of electrons and holes in the bulk of the laser active region are separated by at least the energy of the emitted photons. This is the transparency condition where a transition from absorption to gain occurs in the laser material. Near the

facets of the laser. surface recombination acts to reduce the concentration of excess carriers, reducing the quasi-Fermi level separation. and promoting absorption of the laser light. This leads to heating, which locally reduces the band gap of the material, further enhancing the facet absorption. It is seen that the surface states are the trigger for facet degradation. the reduction of radiative efficiency near the laser facets has been observed directly in operating SDL's [45]. Efforts to reduce the surface state recombination efficiency will result in improved device reliability characteristics.

5.4 Facet Degradation in SDL's

The basic degradation process which results in the failure of a SDL through COMD has already been described. Several measurements have been made of the local temperature at the active region on the facet of various types of laser structures in order to observe the local facet heating directly [72, 73, 74, 75, 76]. Thermoreflectance measurements established two domains of temperature increase for visible wavelength, InGaP strained quantum well lasers with AlGaInP or AlGaAs cladding layers [76]. Below threshold, the temperature increase at the laser facet is close to the bulk temperature rise in the laser, and is due mainly to Joule heating from resistive losses in the laser structure. Above threshold the temperature increases more rapidly, due to the onset of optical absorption at the facets. The measured temperature increase was typically less than 50 K for 5 μm stripe lasers operated at a relatively low optical power (15 mW) and was found to depend sensitively on a number of parameters. The temperature rise was lowered by a factor of 2.5 when AlGaAs was used as the cladding layer, rather than AlGaInP. This was attributed to a reduced resistivity in the AlGaAs layers. The heating depended linearly on the number of quantum wells in the structure, it was reduced by a factor of 2 when the laser was mounted with the

junction side facing the heat sink, and was found to drop by another factor of 2.5 if a 5 μm gold heat spreader layer was applied on the top surface of the laser, right to the edge of the facet. If the heat spreader layer was recessed 10 μm from the edge of the facet it had no impact on the facet temperature increase. This was consistent with spatially resolved electroluminescence measurements that showed that the temperature distribution close to the facet had an exponential profile as a function of distance from the facet with a 1/e depth of 6 μm. At output powers near the COMD limit, the facet temperature was measured to be significantly higher, approximately 140°C, averaged over a spot size of 1.5 μm.

A detailed theoretical model of heating effects, and thermal runaway in SDL's was recently reported [75]. Several processes were included as heat sources in the model, i. e., heat generation due to surface recombination, bandgap shrinkage due to the temperature increase at the facet, absorption due to the non-uniform carrier distribution near the facet, and a drift current of both electrons and holes towards the facet surface due to the reduction of the quasi-Fermi levels of both holes and electrons as the band gap is reduced near the facet. To determine the threshold power for thermal runaway, the steady state temperature, T_Δ, for a given heating power was calculated. The heat power dissipated at this steady state temperature was also calculated. If the heat generated could not be dissapated, then no solution for the steady state temperature existed, and thermal runaway would occur. Unrealistically high values of COMD (75 MW/cm^2) were calculated for GaAs/AlGaAs lasers, unless other contributions in addition to facet heating were included. Including the effect of Joule heating and non-radiative recombination in the bulk of the laser resulted in a predicted COMD limit of 25 MW/cm^2, still a factor of 5 higher than the experimentally measured value of approximately 4.4 MW/cm^2 for GaAs [77]. This was despite

the fact that a high value was used for the SRV in the model (3×10^6 cm/s). The predicted COMD power level for InGaAsP based lasers was an order of magnitude larger, mainly due to an equivalent decrease in the magnitude of the SRV assumed for this material.

The various chemical changes which result in both the gradual degradation, as well as COMD at the laser facet are difficult to quantify. For uncoated (110) facets an increase in the SRV was observed for both InP and GaAs when exposed to O_2 environments, as determined by PL intensity measurements. If the ambient was switched to nitrogen, the SRV for InP recovered, however, the SRV remained high for GaAs. This indicates that, for InP, the O_2 molecules adsorb on the surface, whereas the O_2 chemisorbs and oxidizes the GaAs surface [78]. Several studies have shown an enhancement of the oxidation rate of many materials used in laser manufacturing due to photo induced reactions [43]. Measurements of the oxidation rate of various III-V alloys under ~ 5 kW/cm^2 illumination from a 488 nm Ar^+ laser were made to determine the sensitivity of different laser designs to the ambient operating environment [79]. It was found that the oxidation rate of GaAs was higher than any alloy of GaAs with either In or P. In another study at lower optical excitation (60 W/cm^2) and higher oxidation temperature (T = 820°C), the oxidation rate of GaAs (100) surfaces was enhanced by a factor of 5 relative to the oxidation rate observed for unilluminated samples [80]. On (110) surfaces the oxidation rate was enhanced by a factor of 15. The authors interpreted the variation of the oxidation rate for different surfaces to indicate that the effect of the illumination was at the interface between the oxide and the GaAs, and not in the oxide itself. It was also noted that the illumination produced an As_2O_3 component in the oxide which was not observed for thermal oxidations.

Detailed measurements of AlGaAs/GaAs quantum well lasers showed that the time to COMD can be predicted accurately by a simple Arrhenius rate equation,

$$1/t_{COMD} = \nu \exp(-E_a/kT), \tag{5.11}$$

where t_{COMD} is the predicted time to failure, ν is the frequency term, and E_a is the activation energy [65, 81]. The temperature was obtained from measurements of the relative intensity of the Stokes to anti-Stokes phonon transitions in the Raman scattered light observed at the laser facet, and was related to the optical power per unit stripe width of the laser by

$$T = cPD, \tag{5.12}$$

with c, the proportionality constant in units of K(mW/μm)$^{-1}$, and D the active layer thickness. Both coated and uncoated lasers displayed the same values of ν and E_a, however, the parameter c was reduced with the coating. This behavior was interpreted to indicate that the COMD was triggered by the same process, facet oxidation, and that the Arrhenius parameters were particular to the state of the oxide which immediately formed on the cleaved facet prior to the optical coating. These parameters could be varied by varying the state of the oxide on the facet e. g., by plasma oxidation. It was observed that changes in ν and E_a were strongly correlated, variations in one parameter being compensated by similar variations in the other. This strong correlation allowed for the isolation of a characteristic energy for the oxide, E_o, which determined all three parameters controlling the time to COMD failure, ν, E_a and c. This characteristic energy was closely related to the energy per O atom in the facet oxides, E^o, defined in table 5.1. Surfaces with mainly Al-O bonding were observed to have high COMD limits (small ν), but high facet heating and a low activation energy, resulting in a short t_{COMD} at low output powers. Conversly, surfaces which consisted of mainly As-O bonding had a low COMD limit,

but longer lifetime at lower powers. For this model of facet degradation, the key factor in improving reliability is the reduction of oxide formation.

The AlGaAs/GaAs material system is seen to be particularly suceptible to oxidation, possibly limiting the usefulness of this material system for high power laser applications. Since InGaAsP can be lattice matched to GaAs with a band gap ranging from 1.42 eV (GaAs) up to 1.9 eV for (InGaP). Aluminum free laser designs are possible, however, the growth and processing of these lasers tends to be more complicated. These lasers typically have significantly higher COMD values for uncoated facets (6 MW/cm^2), however, if possible, the elimination of facet degradation in the AlGaAs/GaAs lasers will yield a more versatile high power laser. To this end, sulphur based passivations, as well as more novel optical coating procedures have been investigated as methods for obtaining high quality facets. Although not practical on a large scale, AlGaAs epilayers were grown by MOCVD on cleaved laser facets [82]. A high concentration of aluminum was used to produce a transparent facet. COMD was not observed up to a power density of 3 MW/cm^2, however spatial hole burning limited the optical output power. Similar results have been obtained more recently with the growth of ZnSe, another nearly lattice matched semiconductor with a large bandgap, as the transparent mirror [83, 84]. Measurements of increased COMD powers through the use of sulphur treatments have also been reported [85, 77]. In reference [77], COMD powers in AlGaAs stripe lasers were consistently increased by a factor of 60% after treatment with P_2S_5-NH_4OH, followed by a $(NH_4)_2S$ rinse. No details of the cladding and active layer composition were given, nor the operating wavelength of the laser. Direct measurements of the leakage current associated with the facet surface states have been determined from the optical power-voltage-current characteristics of lasers under low injection conditions [86, 87]. These measurements

showed a reduction in the leakage current after sulphur treatment. The reoxidation, or degradation of the laser facet to its original state was also observed for uncoated sulphur treated facets stored for several days in different ambients. It was found that sulphur passivation using an $(NH_4)_2S$ based treatment increased the COMD limit from 350 mW prior to treatment, to 420 mW. No details of the variation of the COMD limit from device to device were given. It was also found that coating the sulphur treated surface with SiN_x, deposited using a remote microwave excited plasma did not increase current leakage, but stabilized the sulphur passivation.

No information concerning the long term reliability of sulphur treated laser facets has been located in the literature. The wet chemical processing of a cleaved laser facet will result in the production of local defects on the surface due to dust, and impurities in the chemicals. Facets treated in this manner may have good short term high power properties, however, for longer periods of operation, defects on the facet will act as the nucleation site for facet degradation. In the experiments carried out as part of this work, the COMD power before and after sulphur treatment was not measured, partly due to the high power levels required for COMD ($\sim$ 40 W), but also since this parameter does not necessarily indicate an improved long term high power reliability after the sulphur treatment.

5.5 Experimental Details

As already mentioned, the sulphur passivation was carried out at the University of Toronto. The details of the sulphur passivation process, as well as the parameters which were varied to obtain the highest quality surface, can be found in reference [50]. Encapsulation with SiN_x was performed on samples treated with an $(NH_4)_2S$ solution. Before the $(NH_4)_2S$ treatment, the wafers were 'pre-etched' in a solution of

H_2SO_4:H_2O_2:H_2O (1:8:500 dilution ratio) at room temperature. The pre-etch was used to remove the native oxide from the surface. It was necessary to use a heavily diluted solution in order to minimize the roughening of the surface due to the acidic etch. Wafers were then soaked in 20 % $(NH_4)_2S$ at a temperature of 65°C and under illumination by a 100 W white light source.

At the University of Toronto, spectrally resolved PL measurements were made as a function of temperature and optical power using an Ar^+ ion laser operating at 488 nm. For these measurements, the temperature could be varied from 15 K to 300 K using an evacuated cold head, while the optical excitation intensity was 4 W/cm^2. The luminescence associated with both donor and acceptor bound excitons in the material, free to bound emission from carbon acceptor impurities, as well as lower energy emissions associated with optically active deep level defects was observed. To determine the quality of the surface, two samples cleaved from the same wafer were mounted for PL measurement. To measure the effects of sulphur treatment only, one sample was untouched, while the other was treated. To measure the impact of both the coating and sulphur treatment, a reference wafer, untreated but coated during the same deposition as the treated wafer, was used as the reference. The surface quality was then determined by the relative enhancement of the bound exciton peak in the PL emission spectrum. As a result, corrections for the variation in the reflection coefficient of the semiconductor surface were not required in order to normalize the intensity of the PL signal for coated and uncoated samples. For the coating thickness used in these experiments, the reflection coefficient at the illuminating wavelength was only slightly less than that of the semiconductor, however, R at the PL emission wavelength was close to 0, and so the PL signal could be increased by approximately 30% due to the coating alone. Even under conditions of $R = 0$ for both the illumi-

nating light and the PL emission. the enhancement would still only be a factor of 2.

Room temperature spectrally integrated PL measurements were performed at McMaster University in order to investigate the properties of the surface in the ambient environment, as well as to characterize the stability of the surface. The degradation in the intensity of the PL emission was used as a measure of the stability of the SRV under photo-excitation conditions similar to what would be observed at the laser facet. The confocal PL measurement system shown in Figure 5.3 was used to measure the PL degradation [88]. Both a He-Ne laser operating at 633 nm

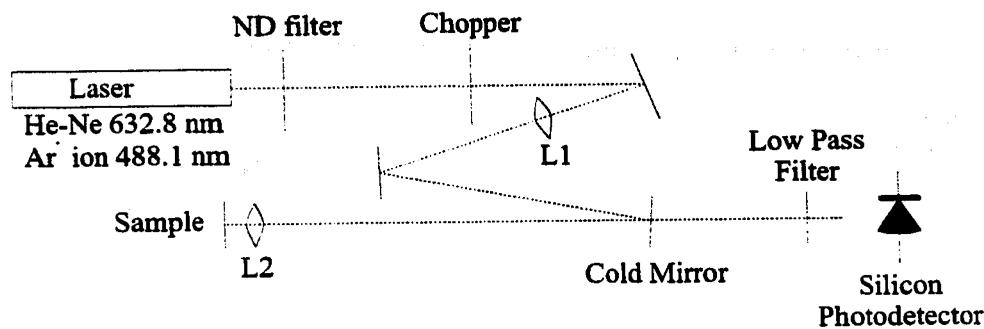

Figure 5.3: A schematic diagram of the integrated PL measurement system.

(penetration depth $\approx$0.3 μm), and an Ar^+ ion laser operating at 488 nm (penetration depth $\approx$0.1 μm) [69] were used as the illumination source. The illuminating light was reflected off of the cold mirror and focused on the sample using lens L2. The PL signal was collected using the same lens and passed through the cold mirror, a low pass filter was used to block residual laser light from reaching the silicon photodetector. Lens L1 (focal length = 50 cm) was used to reduce the effect of chromatic aberration in L2, which focused the short wavelength laser light and also collected the longer wavelength PL emission. To improve the signal to noise ratio of the measurement, phase sensitive detection was used. Strong focusing by lens L2 resulted in an illumination intensity

of 39 kW/cm^2, assuming a spot size of 2 μm for both lasers. The power could be reduced using calibrated neutral density filters. Both the (100) surface and the (110) facet of treated material could be investigated. For the (110) facet, only the substrate was probed; measurements of changes in the luminescence of the laser structure itself were not possible due to the limited resolution of the sample positioning stage.

A series of (100) $Al_xGa_{1-x}As$ epilayers grown by metalorganic chemical vapour deposition with x ranging from 0 to 0.41 were used to evaluate the sulphur passivation and encapsulation procedure. Both undoped ($N \sim 10^{15}$ cm^{-3}) and doped ($N \sim 10^{18}$ cm^{-3}) material was investigated. Once an effective sulphur treatment was obtained on the wafer material, the samples were encapsulated using the ECR-PECVD system. Based on the intensity of the PL for samples measured at different times after the sulphur treatment, it was determined that the stability of the surface in the ambient environment depended on the mole fraction of aluminum in the material. Higher Al content resulted in a more rapid reoxidation of the surface. For GaAs surfaces, the treatment was stable for a number of days, however, for $Al_{0.11}Ga_{0.89}As$, a measureable drop in PL was observed within 24 hours of the treatment. As a result, all encapsulations were performed within 1 day of the sulphur treatment.

It was found that SiN_x deposited using TDAS as the silicon precursor, in an argon discharge produced higher quality surfaces when compared with SiO_2 encapsulations. The effectiveness of the encapsulation process was very sensitive to the manner in which the film deposition was initiated. Direct plasma exposure to the uncoated surface resulted in a removal of the sulphur, or simply damaged the ordered nature of the sulphur terminated surface resulting in a return of the PL intensity after coating to that of an untreated, coated surface. In order to avoid this direct plasma exposure, the samples were shuttered for the first 3 to 5 minutes of the deposition,

Step	Time (hrs)	Current (A)	Pulse width / frequency (ns / kHz)
0	0	ramp to 22	50 / 10
1	48	22	50 / 10
2	48	22	100 / 10
3	48	22	200 / 10

Table 5.2: Typical test sequence for evaluating the impact of facet treatments on the performance of the laser.

avoiding the direct ion bombardment of the surface. A film thickness of approximately 100 Å was obtained during this time, as measured by the in situ ellipsometer, mainly due to deposition from neutral radicals. After this, the shutter was removed and the deposition proceeded as usual. It was found that a maximum microwave power of 800 W could be used before a drop in the PL enhancement of the sulphur treated surfaces was observed. At a power of 1000 W, the PL intensity was reduced to below the pre-treated level, again indicating damage to the surface.

Laser facets were sulphur treated and coated using the optimum parameters obtained from the investigation of the epilayer material. The effect of the various facet treatments on the degradation of the laser output power with time at a constant current was measured. Table 5.2 shows a typical test sequence which was used to evaluate the performance of the treated lasers. The light output versus current was measured for the unstressed laser. after this the power output at the indicated current was measured after each stress period. A current of 22 A corresponds to an optical power of 15 W. or a power density of approximately 5 MW/cm^2 assuming a 1 μm$\times$300 μm emitting aperture. The typical COMD power for these lasers was in the range of 30 W output power, and so the life test was performed at a significant power relative to the COMD limit. Typically 1 to 5 bars consisting of approximately 5 lasers each were used to obtain some measure of the variation in quality observed

for a given treatment. Effects such as reflectance non-uniformity, as well as the degradation due to large defects, for example from surface cleaving steps and mechanical damage on the facet, could be observed and taken into account when interpreting the data.

For comparison, the standard coating applied to the laser facets by EG&G consisted of a 1 to 2 minute argon ion clean, followed by the ion assisted electron beam evaporation of an Al_2O_3 layer with an optical thickness of $\lambda/2$ for the low reflectance facet. The opposite facet coating was a 6 layer quarter wave high reflectance filter with an Al_2O_3 low index layer and an amorphous silicon high index layer. This coating procedure resulted in a reflectance of 30% on the first facet and > 90% on the second facet. The threshold current measured for the lasers was approximately 2.8 A without facet coatings, and was reduced to 1 A after coating. The surface temperature during the facet coating was measured to be approximately 300 °C.

5.6 Low Temperature PL Measurements

Figure 5.4 shows the effect of sulphur treatment and SiN_x encapsulation on a 6 μm thick $Al_xGa_{1-x}As$ film with x=0.11. Several features are apparent in the PL spectrum. The peak at 1.665 eV is due to bound exciton (BE) emission. The lower energy peak at 1.647 eV is attributed to free to bound emission involving shallow carbon acceptors (e^0,A). Two deep level emission peaks were also observed at 1.35 eV and 1.485 eV, associated with silicon-vacancy defect complexes and possibly germanium impurities, arising from source gas contamination, respectively [50].

After sulphur treatment, the intensity of the bound exciton emission peak was enhanced significantly relative to the carbon acceptor peak, the enhancement factor in this case being 20. After encapsulation, a furthur enhancement of the bound

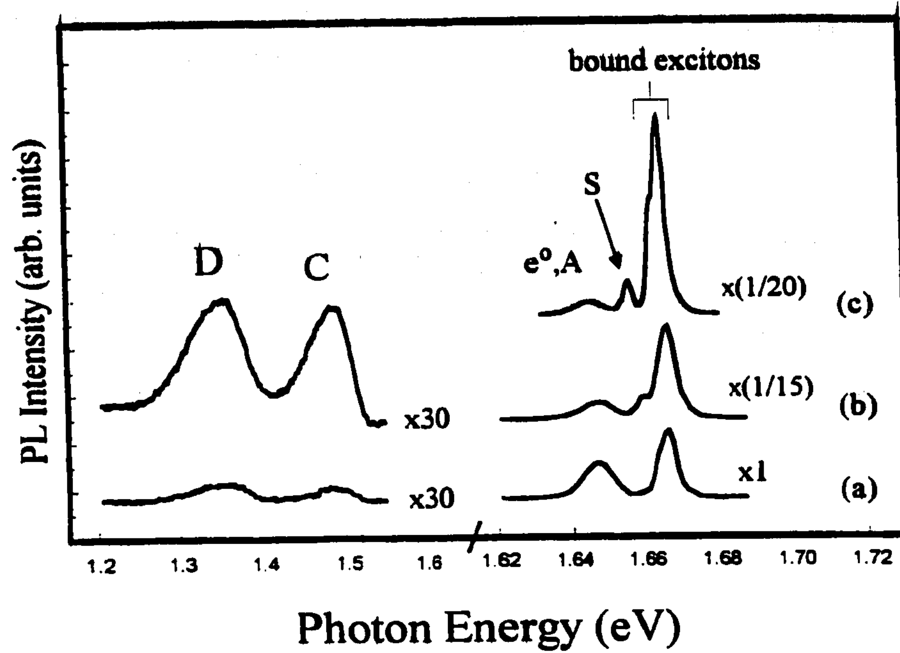

Figure 5.4: Low temperature PL spectra of undoped $Al_{0.11}Ga_{0.89}As$ (a)untreated, (b)sulphur treated and (c)sulphur treated and encapsulated with 100 nm SiN_x.

exciton emission was observed, bringing the total enhancement factor up to ~ 60. The reduction in the relative intensity of the carbon related peak indicates that carbon incorporated near the surface is reduced during the acid pre-etch and that the sulphur terminated surface prevents the reincorporation of this carbon. There is a redshift in the peak position of the bound exciton peak of 1.4 meV, indicating that there is tensile stress induced in the substrate due to the SiN_x coating. This is consistent with a compressive stress observed in the films deposited using TDAS and an argon plasma. The origin of the additional peak (S) which is present in the spectrum for the encapsulated surface has not been uniquely identified, however. the presence of this peak correlated strongly with the effectiveness of the passivation, increasing in intensity for larger PL enhancement ratios. This transition was only observed after the encapsulation. The peak is red shifted by 9 meV relative to the bound exciton emission, and coincides in energy with the so called defect exciton (d,X) peak sometimes observed in MBE grown $Al_xGa_{1-x}As$ [89, 90]. Another possible origin for this peak could be an optical transition involving excitons bound to neutral donors in which the donor electron is excited to the conduction band minimum [69]. This "two-electron" transition is red shifted in energy by the donor binding energy, which for $Al_{0.11}Ga_{0.89}As$ is 8 meV. The transition involves two coherent processes, and hence occurs only in samples with low impurity content, however, the incorporation of silicon as a donor in the surface layer of the encapsulated sample could produce this transition.

Figure 5.5 shows the measured enhancement of the intensity of the bound exciton peak after sulphur treatment and encapsulation for the (100) surface of $Al_xGa_{1-x}As$ as a function of x. The most notable feature is that in all cases, the encapsulation increases the level of enhancement, quite dramatically for $Al_{0.11}Ga_{0.89}As$, as

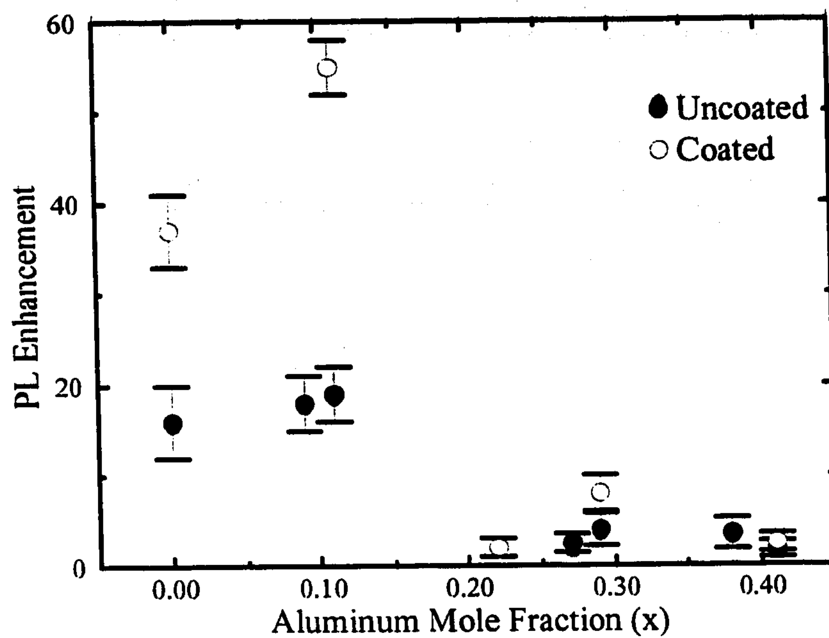

Figure 5.5: Measured PL enhancement as a function of aluminum mole fraction for sulphur treated and sulphur treated and encapsulated $Al_xGa_{1-x}As$.

discussed previously. In general, the overall enhancement factor is reduced for higher aluminum mole fractions. The treatment used for all compositions was optimized for low x material, and so the increased surface oxidation prior to passivation for high x materials would require a more aggressive pre-etching procedure. Significant differential etching was observed in aggressively pre-etched laser facets, indicating a much higher etch rate for higher x material. An example of this is shown in Figure 5.6. As

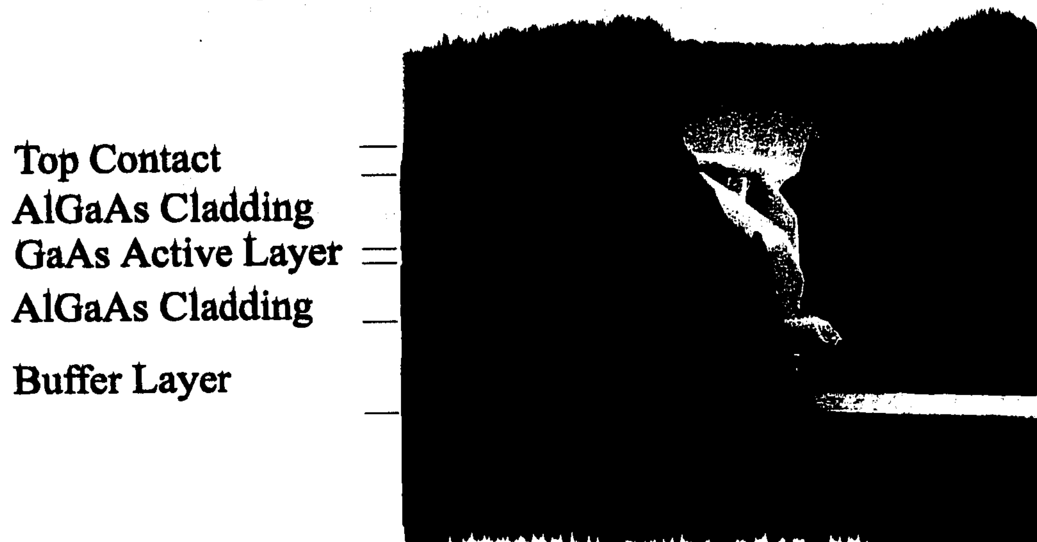

Figure 5.6: SEM image of a sulphur treated laser facet prior to optimization of the pre-etch solution.

a result, the dilute pre-etch solution used for these treatments optimized the PL of low x material, without inducing significant changes in the facet morphology. As well, for high x material, the stronger tendency for the reoxidation of the treated surfaces, may limit the PL enhancement observed after the sulphur treatment, even if a more aggressive pre-etch is used. It should be noted that for the encapsulated material, the PL enhancement factor of the aluminum containing epilayers was unchanged after 6 months of storage, indicating that the SiN_x coating stabilizes the sulphur passivation effectively. Another important feature of the treatment of (100) $Al_xGa_{1-x}As$

is that the PL enhancement of doped material was very low for both p and n-type doping. Only films with a 29% aluminum content were tested, for both dopant types the enhancement factor was less than 40%. For GaAs, it has been observed that the PL enhancement of p-type material is higher than that for n-type material [91]. To explain this behavior, it was assumed that the sulphur treatment reduced the concentration of donor like surface states in the upper half of the band gap. These traps would be efficient recombination centers in p-type material, since they are efficient at capturing the minority carriers, but less important for n-type material.

5.7 PL Decay Measurements

Figure 5.7 shows the effect of the optical coating on the stability of the passivation for sulphur treated samples illuminated with an intensity of 39 kW/cm^2 from the HeNe laser. The degradation characteristics are significantly improved by the optical coating as would be expected. The PL signal decays to half of it's original value after a time of less than 10 seconds for the uncoated surface. Although not indicated in the figure, much longer illumination times of 300 to 600 seconds are required to observe an equivalent decay for the coated surfaces. This is to be compared with data reported in the literature. In reference [67] the PL decay of $(NH_4)_2S$ treated n-type GaAs was measured as a comparison to passivation by Ga_2O_3. A PL decay from an initial value 20 times that of an untreated surface to 2 times occurred after 1 hour of illumination. The measurement was performed under an illumination intensity of 1060 W/cm^2, at $\lambda = 514.5$ nm.

In order to observe the effect of the sulphur passivation alone, treated and untreated reference samples were coated during the same deposition. Figure 5.8 shows the PL decay measured in this case after much longer illumination times. Note that for

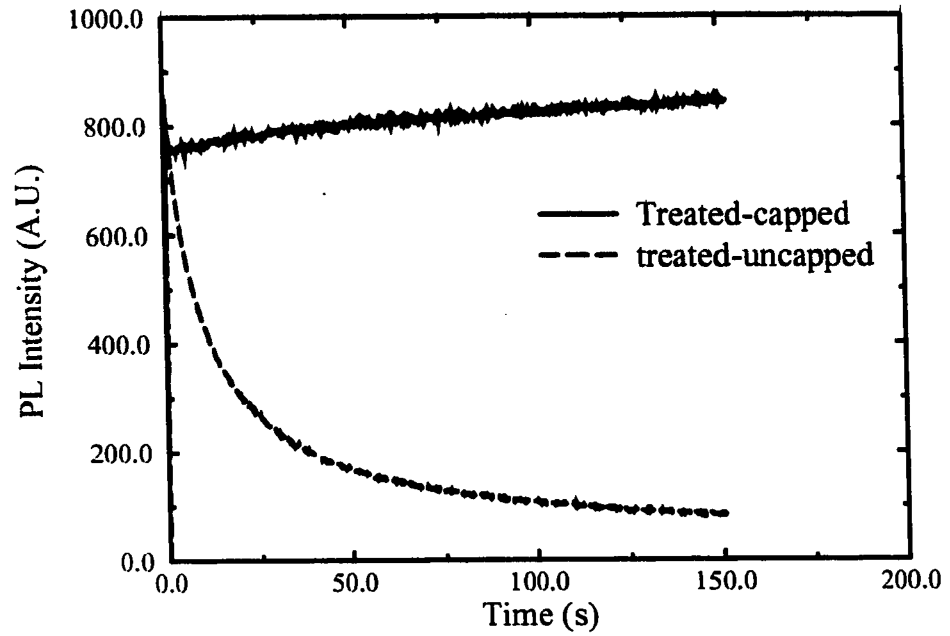

Figure 5.7: The effect of the optical coating on the PL stability for (100) GaAs surfaces.

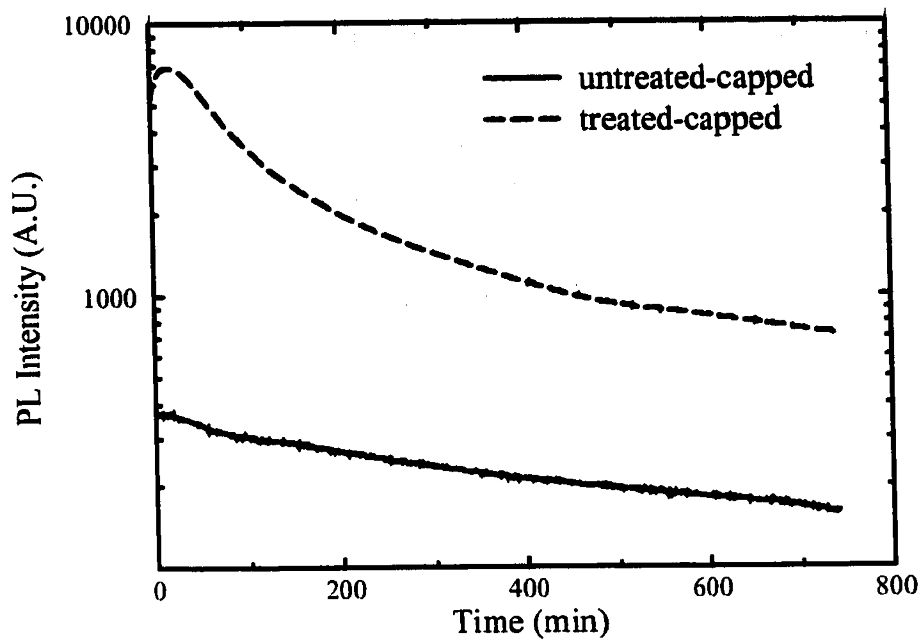

Figure 5.8: The effect of the sulphur treatment on the PL stability for coated (100) GaAs surfaces.

the room temperature integrated PL measurement, the enhancement factor is similar to what was determined from the low temperature measurements, approximately 13 in this case. An interesting feature of the coated-treated sample is that, initially, the PL increases with time. This initial increase of PL with time is not as significant in the untreated samples. After several hours of illumination it is observed that the PL intensity from the treated surface decays to a value close to that of the untreated surface. For times longer than this, the decay rate is similar for both the treated and untreated surfaces.

The rate of PL decay was dependent on the wavelength of the laser source, the time required for a decay of the PL intensity to half of it's initial value was higher by a factor of 2 for the 633 nm source when compared with the 488 nm source. Since the absorption coefficient for the 488 nm light is higher by a factor of 3, the carrier generation rate close to the surface is higher, promoting a more rapid PL decay.

The remaining parameter which affected the PL decay was the intensity of illumination. Figure 5.9 shows the PL decay measured for 39 and 3.6 kW/cm^2 illumination power, using the 632 nm source. In this case the relative intensity has been normalized to the PL intensity at the end of the test. Although the initial PL decay is significantly higher at high intensity, the long term decay is nearly identical, indicating that the same process, which is independent of the optical generation rate, is inducing the degradation.

It has been mentioned that the microwave power used for the deposition of the encapsulating film has a significant impact on the surface properties. To investigate this further a set of sulphur treated GaAs samples were initially exposed to a deposition plasma with varying microwave power. Figure 5.10 shows the effect of varying the initial microwave power of the argon+TDAS plasma exposure before ramping the

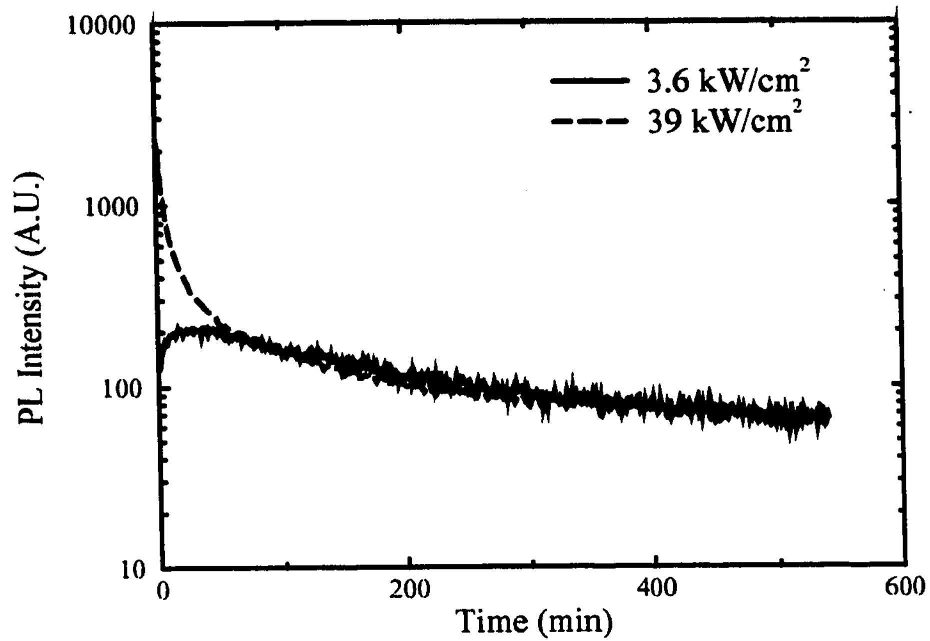

Figure 5.9: The measured PL decay for illumination at 632 nm with 39 kW/cm^2, and 3.6 kW/cm^2 intensity.

power up to 800 W (4.4 W/cm^2) for a normal deposition. As the power is increased,

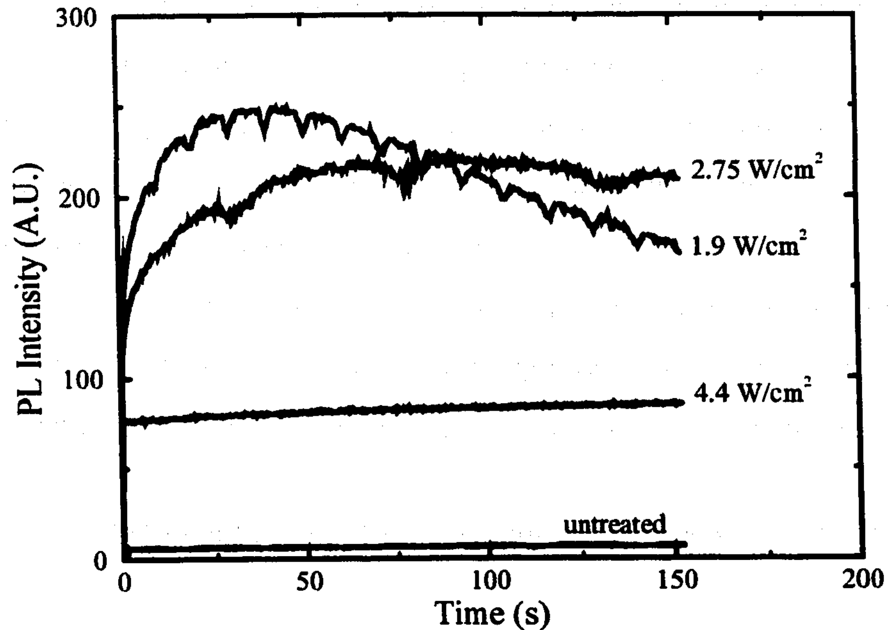

Figure 5.10: Measured PL intensity versus time after various plasma exposures.

the PL signal becomes more constant with time, however, the enhancement factor is reduced. Considering only the variation with microwave power, the initial increase of the PL with time is highest for the deposition at lowest power, however, the stability of the PL with time is the least in this case.

All of the measurements discussed above were made on (100) surfaces. For (110) surfaces. both the PL intensity measured for treated and untreated surfaces and the PL degradation characteristics are quite different. For untreated (110) surfaces of n-type GaAs with a doping density of $10^{18}/cm^3$, the initial PL intensity is nearly equal to that observed after treatment on (100) surfaces. The PL intensity increases by a factor of between 1.5 and 2 with treatment, a significantly lower enhancement,

compared to what is observed on the (100) surfaces. The degradation characteristic is also quite different. Even after hours of illumination, there is usually no degradation of the PL intensity for the untreated material. For the treated material, the PL intensity degrades initially with a time constant similar to the (100) surfaces, but stabilizes at an intensity similar to that observed on the untreated surface. Figure 5.11 shows the PL intensity versus time after exposing a laser facet to a 30 second 1000 W argon plasma as a cleaning treatment. This was the highest PL signal observed for any surface treatments, with the signal increasing significantly with time. Since it

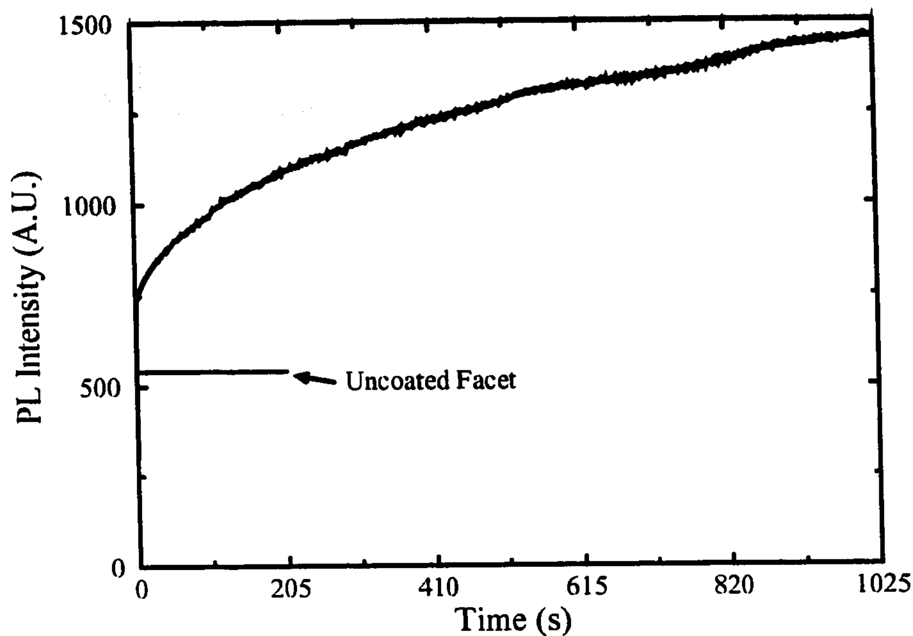

Figure 5.11: Measured PL intensity versus time for a (110) laser facet after a 30 second argon plasma exposure and SiN_x film deposition.

is known that this plasma treatment removes the sulphur passivation effect, even for much shorter exposure times, the variation of the PL intensity with time seems to indicate an instability in the surface recombination velocity which is due to damage

induced in the substrate. It is interesting that the PL intensity is actually highest for this case. indicating that the stability of the PL over time is a more important indicator of damage than the intensity of the luminescence. Reliability tests of lasers with this facet coating did not perform well when compared to similar tests of lasers coated using the EG&G standard coating procedure.

The variation of the PL with time can be due to a number of factors. Local heating by the optical beam should be quite small (on the order of a few degrees Celsius), since the incident intensity is lower than the COMD limit by 2 orders of magnitude. The illumination could induce defect production in either the semiconductor or the dielectric coating, thus changing the SRV. Considering the fact that the passivating effect of the sulphur is still significant relative to the untreated and coated material, the effect seems to be more localized either in the film, or very close to the facet interface, and is not due to induced damage in the laser material. At low powers, metastable bonding configurations could be present in the film, due to incomplete surface reactions during deposition at the cold surface. Upon illumination, optical excitation of these bonds would result in the production of charged defect states. Under high level injection conditions, this surface fixed charge would induce band bending and reduce the observed SRV, as described earlier. As the time of illumination is increased, these charged defects could diffuse to the film-facet interface and become neutralized by carriers in the semiconductor. This is one scenario which could explain the positive excursion in the PL intensity with time. In other experiments, a large improvement in the surface quality after annealing at 300°C for 30 minutes was observed [61, 62]. This effect occurred only when SiN_x was used to encapsulate the sulphur treatment and could possibly be due to the diffusion of hydrogen to the interface. Hydrogen is often associated with charged defects in silicon

nitride and is highly mobile at temperatures above 300°C [92].

5.8 Performance of Treated Lasers

A description of the life testing procedure for treated lasers was given in section 5.5. At McMaster, the L-I measurement system described in chapter 4 was used to determine the impact of the sulphur treatment on the observed threshold and external quantum efficiency of the treated lasers. Under treatment conditions where significant differential etching occured on the laser facet due to the pre-etch, the threshold increased by approximately 10%, however, with the final treatment, similar L-I characteristics were obtained before and after sulphur treatment. Unfortunately, the low maximum current of this measurement station prevented both the evaluation of the COMD limit, and the long term reliability of the sulphur treatment at McMaster, and so reliability tests were only carried out at EG&G. As mentioned earlier, argon plasma pre-cleans at microwave powers of 1000 W induced damage in the material, which resulted in poor performance during life testing. Figure 5.12 shows the measured output power after four stressing steps for the standard EG&G coating process, and the McMaster $\lambda/2$ coatings of SiN_x using the argon pre-clean followed by the application of a high reflection coating at EG&G. The error bars indicate the standard deviation of the optical power observed for five chips tested from a single bar. The stress steps for the EG&G test are indicated in the figure. Note that each step for the McMaster coating test is 65 hours, except for step four, which is 50 hours. Also, the pulse width for step four of the McMaster coating test is 150 ns, rather than 200 ns. The remaining parameters were identical for both tests. The variation in the initial power for the different chips is most likely due to non-uniformity in the reflectance of the high reflectance coating. Unfortunately, there is no test data available for

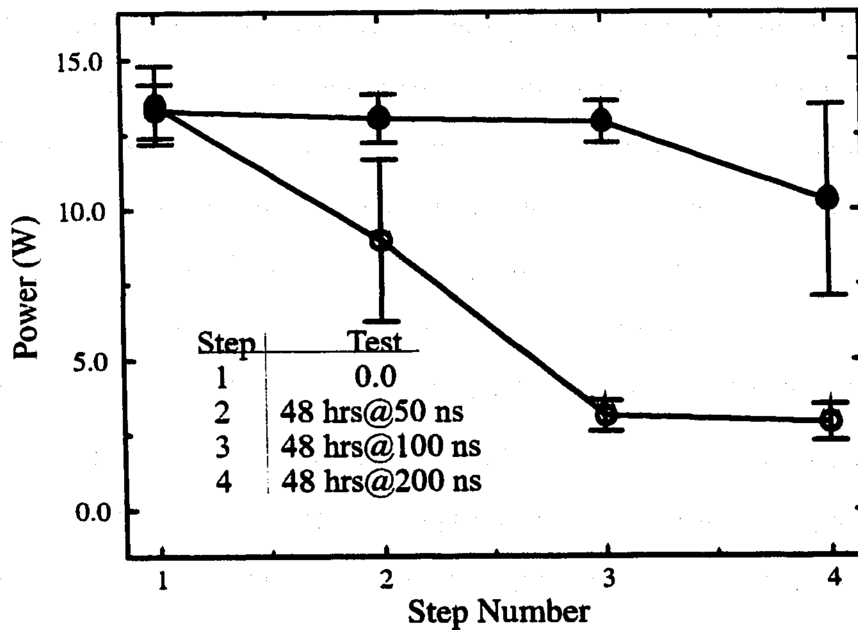

Figure 5.12: Measured optical power at constant current for (•) EG&G coated lasers, (o) McMaster coated lasers with an argon preclean.

the more gentle coating conditions, where no PL changes with time are observed on tested facets. The pre-cleaning procedure was used to imitate the argon ion clean used during the EG&G standard coating procedure, however, it was later determined by the PL decay measurements that the plasma clean is damaging at this power level, and therefore, this step should be avoided, or performed at a lower power.

The reliability test results obtained for lasers with sulphur passivated and encapsulated facets are shown in Figure 5.13. In this case, there is a slightly larger fluctuation in the initial power from the McMaster coated lasers. This was due to the uneven placement of the laser bars on the jig which resulted in the shadowing of some bars near the active region, and as a result, a change in the reflectance for these bars. This test indicates that sulphur treated and coated facets can have quite stable operating characteristics, however, the variability in the degradation from chip to chip

is large. Visual inspection of the laser facets indicated that the problem is most likely

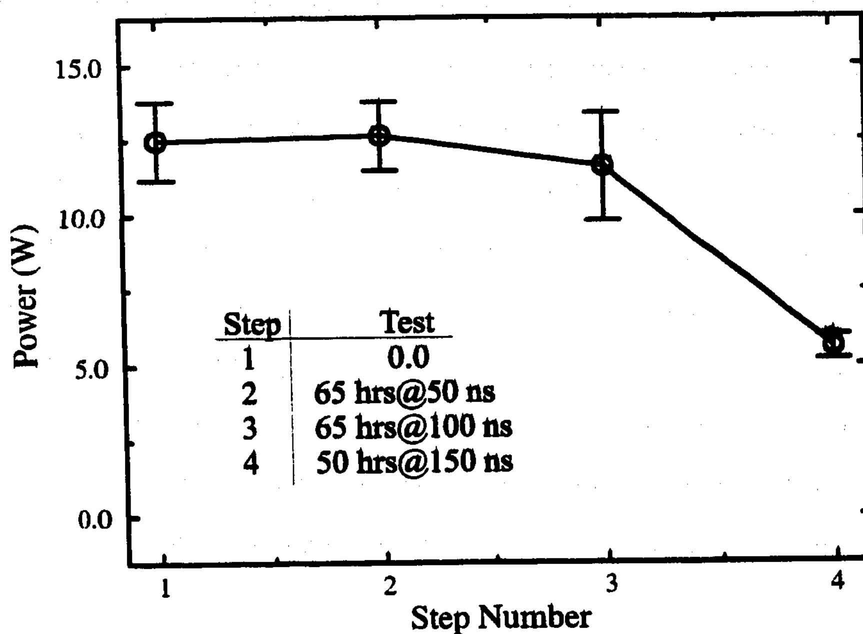

Figure 5.13: Measured optical power at constant current for sulphur treated and coated lasers using the process for optimum PL enhancement.

due to particles which accumulate at the facet during the wet chemical processing and handling of the lasers. These particles can induce local hot spots on the laser facet, and rapidly accelerate facet aging. They can also result in the delamination of the coating film, increasing the local rate of oxidation, and again accelerating facet aging. Figure 5.14 shows the appearance of the facets of the lasers processed using the McMaster argon pre-clean and SiN_x coating from the test shown in Figure 5.12 with those from the test shown in Figure 5.13. The untreated facets showed classic signs of COMD, indicated by the dark line at the position of the active layer on the facet, as well as the marked "beading" associated with thermal breakdown of the active material. In contrast to this, the dark line at the facet is significantly less prominent for the sulphur treated facet, and although significant degradation has occured, it

seems to be localized more to regions where particle contamination is significant.

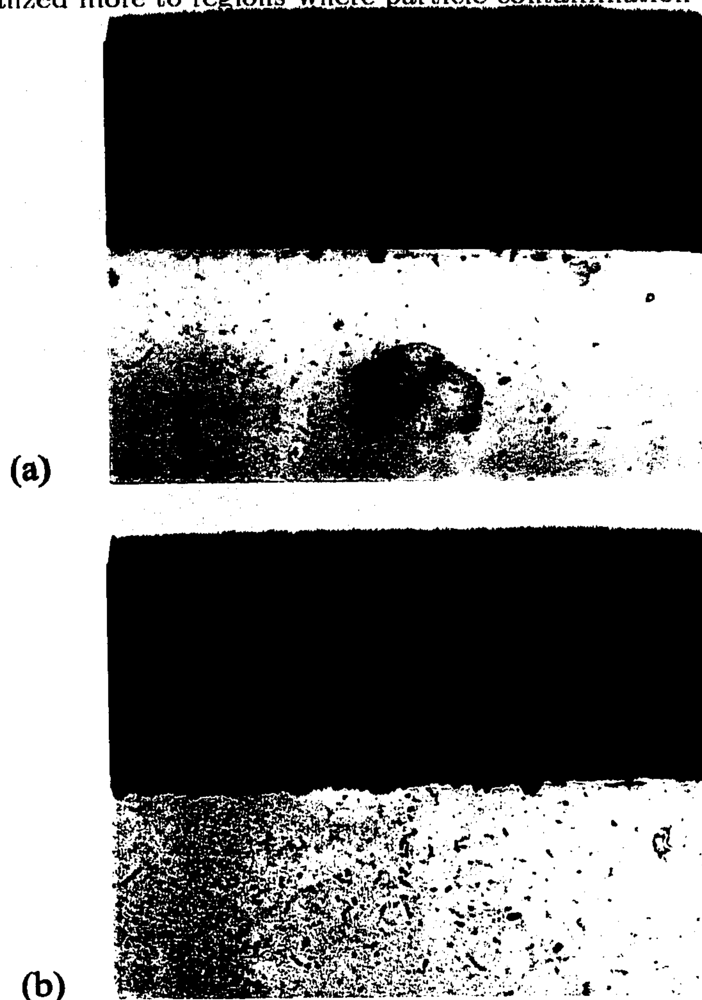

Figure 5.14: Optical micrograph of laser facets after life testing for (a)the optimized process, and (b)the non-sulphur passivated facet.

A difficulty associated with the present processing procedure is the transport of the sulphur treated lasers to McMaster from the University of Toronto. Particle contamination during this step is virtually guaranteed; it would be interesting to attempt a passivation at McMaster in order to remove this variable, and observe the effect on reliability. In addition, there is no data available at present on the reliability of lasers coated using a lower microwave power, which from the PL measurements is

known to induce no damage in the substrate.

Chapter 6

Conclusions and Future Work

6.1 Conclusions

In this Thesis, the development of ECR-PECVD based processes for the fabrication of optical interference filters and passivation coatings on semiconductor laser facets has been described. The well known theoretical basis for the calculation of the reflectance spectrum of an interference filter was summarized. Based on this, the design of anti-reflection coatings and both wide band and narrow band high reflection coatings was carried out. It was emphasized that for the application of these filters to laser facets, the characteristics of the optical waveguide defining the spatial mode of the laser must be taken into account, particularly for anti-reflection coatings. Numerical calculations which account for this effect have been implemented and yield designs for AR coatings which have minimum reflectances well below the necessary minimum for practical applications.

The use of narrow band reflection filters for the control of the laser side mode surpression ratio has been investigated theoretically, using an accurate model of a Fabry-Perot semiconductor laser. This study indicates that the optical coating could begin to have a significant effect on the optical spectrum of the laser, and, as a consequence, the relative intensity noise of the laser under typical operating

conditions. In addition, the small variation of the optical thickness of the coating with temperature could lead to improved temperature stability of the laser after the coating.

One of the most important aspects of this work has been the demonstration that in situ ellipsometry can be used as an effective tool for the monitoring, and control, of multilayer deposition processes. For most filter fabrications, no calibration depositions were required, and the examples shown here were first or second attempts. Careful calibration of the ellipsometer is essential, however, the incorporation of changes in the thin film model used to invert the ellipsometric equations is also important. The most important correction of this type is the variation of the substrate temperature during the deposition of the film. By including this effect, a marked improvement in the accuracy of the prediction of the deposited film index of refraction is observed. Once the substrate temperature is corrected for, real variations in the film index of refraction and thickness with temperature can be observed, allowing the determination of the optical properties at elevated temperatures. This information is important in applications where the thermal stability of the optical thickness is an important issue, such as the applications described in the last paragraph. A jig which can be used to coat the SDL facets, while still monitoring the film properties with the ellipsometer, was designed and fabricated. The important design criteria was the thermal conductivity between the laser bars and the witness silicon wafer. A design which actually used the silicon wafer to clamp the laser bars was found to be the most effective.

The material properties of films fabricated from TDAS in an argon plasma, and a mixed plasma of nitrogen and argon have been described. It was found that the composition of the films deposited in an argon plasma are similar to silicon nitride,

however, carbon has been incorporated, and seems to replace silicon in the bonding network. The chemical stability of these films is very promising, and seems to be due to the high ion bombardment conditions associated with the argon plasma, as well as the carbon incorporation in the films. Extremely low, uniform etch rates with no surface roughening have been observed in HF solutions.

The more conventional silicon precursor, silane, has also been used for the fabrication of SiO_x material. In this case, the range of available refractive indices is higher than that associated with films fabricated from TDAS, and as a result more optimal interference filter designs can be implemented.

Anti-reflection coatings have been deposited on laser facets using TDAS in order to obtain a modal reflectance of approximately 0.1%. With SiH_4, single layer AR coatings with a reflectance of 3×10^{-4} have been obtained on silicon wafers. In addition, two layer AR coatings fabricated on silicon have the wide low reflectance zone which is expected from this design, however, the minimum reflectance obtained was much higher than expected. It is believed that the dispersion in the index of refraction of the material is significant, and so the actual filter characteristics at the longer wavelengths are not characterized. High reflectance coatings using both TDAS and SiH_4 have been fabricated. The wide refractive index range available from films deposited with SiH_4 results in filters with a high reflectance for designs consisting of seven layers. TDAS has been used to obtain high reflectance laser facet coatings, which reduced the laser threshold current by a factor of 3, and which were uniform across the coated laser bar.

Thick narrow band filters consisting of 37 layers were fabricated with a total thickness approaching 5 μm. These filters were mechanically stable on silicon wafers, and had reflectance peaks near the target wavelength. In addition, the width of

the filters was such that one could expect to see effects on the optical spectrum of coated lasers. It was found that inhomogeneous filters could also be fabricated by continuously varying the gas flow rates to the chamber, however, it was observed that the stress in these films actually seemed to be higher, and that history effects in the plasma, possibly associated with residual oxygen, made the accurate control of the refractive index difficult. This type of film was only attempted using TDAS, the fabrication of inhomogeneous filters of SiN_x material using SiH_4 in an ECR-PECVD reactor has been described [93].

Due to the inert character of the films deposited using TDAS in an argon plasma, this film was applied as an encapsulant of sulphur treated $Al_xGa_{1-x}As$ material. A description of the surface properties of GaAs and AlGaAs has been given, along with a survey of efforts to passivate this surface, both for the general improvement of surface properties, and for the particular case of improving the critical power for COMD at a laser facet. The physical processes leading to COMD, and attempts to understand and limit this process from the literature were also related.

From these experiments, it was found that by using a two step deposition process, where the initial film deposition occured without ion bombardment, an effective encapsulant, which stabilized the photoluminescence enhancement associated with the sulphur treatment, could be obtained. It was found that the PL signal could even be enhanced after the optical coating. A possible mechanism for this, involving the incorporation of fixed charge in the insulator material, was postulated. The measurement of the PL stability under high intensity illumination conditions was used to evaluate the effectiveness of various processing conditions on the quality of the capping layer. Many parameters, such as the surface type [(100) versus(110)], the presence of the encapsulation layer, the intensity and wavelength of the illumination,

and the initial plasma exposure during the encapsulation procedure. all had significant effects on the PL decay profile. Although these effects may be difficult to fully characterize, the PL decay was shown to be a useful empirical tool for establishing the effectiveness of the various surface treatments.

The sulphur treatment and encapsulation procedure which resulted in the best PL characteristics was used to encapsulate laser facets which were then tested for high power reliability. It was found that the treated lasers did not perform better than the untreated lasers, however, it was observed that the facet condition after life testing was different for the treated facets. In the treated case, it appeared that particles on the facet nucleated the degradation, rather than a uniform heating effect, which was found to be the more characteristic facet condition after the life testing of untreated lasers.

6.2 Future Work

In many ways, the work related in this Thesis is the initiation of several projects, rather than the completion of any particular project, and so there are many opportunities for continued research. Measurements of the dispersion of the index of refraction, as well as the absorption coefficient of the full range of SiO_x and SiN_x materials deposited using SiH_4 are underway. The refractive index and extinction coefficient can be determined from transmission measurements of 1 μm thick films on quartz substrates [94]. This will allow the accurate prediction of the refractive index at an arbitrary wavelength from the measured index at 632 nm. The same measurement will be made on films deposited using TDAS. The application of the AR coatings on laser facets with stronger index guiding, and lower threshold currents, than the EG&G high power lasers will allow measurements of the modal reflectance

of the laser structure from the intensity modulation in the output spectrum of the laser below threshold [95, 96]. Under these conditions. the accuracy of the designs related in chapter 2 can be evaluated.

A significant improvement in film uniformity can be obtained by modifying the gas dispersion rings used for the silicon precursors. The modification of the TDAS dispersion ring improved the film uniformity over a two inch wafer by a factor of approximately 2. This was after one iteration in the empirical optimization of the flow characteristics of the ring. A similar improvement will also be possible for the SiH_4 dispersion ring.

For the narrow band coatings, and optically thick coatings. which are intended for the modification of the laser spectral characteristics, much experimental work is still required. At present, a temperature controlled laser test station, as well as a scanning mirror monochromator, are being assembled to characterize the laser light power and spectral characteristics, as well as the temperature tuning of the laser. These experiments will be able to characterize the accuracy of the predictions described in this work.

An effect, which has not been emphasized previously, is that for lasers which have some pre-defined mode selection mechanism, such as distributed feedback lasers, the optical filter could be used to improve the modulation characteristics of the laser. As an example. a filter with a reflectance which is a strong function of λ at the operating wavelength of the laser could be used to reduce the observed chirp in the laser frequency during current modulation of the laser. This chirp is due to carrier modulation which varies the optical path length in the cavity. The filter could be used to have the laser cavity loss vary as the operating wavelength of the laser chirps in a way which adds to the power modulation for a given current modulation. By

this method, a reduced current modulation is required to generate the same power modulation, reducing the observed chirp from the laser. A simple rate equation model of the dynamic response of the laser indicates that the filter reflectance change, $dR/d\lambda$, would have to be approximately $0.1/nm$ in order to obtain a significant effect. This is not difficult to obtain, and the edge of a high reflectance quarter wave stack similar to the design shown in Figure 2.10 could be used. The difficult aspect is the reproducible positioning of this edge at the appropriate wavelength.

The issue of passivation of III-V semiconductor surfaces is an area of intense research activity. Recently, the evaporation of a-Si thin films on vacuum cleaved laser facets has resulted in significant increases in the COMD power level of AlGaAs/GaAs lasers [97]. The principle upon which this passivation technique is based was described in section 5.2, and requires the controlled deposition of very thin ($< 50\AA$) films. This experiment is very simple to duplicate in the present reactor. The properties of the coating dielectric will be measured accurately by the ellipsometer, as well, the high vacuum obtained in the ECR-PECVD reactor will allow for a low oxygen contamination of the cleaved surface. The same coating could be applied to sulphur treated surfaces, similar to the experiments described in reference [63], where the sulphur acts to reduce the level of oxidation on the facet surface. This would eliminate the need for cleaving the lasers in vacuum, which is a very impractical step for any manufacturing process.

No compositional measurements have been made at the semiconductor surface of the sulphur treated and encapsulated material. It would be important to verify that the present treatment results in a similar surface structure to those obtained in the literature. Also of interest would be to determine the changes in surface composition which occur after the decay of the PL under high intensity illumination. Simple

cathodoluminescence measurements in a SEM would indicate the degraded surface regions, and correlations could be established between the compositional change at the interface, and the PL decay characteristic.

In summary, this work represents the development of an effective process using TDAS and SiH_4 as silicon precursors for the fabrication of high quality encapsulating dielectric layers, as well as complicated multilayer dielectric interference filters. A reliable process for the coating of laser facets, and the in situ optical monitoring of the thin films using ellipsometry were significant contributions to this process. It is hoped that this base process will be used for new and interesting applications by future researchers.

Appendix A

Fabry-Perot Model of a Semiconductor Laser

In this appendix a description of the model used to investigate the effect of various optical coatings on the output spectrum of a SDL is given. The model is an extension of the one discussed in reference [11] to include a wavelength dependent reflectance and asymmetric cavity.

Figure 2.11 is included here again for convenience.

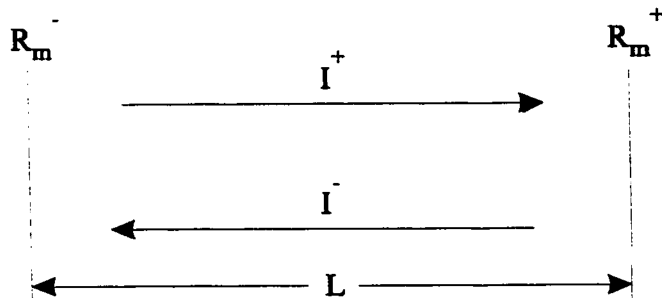

Figure A.1: Schematic diagram of the optical path traced in a Fabry-Perot semiconductor laser cavity.

The relationship between the intensity of a laser mode, and the single pass gain, G_m is given by

$$I_m^{\pm} = \frac{<\delta_m^2> (1 + R_m^{\mp} G_m)}{1 - R_m^{+} R_m^{-} G_m^2}. \tag{A.1}$$

In the model, the modes are labelled such that the gain peak occurs at mode 0, and there are 10 modes included on each side of the gain peak. For the mth mode, the single pass gain, G_m, and the spontaneous emission noise power, $< \delta_m^2 >$, must be calculated in order to calculate the intensity of the mth mode.

From reference [11] the values of these parameters are

$$< \delta_m^2 >= c_m(G_m - 1), \tag{A.2}$$

with $c_m = \beta B_m / g_m$. B_m is the amount of spontaneous emission over the wavelength range of the mth mode. β represents the fraction of this radiation which is coupled into mode m and amplified. g_m sets the shape of the gain profile, and scales the gain per unit length of the laser for a given inversion. The value of the single pass gain is

$$G_m = \exp\left\{ \frac{g_m NL - 2g_m \sum_i \frac{\sigma_i}{g_i} \left[(1 - R_i^-)I_i^- + (1 - R_i^+)I_i^+ \right]}{S - 2\sum_i \sigma_i c_i} \right\}. \tag{A.3}$$

S is the total spontaneous emission rate, σ represents the reduction of the photon density from scattering out of the active region and similar processes. For the purposes of this investigation, σ is set equal to g_m and these losses are neglected.

The parameters B_m and g_m must be determined. They can be expressed as

$$g_m = g(1 - m^2/2000)^{-1}, \tag{A.4}$$

$$B_m = B(1 + 0.05m). \tag{A.5}$$

The gain is a parabolic profile, with the factor 2000 used to approximate measured gain spectra. The linear increase of the spontaneous emission factor with mode number also reflects experimentally measured effects. The remaining parameters, g and B ($B = S/21$ for the number of modes considered in this case) can be removed from the model by scaling the calculated mode powers, and pump rate accordingly. The

pump rate is given in units of gNL/S, while the output intensity is given in units of S/g. These relations allow the single pass gain to be written as

$$G_m = \exp\left\{\frac{1}{(1-m^2/2000)(1-2\beta)}\left(\frac{gNL}{S} - 2\frac{g}{S}\sum_i[(1-R_i^-)I_i^- + (1-R_i^+)I_i^+]\right)\right\}. \tag{A.6}$$

Now one can see the dependence of G_m on the gain profile; the term in the exponent is the product of the gain shape and the net photon injection. The gain of the mth mode depends on the intensities in all the remaining modes, scaled by the transmission of the laser facet for each mode.

Now that expressions for $<\delta_m^2>$ and G_m have been given, equation A.1 can be solved to determine the modal intensities. The numerical solution of the coupled set of equations is an important subject. A description of the algorithm used here is given in the appendix of reference [98], for the case of a symmetric laser cavity without optical coatings.

The procedure is complicated by the asymmetric cavity, but the result is simply a doubling of the amount of calculations which must be carried out. The procedure is to expand an error function, defined as

$$f_m^i = I_m^i - \frac{<\delta_m^2>(1+R_m^i G_m)}{1-R_m^+ R_m^- G_m^2}, \tag{A.7}$$

in a Taylor series about 0 ($i = +$ or $-$ depending on which facet the power is calculated at). By calculating the derivatives of f_m^i with respect to the various mode intensities the stepsize for each mode in a Newton iteration scheme can be calculated. In the numerical simulation, the mode powers are initialized to 0, and the pump power is ramped up from zero. For each increase in the pump power, the mode intensities calculated for the previous pump power are used as the initial guesses of the new set of mode intensities. To improve this initial estimate, and hence make the calculation

more robust. derivatives of the mode intensities with power can be used to improve the initial mode power guess for a new pump current.

Appendix B

Publications and Presentations

1. C. H. Edirisinghe, I. P. Koutzarov, L. Z. Jedral, H. E. Ruda, M. G. Boudreau, P. Mascher, A. Moore, "The Encapsulation of Sulphur Passivated AlGaAs Surfaces using Silicon Nitride", submitted for publication to the Journal of Applied Physics.

2. M. G. Boudreau, P. Mascher, "Deposition of Rugate Interference Filters on Laser Facets Using In Situ Ellipsometry for Process Control", Presented at the Optical Society of America annual meeting, Rochester, N. Y., October, 1996.

3. M. G. Boudreau, P. Mascher, C. H. Edirisinghe, H. E. Ruda, and I. P. Koutzarov, "Enhanced Photoluminescene From Sulphur Passivated AlGaAs Laser Facets after Argon and Tris dimethylaminosilane Plasma Exposure", Presented at the Optical Society of America annual meeting, Rochester, N. Y., October, 1996.

4. M. G. Boudreau, J. Brown, P. Mascher, "The Properties of silicon nitride formed through the decomposition of tris dimethylaminosilane in an argon plasma", Proceedings of the 13th Conference on CVD, The Electrochemical Society, p. 464-469, 1996.

5. C. H. Edirisinghe, H. E. Ruda, I. Koutzarov, A. Liu, L. Jedral, M. G. Boudreau,

M. Boumerzoug, J. Brown, P. Mascher, A. Moore and R. Henderson, "Passivation Studies on AlGaAs Surfaces Suitable for High Power Laser Development", Materials Research Society symposium proceedings, Vol. 378, P. 1007-1012, 1995.

6. I. P. Koutzarov, H. E. Ruda, C. H. Edirisinghe, L. Z. Jedral, Q. Liu, A. Moore, R. Henderson, M. G. Boudreau, M. Boumerzoug and P. Mascher, "Optical Characterization of Passivation for High Power $Al_xGa_{1-x}As$ Based Lasers", Society of Photo-Optical Instrumentation Engineers, Vol. 2382, p. 42-48, 1995.

7. M. G. Boudreau, M. Boumerzoug, P. Mascher and P. E. Jessop, "Decomposition Characteristics of Tris Dimethylaminosilane in an ECR-PECVD Reactor", in: Plasma Processing, G. S. Mathad and D. W. Hess (eds.), The Electrochemical Society p. 536-544. 1994.

Bibliography

[1] C. W. Wieman and L. Holberg. *Review of Scientific Instruments*, 62(1):1, 1991.

[2] C. Spielmann, M. Lenzner, F. Krausz, R. Szipöcs, and K. Ferencz. *Laser Focus World*, 31(12):55, 1995.

[3] A. Kasukawa, N. Iwai, and N. Yamanaka. *Electronics Letters*, 30(13):1064, 1994.

[4] M.H. MacDougall, H. Zhao, P. D. Dapkus, M. Ziari, and W. H. Steier. *Electronics Letters*, 30(14):1147, 1994.

[5] T. R. Chen, B. Zhao, Y. H. Zhuang, A. Yariv, H. Blauvelt, and N. Bar-Chaim. *Fiber and Integrated Optics*, 9:347, 1990.

[6] T. Higashi, S. Ogita, H. Soda, H. Kobayashi, H. Kurakake, O. Aoki, and N. Okazaki. *IEEE Journal of Quantum Electronics*, 29(6):1918, 1993.

[7] D. R. Hjelme, A. R. Mickelson, R. G. Beausoleil, J. A. McGarvey, and R. L. Hagman. In *Proceedings of the SPIE*, volume 1043, page 167, Bellingham, Wa., 1989. SPIE.

[8] P. Zorebedian and W.R. Trutna Jr. *Optics Letters*, 123(10):826, 1988.

[9] I. Ladany, M. Ettenberg, H. F. Lockwood, and H. Kressel. *Applied Physics Letters*, 30(2):87, 1977.

[10] C. Vassallo. *Journal of the Optical Society of America*, 5(11):1918, 1988.

[11] D.T. Cassidy. *IEEE Journal of Quantum Electronics*, QE-20(8):913, 1984.

[12] H.A. Macleod. *Thin Film Optical Filters.* Adam Hilger Ltd, Bristol, second edition, 1986.

[13] J. Strong. *Journal of the Optical Society of America*, 26:73, 1936.

[14] W. Geffken. Interferenzlichtfilter, 1939. No. 716 153.

[15] A. Thelen. *Design of Optical Interference Coatings.* McGraw Hill, New York, 1989.

[16] P. Yeh. *Optical Waves in Layered Media.* John Wiley and Sons, New York, 1988.

[17] J. A. Dobrowolski and D. Lowe. *Applied Optics*, 17(19):3039, 1978.

[18] P. G. Verly. In *Proceedings of the SPIE*, volume 2253, page 161, Bellingham, Wa, 1993. SPIE.

[19] P. V. Bulkin, P. L. Swart, and B. M. Lacquet. *Applied Optics*, 35(22):4413, 1996.

[20] S. D. Smith. *Journal of the Optical Society of America*, 48:43, 1958.

[21] D. M. Braun and R. L. Jungerman. *Optics Letters*, 20(10):1154, 1995.

[22] C. Vassallo. *Electronics Letters*, 24:61, 1988.

[23] C. Vassallo. *Electronics Letters*, 24:62, 1988.

[24] P.C. Kendall, D.A. Roberts, P.N. Robson, M.J. Adams, and M.J. Robertson. *IEEE Photonics Technology Letters*, 5(2):148, 1993.

[25] J. Xu, D. Yevick, and M. Gallant. *Optical Society of America*, 12(4):725, 1995.

[26] T. Saitoh, T. Mukai, and O. Mikami. *Journal of Lightwave Technology*, LT-3(2):288, 1985.

[27] P. Zorabedian and W.R. Trutna Jr. *Optics Letters*, 13(10):826, 1988.

[28] J. E. Fouquet, D. M. Braun, and G. R. Trott. *IEEE Journal of Quantum Electronics*, 32(10):1777, 1996.

[29] S. H. Woodside. Master's thesis, McMaster University, 1992.

[30] M. G. Boudreau. Master's thesis, McMaster University, 1993.

[31] S. G. Wallace. Master's thesis, McMaster University, 1996.

[32] D. L. Smith. *Journal of Vacuum Science and Technology A*, 11(4):1843, 1993.

[33] S. Dzioba and R. Rousina. *Journal of Vacuum Science and Technology B*, 12(1):433, 1994.

[34] Z. Yin and F. W. Smith. *Journal of Non-Crystalline Solids*, 137/138:879, 1991.

[35] G. Lucovsky and W. B. Pollard. In *The Physics of Hydrogenated Amorphous Silicon II*, page 322. Berlin, 1984. Springer-Verlag.

[36] J. Brown. Master's thesis, McMaster University, 1995.

[37] C. Amra. *Applied Optics*, 32(28):5481, 1993.

[38] P. S. Hauge and F. H. Dill. *Optics Communications*, 14:431, 1975.

[39] D. E. Aspnes. *Journal of the Optical Society of America*, 10(5):974, 1993.

[40] I. Fan Wu, J. B. Dottellis, and Mario Dagenais. *Journal of Vacuum Science and Technology A*, 11(5):2398, 1993.

[41] D. E. Aspnes. *IEEE Journal of Selected Topics in Quantum Electronics*, 1(4):1054, 1995.

[42] E. D. Palik. *Handbook of Optical Constants.* Academic Press Inc., Orlando, 1985.

[43] P. G. Eliseev. *Reliability Problems of Semiconductor Lasers.* Nova Science Publishers. Inc., New York, 1991.

[44] M. Fukuda. *Reliability and degradation of Semiconductor Lasers and light emitting diodes.* Artech House. Boston. 1991.

[45] R. G. Waters. *Progress in Quantum Electronics*, 15:153, 1991.

[46] P. G. Eliseev. *Progress in Quantum Electronics*, 20(1):1, 1996.

[47] D. A. Shaw and P. R. Thornton. *Solid State Electronics*, 13:919, 1970.

[48] E. Yablonovitch, C. J. Sandroff. R. Bhat, and T. Gmitter. *Applied Physics Letters*, 51(6):439, 1987.

[49] C. J. Sandroff. R. N. Nottenburg, J.-C. Bischoff, and R. Bhat. *Applied Physics Letters*, 51(1):33, 1987.

[50] Champika Edirisinghe. Master's thesis, University of Toronto, 1997.

[51] C. W. Wilmsen. *Physics and Chemistry of III-V Compound Semiconductor Interfaces.* Plenum Press, New York, 1985.

[52] J. R. Chelikowsky and M. L. Cohen. *Physical Review B*, 20:4150, 1979.

[53] J. A. Knapp and G. J. Lapeyre. *Journal of Vacuum Science and Technology*, 13:757, 1976.

[54] W. E. Spicer, P. Pianetta, I. Lindau, and P. W. Chye. *Journal of Vacuum Science and Technology*, 14(4):885, 1977.

[55] W. E. Spicer, P. W. Chye, P. R. Skeath, C. Y. Su, and I. Lindau. *Journal of Vacuum Science and Technology*, 16(5):1422, 1979.

[56] W. Shockley. *Electrons and Holes in Semiconductors*. Van Nostrand, New York, 1950.

[57] D. J. Wolford, G. D. Gilliland, T. F. Kuech, L. M. Smith, J. Martinsen, G. A. Bradley, C. F. Tsang, R. Venkatasubramanian, S. K. Ghandi, and H. P. Hjalmarson. *Journal of Vacuum Science and Technology B*, 9(4):2369, 1991.

[58] S. Shikata, H. Okada, and H. Hayashi. *Journal of Vacuum Science and Technology B*, 9(5):2479, 1991.

[59] H. Hasegawa, H. Ishii, T. Sawada, T. Saitoh, S. Konishi, Y. Liu, and H. Ohno. *Journal of Vacuum Science and Technology B*, 6(4):1184, 1988.

[60] C. J. Spindt and W. E. Spicer. *Applied Physics Letters*, 55(16):1653, 1989.

[61] A. Kapila, V. Malhotra, L. H. Camnitz, K. L. Seaward, and D. Mars. *Journal of Vacuum Science and Technology B*, 13(1):10, 1995.

[62] S. Shikata and H. Hayashi. *Journal of Applied Physics*, 70(7):3721, 1991.

[63] L. J. Huang, K. Rajesh, W. M. Lau, S. Ingrey, D. Landheer, J.-P. Noël, and Z. H. Lu. *Journal of Vacuum Science and Technology A*, 13(3):792, 1995.

[64] Z. H. Lu and J.-M. Baribeau. *Applied Physics Letters*, 70(15):1989, 1997.

[65] A. Moser and E. E. Latta. *Journal of Applied Physics*, 71:4848, 1992.

[66] C. D. Thurmond, G. P. Schwartz, G. W. Kammlott, and B. Schwartz. *Journal of the Electrochemical Society*, 127(6):1366, 1980.

[67] M. Passlack, M. Hong, J. P. Mannaerts, R. L. Opila, and F. Ren. *Applied Physics Letters*, 69(3):302, 1996.

[68] M. Passlack, M. Hong, E. F. Schubert, J. R. Kwo, J. P. Mannaerts, S. N. G. Chu, N. Moriya, and F. A. Thiel. *Applied Physics Letters*, 66(5):625, 1995.

[69] L. Pavesi and M. Guzzi. *Journal of Applied Physics*, 75(10):4779, 1994.

[70] B. Smandek, G. Chmiel, and H. Gerischer. *Ber. Bunsenges. Phys. Chem.*, 93:1094, 1989.

[71] G. Chmiel and H. Gerischer. *Journal of Physical Chemistry*, 94:1612, 1990.

[72] P. W. Epperlein and G. L. Bona. *Applied Physics Letters*, 62(24):3074, 1993.

[73] N. I. Katsavets, D. Z. Garbuzov, T. A. Grishina, I. E. Kudrik, and P. V. Pitkianen. In *Proceedings of the SPIE*, volume 2148, page 152, Bellingham, Wa., 1994. SPIE.

[74] G. Chen and C. L. Tien. *Journal of Applied Physics*, 74(4):2167, 1993.

[75] R. Schatz and C. G. Bethea. *Journal of Applied Physics*, 76(4):2509, 1994.

[76] P. W. Epperlein, P. Buchmann, and A. Jakubowicz. *Applied Physics Letters*, 62(5):455, 1993.

[77] J. S. Yoo, H. H. Lee, and P. Zory. *IEEE Photonics Technology Letters*, 8(3):202, 1991.

[78] H. Nagai and Y. Noguchi. *Applied Physics Letters*, 33(4):312, 1978.

[79] M. Fukuda and K. Takahei. *Journal of Applied Physics*, 57(1):129, 1985.

[80] S. A. Schafer and S. A. Lyon. *Journal of Vacuum Science and Technology*, 19(3):494, 1981.

[81] A. Moser. *Applied Physics Letters*, 59(5):522, 1991.

[82] M. Matsumoto, K. Sasaki, M. Kondo, T. Ishizumi, T. Takeoka, H. Nakatsu, M. Watanabe, O. Yamamoto, and S. Yamamoto. *Japanese Journal of Applied Physics Part 2*, 32(5A):L665, 1993.

[83] A. V. Syrbu, V. P. Yakovlev, G. I. Suruceanu, A. Z. Mereutza, L. J. Mawst, A. Bhattacharya, M. Nesnidal, J. Lopez, and D. Botez. *Electronics Letters*, 32(4):352, 1996.

[84] N. Chand, W. S. Hobson, J. F. deJong, P. Parayanthal, and U. K. Chakrabarti. *Electronics Letters*, 32(17):1595, 1996.

[85] S. Kamiyama, Y. Mori, Y. Takahashi, and K. Ohnaka. *Applied Physics Letters*, 58(23):2595, 1991.

[86] G. Beister, J. Maege, D. Gutsche, G. Erbert, J. Sebastian, K. Vogel, M. Weyers, J. Würfl, and O. P. Daga. *Applied Physics Letters*, 68(18):2467, 1996.

[87] G. Beister, J. Maege, J. Sebastian, G. Erbert, L. Weixelbaum, M. Weyers, and J. Würfl. *IEEE Photonics Technology Letters*, 8(9):1124, 1996.

[88] P. D. Colebourne. PhD thesis, McMaster University, 1993.

[89] M. Mihara, Y. Nomura, M. Mannoh, K. Yamanaka, S. Naritsuka, K. Shinozaki, and T. Yuasa. *Journal of Applied Physics*, 55(10):3765, 1984.

[90] M. Mihara, Y. Nomura, M. Mannoh, K. Yamanaka, S. Naritsuka, K. Shinozaki, and T. Yuasa. *Journal of Applied Physics*, 55(10):3760, 1984.

[91] Kenji Uchida and Shin'ichi Nakatsuka. *Japanese Journal of Applied Physics*, 32(7A):L883, 1993.

[92] Z. Lu, S. S. He, Y. Ma, and G. Lucovsky. *Journal of Non-Crystalline Solids*, 187:340, 1995.

[93] P. L. Swart, P. V. Bulkin, and B. M. Lacquet. *Optical Engineering*, 36(4):1214, 1997.

[94] R. Swanepoel. *Journal of Physics E*, 16(12):1214, 1983.

[95] D. T. Cassidy. *Journal of Applied Physics*, 56(11):3096, 1984.

[96] B. W. Hakki and T. L. Paoli. *Journal of Applied Physics*, 46(3):299, 1975.

[97] L. W. Tu, E. F. Schubert, M. Hong, and G. J. Zydzik. *Journal of Applied Physics*, 80(11):6448, 1996.

[98] J. E. Hayward. PhD thesis, McMaster University, 1993.

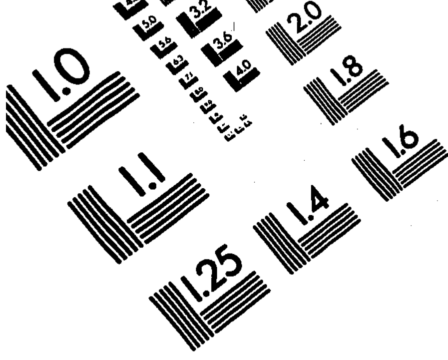

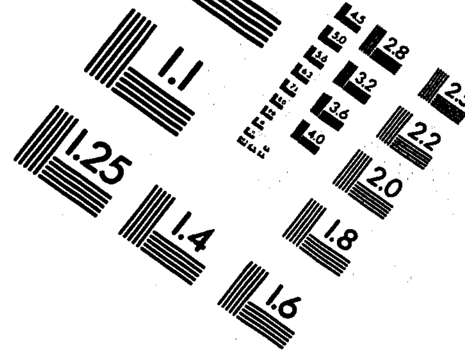

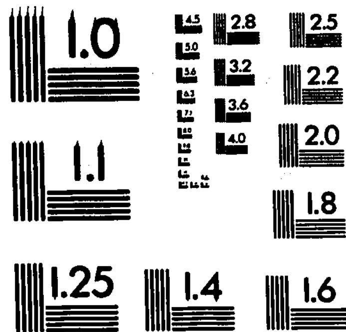

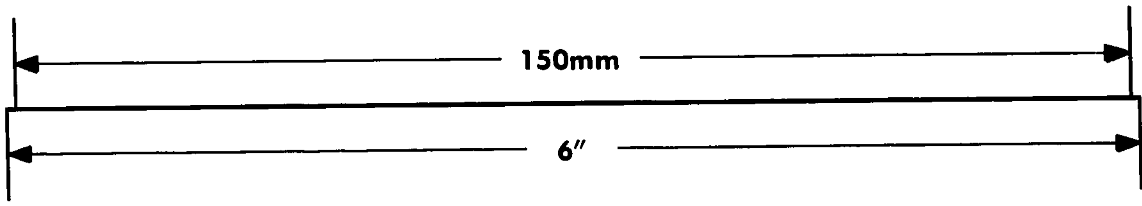

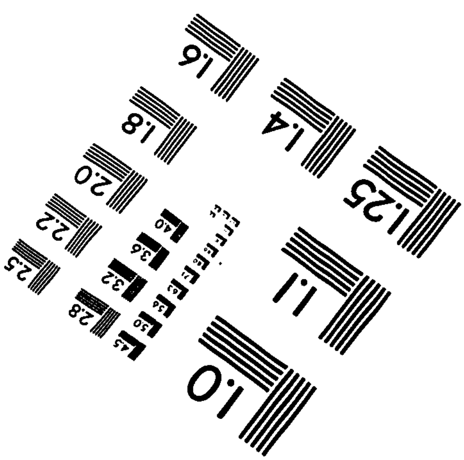

APPLIED IMAGE . Inc
1653 East Main Street
Rochester, NY 14609 USA
Phone: 716/482-0300
Fax: 716/288-5989

© 1993, Applied Image, Inc., All Rights Reserved